Development of a Low-Emission Spray Combustor for Emulsified Crude Oil

STEVEN G. TUTTLE
KATHERINE M. HINNANT
THOMAS N. LOEGEL
BRIAN T. FISHER

Navy Technology Center for Safety and Survivability
Chemistry Division

ALFREDO D. TUESTA
MICHAEL WEISMILLER

National Research Council Postdoctoral Associate
National Academies of Science
Washington, D.C.

March 3, 2017

REPORT DOCUMENTATION PAGE

1. REPORT DATE (DD-MM-YYYY)
03-03-2017

2. REPORT TYPE
Memorandum Report

3. DATES COVERED (From - To)
September 3, 2014 – October 31, 2016

4. TITLE AND SUBTITLE

Development of a Low-Emission Spray Combustor for Emulsified Crude Oil

5a. CONTRACT NUMBER
C14PG00060

5b. GRANT NUMBER

5c. PROGRAM ELEMENT NUMBER

6. AUTHOR(S)

Steven G. Tuttle, Katherine M. Hinnant, Thomas N. Loegel, Brian T. Fisher, Alfredo D. Tuesta,* and Michael Weismiller*

5d. PROJECT NUMBER

5e. TASK NUMBER

5f. WORK UNIT NUMBER
4817

7. PERFORMING ORGANIZATION NAME(S) AND ADDRESS(ES)

Naval Research Laboratory
4555 Overlook Avenue, SW
Washington, DC 20375-5320

8. PERFORMING ORGANIZATION REPORT NUMBER

NRL/MR/6180--17-9720

9. SPONSORING / MONITORING AGENCY NAME(S) AND ADDRESS(ES)
Bureau of Safety & Environmental Enforcement
381 Elden Street
Herndon, VA 20170

10. SPONSOR / MONITOR'S ACRONYM(S)

MIS-NONDOD

11. SPONSOR / MONITOR'S REPORT NUMBER(S)

12. DISTRIBUTION / AVAILABILITY STATEMENT

Approved for public release; distribution is unlimited.

13. SUPPLEMENTARY NOTES

14. ABSTRACT

A sub-scale and engineering-scale burner were designed, built, and tested in an effort to develop a single nozzle burner capable of efficiently atomizing and burning neat, emulsified, and weathered crude oil for spill response and remediation. The sub-scale and engineering-scale burners were capable of burning 22.9 bbl/day and 91.5 bbl/day, respectively. We discovered that the flow-blurring atomizers used in these burners were able to effectively atomize the highly viscous emulsified crude oil, even with nozzle diameters of 12.7 mm and 25.7 mm. The increasing size of both the atomizer and burner geometry has been shown to increase burn temperature without negatively impacting burner performance. A parallel laboratory study used a flat-flame stabilized spray burner to examine fundamental spray combustion behavior. It was shown that flame radiation has a significant impact on the droplet ignition and spray flame propagation.

15. SUBJECT TERMS

Crude oil	Combustion	Flow-blurring atomizer
Spray	Flame	
Atomization	Phase doppler interferometry	

16. SECURITY CLASSIFICATION OF:

a. REPORT	b. ABSTRACT	c. THIS PAGE
Unclassified Unlimited	Unclassified Unlimited	Unclassified Unlimited

17. LIMITATION OF ABSTRACT
Unclassified Unlimited

18. NUMBER OF PAGES
121

19a. NAME OF RESPONSIBLE PERSON
Steven G. Tuttle

19b. TELEPHONE NUMBER (include area code)
(202) 767-0810

Standard Form 298 (Rev. 8-98)
Prescribed by ANSI Std. Z39.18

i

CONTENTS

FIGURES

TABLES

DEVELOPMENT OF A LOW-EMISSION
SPRAY COMBUSTOR FOR EMULSIFIED CRUDE OIL

INTRODUCTION

This report describes the completed tasks, results, conclusions, and future work for the development of a low-emission spray combustor for emulsified crude oil. We report the design, development, and testing of a sub-scale (25%) and an engineering-scale (50%) burner to meet this objective. We also report the laboratory results of supporting basic research that examines the fundamental spray combustion behavior of crude oils. These efforts included laboratory-scaled spray measurements, flame characterization, and analytical measurements of the oils, their emulsion and weathered mixtures, and the combustion products.

A recent concept demonstration study by the Naval Research Laboratory (NRL) showed the feasibility of using a flow-blurring atomizer (FBA) to atomize and burn neat and emulsified crude oil with nozzle pressure drops less than 20 psig [1]. This is a crucial step in developing an alternative to *in situ* burning (ISB) for oil spill remediation. Off-shore crude oil spill remediation is generally performed by gathering the surface oil into large pools where the oil is either pumped into floating storage bladders for shipping to oil processing facilities [2] or the pools are ignited to form large fires [3]. Referred to as *in situ* burning [3], this process produces large plumes of soot and other potentially harmful pollutants [4-7] and leaves a slick of residual hydrocarbons remaining on the ocean surface[8]. The seawater provides a nearly infinite heat sink that prevents a layer 1 - 3 mm-thick of crude oil from evaporating and burning. Additionally, ISB cannot reliably burn emulsified crude oil formed by surface or benthic mixing [3]. In contrast, oil flares, formed by spraying and igniting crude oil, produce much less soot than in situ burning and have been reported to be capable of burning emulsified oil with seawater volume fractions up to 80% [9,10]. In the past, these flares have used atomizers that were either mechanically complex or required high air and oil pressures that small sea vessels cannot supply. For example, the Super Green burner manufactured by Expro operates at ~1400 psig.

The effects and performance impact of emulsified fuel has been studied for diesel [11,12] and gas turbine [13,14] engines for some time, but none of these fuels contain the wide range of hydrocarbons, including asphaltenes, that are contained in crude oil and in some distillation-residual fuels used in marine diesel engines.

Researchers have examined the combustion behavior of distillation-residual fuels that operators use in the large diesel engines of ships, generally referred to as residual or bunker fuel. These fuels are formed from crude oil that has the lighter hydrocarbons distilled to make gasoline, diesel, kerosene, and other profitable fuel and chemical feedstock. Investigators have studied residual fuels because the constituent asphaltenes have significant influence on ignition and smoke formation behavior. In a study by Bartle *et al.* [15], they report that increasing asphaltene content reduces ignition delay by emitting lighter-weight, more reactive alkanes during devolatilization, which occurs when the large asphaltene molecules are heated and start to break apart into smaller molecules. Simultaneously, increasing asphaltene concentrations increased the smoke content, composed of soot and cenospheres (hollow particles of inorganic ash). We can expect that some of these results will qualitatively translate to crude oil, but since residual fuel oils have a smaller fraction of lighter hydrocarbons, the droplet evaporation and combustion process will proceed differently.

We can suppose that the crude oil droplets diameters will reduce more rapidly and leave smaller particles than residual fuels, but that behavior has yet to be established.

The principle benefit of incorporating the FBA into a combustor system is the low atomization pressure. As we discussed in Ref. [1], the pumping power scales with $\Delta p^{3/2}$, where Δp is the pressure drop. Therefore, if we fix the flow rate, the power requirement for a 1400 psig spray system is 586 times that of a 20 psig spray system. For large, sea-based vessels and oil exploration platforms, which have onboard power generation systems capable of supplying more than a megawatt of power, supplying power to high-pressure pumps and compressors is trivial. For a small vessel, such a power requirement is not practical.

Another benefit of the FBA atomizer is the simple design. It contains no moving internal parts and it only requires liquid and air supply pressures up to 30 psig. Additionally, the liquid orifice size is quite large (~2-50 mm), allowing particulate debris to pass through the atomizer without clogging it.

Our previous work demonstrated the capability of the FBA to atomize neat and emulsified crude oil to practical, combustible droplet sizes [1]. We used an atomizer with a liquid and air exit diameter of 3.18 mm to produce a spray plume, which a spark-ignited propane torch ignited. We observed the basic combustion anchoring behavior, from which we were able to design a notional combustor. We also made *in situ* droplet measurements of the spray plume using phase Doppler anemometry for both water and burning crude oil. This work continues that effort and focuses on developing an operable, robust burner geometry and determining the operability characteristics and performance.

OBJECTIVE

The objective of this work has been to transition the Technology Readiness Level of a low-emission, low pressure atomizer and combustor for emulsified crude oil from 3 to 5 by developing and refining the performance of a quarter and half-scale flow blurring atomizer spray burner system.

APPROACH

Two parallel efforts composed this program. The first was an engineering development program that focused on the burner design, assembly, and testing to determine operability and performance. In the process, we incorporated design changes to improve the operability and performance. Unfortunately, the combustion behavior of neat and emulsified crude oil is significantly different from other fuels. Higher viscosity, particulate asphaltenes suspended in the oil, emulsification, and atomization all contribute to complicate the burner development process. To address the gaps in the fundamental understanding of emulsified crude oil combustion, we conducted a parallel effort focused on basic combustion behavior. We was carried out this effort in the laboratory, with a smaller scale burner designed to burn all of the crude oil by surrounding the plume with a stream of hot combustion gases. The following sections describe the wide range of work encompassing both efforts. The first section focuses on the sub-Scale and engineering-scale burner development. The second focuses on the laboratory-scale investigations.

Sub-Scale and Engineering-Scale Burner Development
This section describes the engineering effort of the burner development. Constituent subsections describe the sub-scale burner, the associated instrumentation, and the engineering scale burner. Detailed diagrams and discussion clarify each major sub-system.

Sub-Scale Burner Component Design
The subscale burner was composed of the atomizer, plasma igniter-jets, combustor, and the associated flow system. The general design concepts were based on the previous concept demonstration work [1], but adapted by increasing the overall dimensions. The previous atomizer orifice diameter was 3.18 mm

(0.125 in), while the sub-scale atomizer diameter was 13.0 mm (0.510 in). We scaled the dimensional details of the atomizer and burner accordingly.

Atomizer
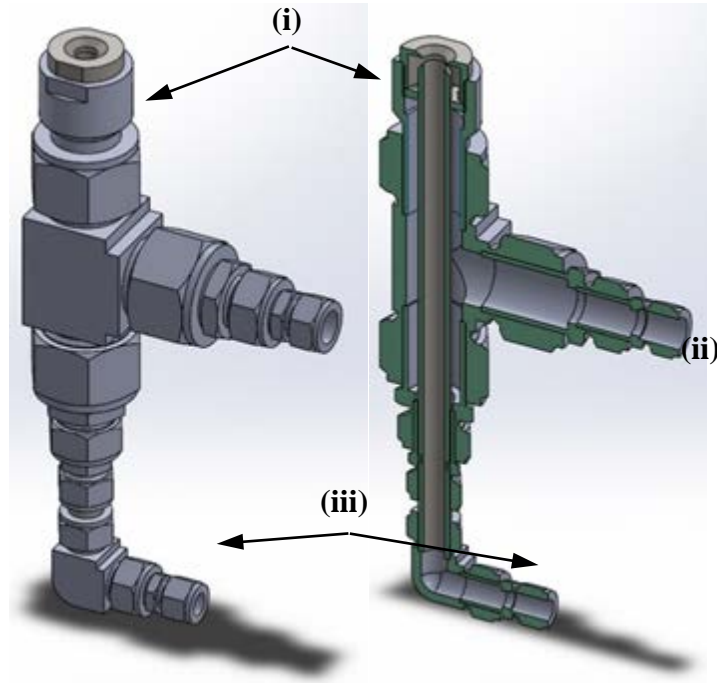
Fig. 1-Atomizer subassembly. The atomizer (i), air input (ii), and fuel input (iii) are shown.

Figure 1 shows the atomizer subassembly. The atomizer components were the only custom manufactured components, while the rest of the assembly uses standard compression fittings. Atomizing air entered through the air input on the side, labeled (ii) in Fig. 1, while the crude oil entered through the fuel input at the bottom (iii). These two input streams then mixed and exited through the atomizer (i). We chose to use standard compression fittings in lieu of designing and fabricating a custom manifold assembly. This reduced the number of custom parts.
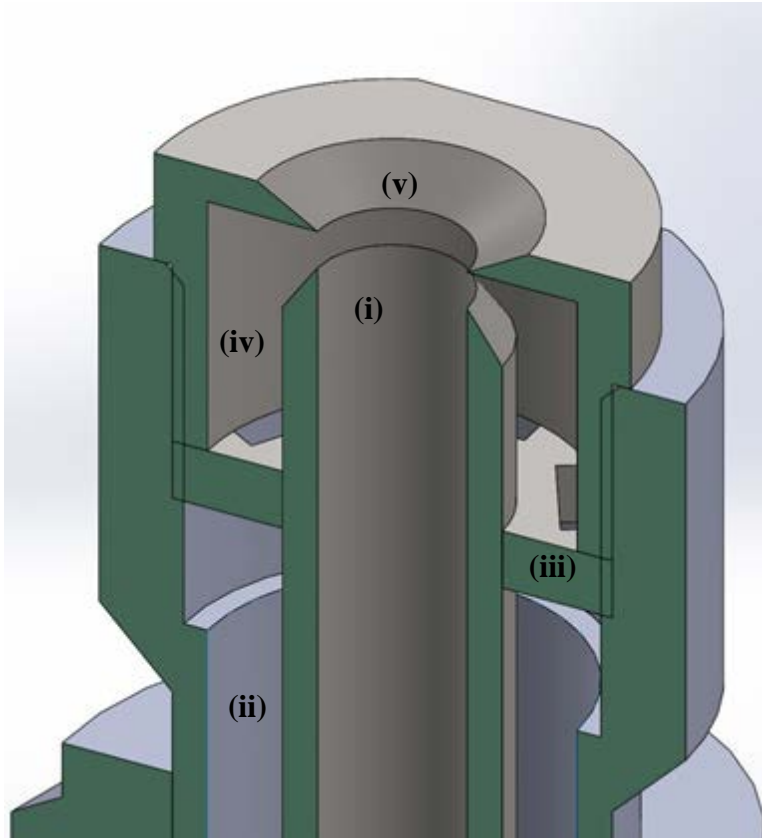
Fig. 2-Detailed, cross-sectional view of the atomizer subassembly. The fuel tube (i), annular air tube (ii), strainer plate (iii), air manifold (iv), and atomizer orifice (v) are shown.

Figure 2 shows the details of the atomizer components. The crude oil flowed through the fuel tube (i) while air flowed through an outer, annular passage, (ii) past the strainer (iii), and into the plenum (iv), after which the air flowed across the face of the fuel tube exit. The strainer also coaxially aligned the fuel tube with the atomizer orifice. The air flowed rapidly across the face of the oil at the tip of the fuel tube, and the resulting shear and flow instability atomized the crude oil and expelled the droplets out of the nozzle orifice (v). We tested tip configurations: one, as shown in Fig. 2, and three others with geometry designed to add turbulence to the flow. We will not provide details on the atomizer design details, since they need to be examined in further detail.

Plasma Ignition

We had anticipated two potential design concepts for the plasma ignition torch. From our previous work, we knew only a steady-flow heat source would anchor the spray plume flames. In order to anchor combustion for emulsion fractions greater than 25% and for higher flow rates, we required higher temperature and heat flow than the propane torch we used in the last study.

Plasma torches emit gas streams at temperatures in the range of 10,000 K, composed of ionized, electrically excited gases. In this application, the plasma was to be composed of electrically-excited, oxygen compounds (O, O_2, O_3) and nitrogen compounds. The combination of hot and electrically-excited, ionized gases accelerated the ignition process [16,17] and stabilized plume combustion more effectively than a stream of propane-air combustion products, which has a temperature in the range of 1500 K and is not composed of the same highly-reactive, excited species. Our first alternative was to use a plasma fuel nozzle

4

provided by Applied Plasma Technologies. They have a great deal of experience with unusual combustor design and flame anchoring technologies, but their hardware required special power supplies and was prohibitively expensive ($10,000–$40,000). Our second alternative was to use a conventional plasma torch, normally used to cut metal. Vendors sell configurations with remote operation capabilities, their components are readily available, and are almost a tenth of the price of the specialty built systems. The vendors also supply diesel generators for use with welders and plasma torches for locations unreachable by the electrical grid. After our visit to the Navy's Emergency Ship Salvage Material (ESSM) stockpile warehouse at the Cheatham Annex, we realized that a diesel-powered system is compatible with the infrastructure of most oil spill response agencies. We ordered two torches (Miller Spectrum 625, shown below in Fig. 3) and incorporated them into the burner design. These remotely triggered systems allowed us to control their operation at a safe distance from the combustor.

Fig. 3-Plasma cutting torch integrated into the combustor design.

Combustor Shroud

The combustor needed to meet a number of design requirements for this program. The geometry needed to scale proportionally with the hardware successfully used in the last study [1]. We also needed to be able to modify the design to optimize operation without rebuilding hardware, limit the number of fabricated components, and be able to increase or decrease the air entrainment rate. Therefore, the components needed to be modular and interchangeable.
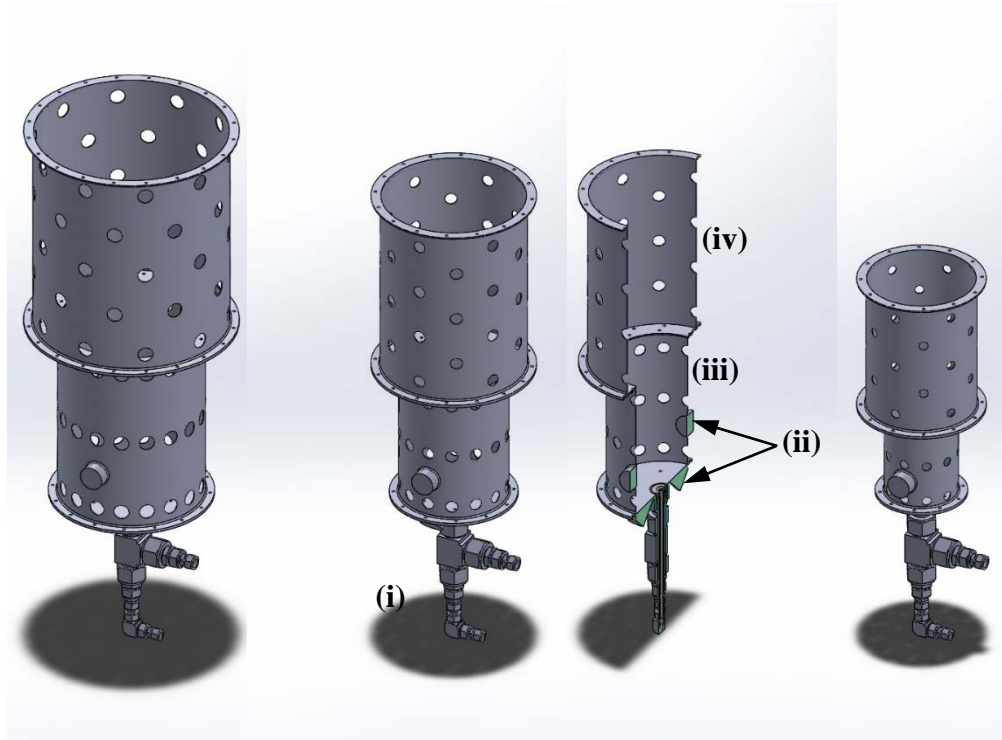
Fig. 4-The three combustors sizes incorporating the atomizer (i), plasma igniters (ii), and a first (iii) and second (iv) stage combustor shroud. (Images not to scale).

(a) **(b)** **(c)**
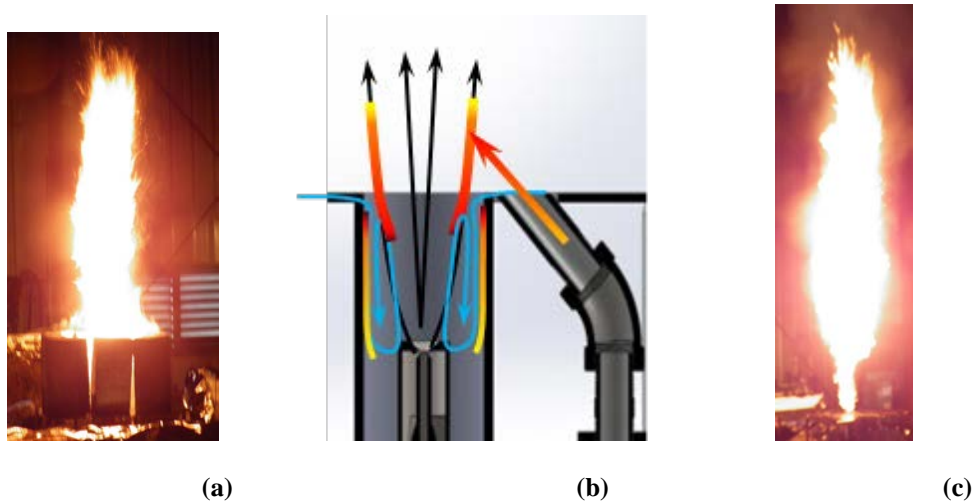
Fig. 5-Diagrams of the combustion process for crude oil. (a) The full combustion plume, with the base shielded by fire bricks, as studied in the last investigation[1]. (b) The stabilization process at the base of the plume, with fresh air shown in blue and flames shown in red-orange. (c) Photograph of an unenclosed burning plume.

To address the requirement for design adaptability, we created the three basic combustor designs shown in Fig. 4. They are composed of the atomizer subassembly (i) (shown in Fig. 4), plasma ignition torches (ii), a first stage combustor shroud (iii), and a second stage combustor shroud (iv). We designed four ports for the plasma jets, with anticipation that we would only use a maximum of two at any time. This allowed us to determine the ideal location for igniting and stabilizing spray plume combustion.

In order to replicate the flame stability process we observed in previous work, we needed to re-examine the flame stabilization processes, as shown in Fig. 5b. During our previous concept demonstration investigation, we found that for pure crude oil, the spray plume flames stabilized within the narrow co-flow duct that enclosed the atomizer [1]. In order to produce a similar stabilization process, we scaled the length and diameter of the burner's dimensions to match the proportions from the previous study, scaled from the fuel atomizer diameter (D_f), as shown in Table 1. For the smallest combustor size, we scaled the first stage combustor length (L_1) and diameter (D_1) to ratios of $15.7 \times D_f$.

In the same study, we also observed that the emulsified crude oil required a larger flame anchoring volume [1]. From this observation, we increased the diameter and length of the first stage combustor by two additional increments of 50% and then 100%, for the medium and large combustor, to improve the flame anchoring for the emulsified crude oil plume.

Table 1-Combustor Dimensions. The numbered subscripts refer to the combustor stages, while subscript f refers to the fuel nozzle.

Dimension	Demonstration	Sub-Scale			Engineering Scale
		Small	Medium	Large	
D_f (in.)	0.125	0.510	0.510	0.510	1.01
L_1 (in.)	1.97	8	12	16	24
L_1/D_f	15.7	15.7	23.5	31.4	23.8
D_1 (in.)	2.067	8	12	16	24
D_1/D_f	16.5	15.7	23.5	31.4	23.8
L_1/D_1	0.95	1.0	1.0	1.0	1.0
D_2 (in.)	9.0	12	16	20	32
D_2/D_f	72	23.5	31.4	39.2	31.7
L_2 (in.)	9.0	12	16	20	32
L_2/D_f	72	23.5	31.4	39.2	31.7
D_3 (in.)			20		40
D_3/D_f			39.2		29.6
L_3 (in.)			20		40
L_3/D_f			39.2		39.6

Figure 5c, from our concept demonstration study, shows that the plume transitioned from a narrow burning jet into a much broader burning plume structure. This effect was caused by hydrocarbon evaporation, entrainment of the surrounding air into the plume, and mixing; when the local fuel-air mixture was within its flammability limits, it was ignited by the upstream flames. The rapid combustion produced a dilatative flow divergence that expanded the exterior plume gases. We observed this effect with both the crude oil and the emulsified crude oil. The difference between the two was that the emulsified crude oil did not stabilize in the initial narrow channel, but in the downstream expansion, after the propane jet anchored the plume combustion. A narrow initial combustion stage, followed by a wider secondary combustion stage, also produces flow separation and recirculation zones that transport hot products upstream. Creating a

combustor composed of abrupt increases in diameter allows both the plume expansion and recirculation zones to drive flame anchoring.

The length and diameters of the secondary combustion stage did not simply scale from our last study. The diameter of the space created by the firebricks was much larger than the plume and only extended a short distance along its length. Therefore, we decreased the secondary combustor diameter to a combustor-nozzle diameter (D_2/D_f) ratio of 23.5 for the smallest combustor, and increased the medium and large combustors by ~50% and ~100% respectively. Although the diameter of space created by the firebricks was larger than the plume, the firebricks did not contain the length of the plume. To address this, we added a secondary combustor duct, and later a tertiary duct, to the length of the burner with options for additional sections.

To entrain air into the burning plume, we incorporated a number of holes into the combustor shroud design. Stainless steel foil tape closed off holes to limit air entrainment. We could have increased the amount of air entrainment by increasing the size or number of holes, but we did not explore that design change.

We designed all burners with interchangeable ducts and adapters, with the dimensions shown in Table 1. The secondary stages of all three sized-combustors are compatible to equal or smaller combustor diameters. This allowed us to examine the scaling rules that produced the most effective combustion behavior.

Instrumentation

For the sub-scale and engineering-scale burner tests, we designed the instrumentation for integration, if possible, into the data acquisition system. The data acquisition system recorded temperature, pressure, Boolean logic (on/off), volume flow, mass flow, and other parameters automatically to allow the test operators to focus on the burner behavior instead of manually recording a large number of test parameters. We manually gathered samples, such as soot filters and sorbent tubes, for post processing.
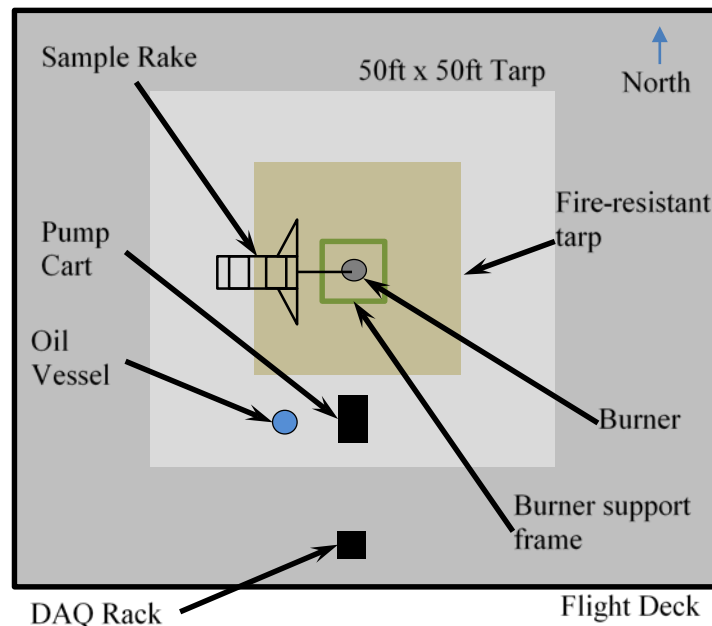
Fig. 6-Test layout, with the burner placed in the center of the tarp, on the flight deck.

Testing Facility

We used two different test facilities for the sub-scale and engineering-scale testing. The first, and principle, test facility was that of the flight deck at the Naval Research Laboratory's Chesapeake Bay Detachment (CBD) in Chesapeake Beach, Maryland. The flight deck is a large concrete platform for large-scale, outdoor burn testing. We used the high-capacity air compressor in the adjacent Bldg. 313 to supply both the atomization air and the plasma torch air. A gear pump supplied the crude oil to the atomizer, controlled by a general data acquisition and control system.

Figure 6 shows the layout for the various components of the flight deck experiment. The 50 ft. × 50 ft. tarp kept oil from draining into the fluid sump system of the flight deck. A second, fire-resistant tarp rested in the center and prevented damage to the larger tarp. In the center of the tarps, the burner rested on a support frame. We placed the pump cart that housed the oil pump and plasma torches about 20 feet south of the burner. Directly south of the tarp and pump cart, we placed the data acquisition (DAQ) rack, from which the air, oil, and plasma flows were controlled and recorded. The sample rake rested west of the burner and housed a vacuum pump. A series of sorbent socks were on hand to capture any spilled oil.

The flight deck sampling rake was a 6.1 m-high (20 ft.) structure on wheels with a sampling tube and thermocouple mounted on a rake to extract samples at different axial and radial locations with respect to the plume axis. We used the measurements of plume temperature and emissions to compare the performance of the combustor geometries. In this investigation, we placed the rake inlet at the centerline of the plume.
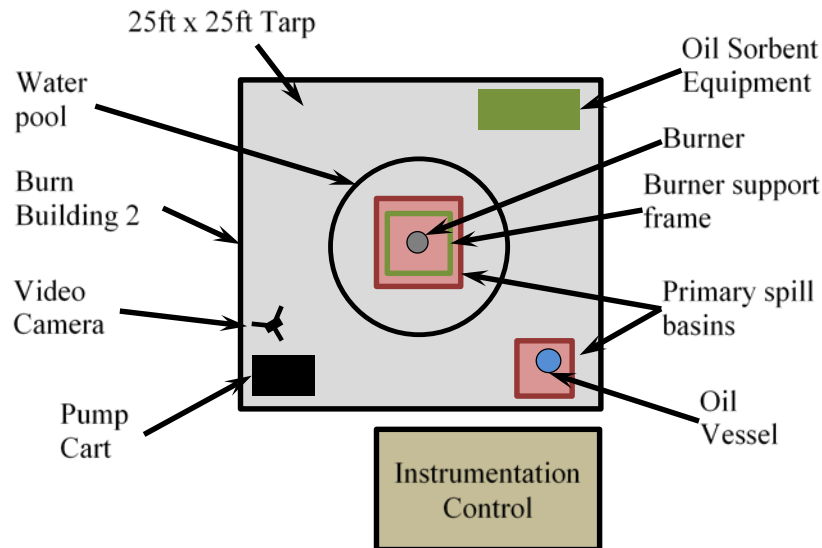
Fig. 7-Test layout, with the burner placed in the center of the tarp, in Bldg. C252.

Among the problems with testing on the flight deck was the dependence on the weather for accurate soot measurements. We conducted the tests on the flight deck and discovered that the constantly shifting wind moved the exhaust plume away from the plume-sampling rake. The only period of time when we could dependably gather meaningful data was in the early morning, just prior to and just after sunrise when the wind speed was very low. This small period of about one hour, and the required set up time, severely

limited our ability to conduct performance tests needed to optimize the burner design. Furthermore, flight deck testing required up to two hours of set up and the same amount of time to take down test equipment, which severely limited available test time in a given day. In order to rectify these problems, we moved the subscale experiment to a small burn building at CBD, which designated as Bldg. C252.

We continued to use the high-capacity air compressor in Building 313 to supply pressurized air to both atomize the crude oil and operate the plasma ignition torches. A 1-$^3/_8$"-diameter air hose directed the pressurized air from the compressor in Bldg. 313 to the instrumentation control trailer, where a manifold split the air into four branches. The first was a standard compressed air connection for the plasma torches. The second, third, and fourth branches directed the air through regulators and critical flow Venturis. The second and third branches, which have been described in previous documentation [1], can be connected to 1"-diameter hoses to supply atomizing air to the sub-scale burner. The engineering scale burner used an additional regulator-Venturi channel, attached to a 1-$^1/_2$"-diameter hose on the second or third branch.
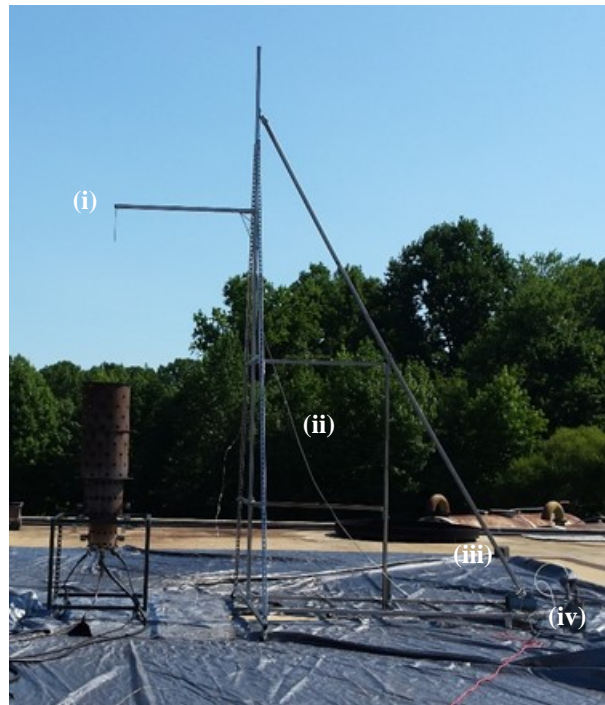
(a)
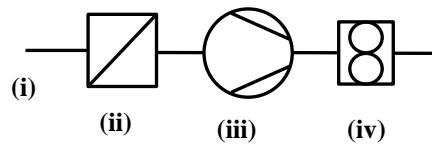
(b)

Fig. 8-(a) Instrumentation rake for extracting plume samples and measuring plume temperature and (b) plumbing diagram. The rake inlet (i), filter (ii), vacuum pump (iii), and displacement meter (iv).

Figure 7 shows the burner layout and the various equipment placed inside of Bldg. C252. The burner, oil pump, and oil plumbing rested on a 25 ft. x 25 ft. square tarp to contain spills, leaks, and unburned droplets. The burner rested on the 3 ft. × 3 ft. × 3 ft. burner support frame, which is inside of a primary spill basin, which is a 5 ft. × 5 ft. × 1 ft. steel pan, formerly used for pool fire testing. A loop of 1-$^3/_8$-" hose, placed underneath the tarp, encircled the primary spill basin. This formed a shallow pool that we filled with water prior to testing to contain additional oil spills and prevent heat damage to the tarp, as we observed during tests on the flight deck. Oil sorbent equipment and materials were stored inside the building.

The pump cart contained the oil pump and the plasma torch controllers. Oil containers, such as a 50-gallon drum and various buckets were contained in another primary spill basin, also a former burn pan. The Instrumentation and Control trailer contained the data acquisition system, air metering and control plumbing, and the video feed from the camera inside the building. To reduce the risk of injury, we kept people outside of building C252 and remotely operated the test facility. Directly above the burner, we suspended a gas-sampling rake and exposed-bead thermocouple.

Figure 8a and b shows a photograph of the rake structure placement with respect to the burner and the associated plumbing schematic, respectively, that gathered plume samples on the flight deck. The burner exhaust was directed to the rake inlet, where a 6.35 mm-diameter (1/4 in) tube and a K-type thermocouple were mounted at the tip of a 1.55 m rake (See Fig. 8a). The diagram in Fig. 8b shows the path the sampled gases travel. They passed into the inlet (i) and then through a Gelman Ø47 mm in-line filter holder (ii), which removed any soot from the gas stream. A vacuum pump (iii) drrew the gases, which were then directed through a displacement meter (iv) to measure the displaced gas volume. Once the plume reached steady state, we turned on the pump and sampled for 1:30 to 2:00 minutes. We then recorded the volume displacement and duration. Borosilicate glass fiber filters (Pall Gelman, Type A/E, Ø47 mm, 1μm pore) captured any condensates, both liquids and solids, from which we could determine the concentration of soot and unburned solids. We measured the mass of the filters before and after testing.

The hazardous waste effluent from these tests consisted of tarps and plastic sheets covered with crude oil. Additional oil spill collection pads, pillows, and socks were on the deck to capture any spilled oil. Including the surrounding socks, described above, there was be a total absorption capability of 185 gallons. Table 2 provides the oil absorption capabilities of the equipment we had on hand.

Table 2-Oil-spill collection equipment to be used and stored on hand

Description	Qty.	#/Pack	Gal./ Pack	Capacity (gal.)
Oil-Only Polypropylene Sorbent, 16" Wide x 18" Long Perforated Pad, Absorbs 16 Gallon/Pack	150	50	16	48
Oil-Only Polypropylene Sorbent, 16" Width x 20" Length Pillow, Absorbs 45 Gallon/Pack	10	10	45	45
Oil-Only Polypropylene Sorbent, 3" Diameter x 24' Length Sock, Absorbs 12 Gallon/Pack	9	2	12	54
Spill-Control Sorbent Kit, Oil Only, 38 Gallon Absorption Cap, in 55-gal Drum	1	1	38	38
Total Spill Capability				185

Flow Metering & Control

The air delivery system we used in this study was the same used in the previous study [1], with some adaptation. For this study, we used a commercial compressor system, hoses to deliver the air, pressure regulators, and orifices to meter the flow. Figure 9 shows the schematic of the airflow system and a photograph of the instrumentation rack, with Roman numerals designating different components. Air passed through the compressor (i), into the tank (ii), and then through the dryer (iii). A ball valve (iv) restricted the air from entering a hose (v) which directed the air to a manifold, which in turn split the flow into three branches. On all but the first branch, a manual regulator (vi) on each branch reduced and regulated the air pressure before the air passed through an orifice. The first branch (vii) had a direct feed, after passing through a filter and another dehumidifier, to the plasma torches. The second and third branches (viii and ix) utilized NIST-traceable pressure transducers (Omega Engineering, PX409-150A5V and PX409-50A5V) upstream and downstream from a NIST-traceable, critical-flow Venturi tube (Flow Systems, SN-16-AN-0.022-SS) and metering tube (Flow Systems, FC, IS, and ES-16-0.87-SS) to meter flow to the spray atomizer and other flow requirements. Hoses then directed the flows of all three branches to their respective components.

An Oberdorfer gear pump (N400RS17-N52-vfd), with a variable frequency drive system to control the flow rate, pumped the crude oil mixtures. It was capable of pumping crude oil up to 3 gal/min, which spanned our anticipated limit of 2.1 gal/min.
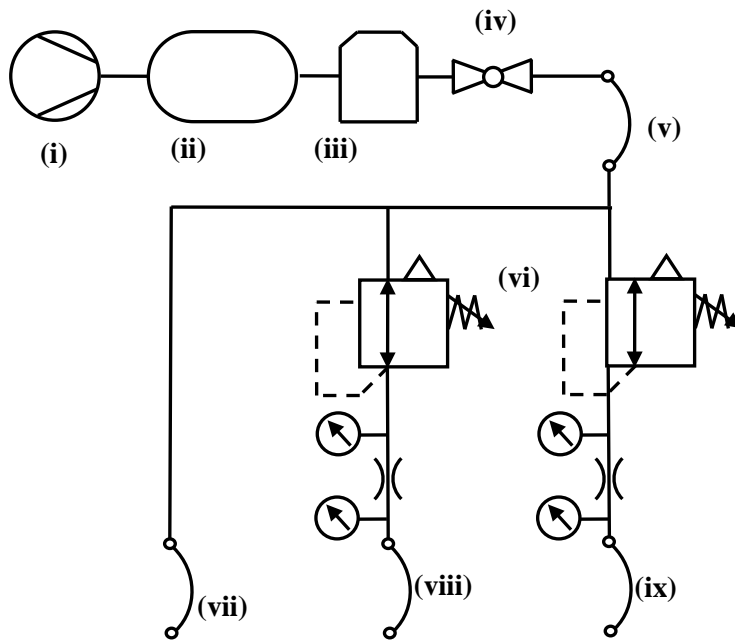
(a) Airflow control system.   (b) Data acquisition system.

Fig. 9-Shown are (a) a schematic of the airflow control system and (b) a photograph of the rack-mounted data acquisition system. The manifold valves, Venturi tubes, and regulators are mounted on the side.

Atomizer

NRL's R&D Services machined the engineering-scale atomizer (Fig. 10). As for the sub-scale burner, a straight-flow atomizer and a swirled-flow atomizer orifice were both constructed. We anticipated that we would only use the swirled-flow atomizer during testing, but the straight-flow atomizer provided an alternative if there are any issues. Our tests showed that the swirled-flow atomizer was sufficient.

Fig. 10-Photograph of the assembled atomizer for the engineering-scale burner.

Plasma Ignition

For the engineering-scale burner, we used the same plasma torches we used for the sub-scale burner. To examine a potential alternative, we purchased a plasma torch to test its performance and behavior. We discovered that it produced only a fraction of the heat and the resulting velocity was very low. While testing with a Bunsen burner flame, we found that it could not ignite the flame unless the plasma air was seeded with a hydrocarbon fuel.

(a) Hot side of combustor inlet bulkead.

(b) Cold side of combustor inlet bulkead.

Fig. 11-Photographs of the assembled engineering-scale burner bulkhead.

Bulkhead

Figure 11 shows the hot and cold sides of the inlet bulkhead. We simplified the design and mounted the plasma torch holders directly to the bulkhead. We also installed two thermocouple mounts to measure the flame anchor recirculation zone temperature. Because of the size of the first stage and the anticipated

radiative heat transfer from the burner, we mounted the inlet bulkhead directly to the 4-ft cube Unistrut support frame.

Combustor Shroud

We designed a similar combustor shroud for the engineering-scale testing to that used for the sub-scale testing. Table 1 has the dimensions for the engineering-scale burner, as well as the sub-scale and demonstration burners.

Fig. 12-Photograph of the inside of the instrumented combustor shroud.

Figure 13 shows the fully assembled and instrumented combustor shroud. The full height of the burner is 3.66 m (12 ft.). The inside diameter of the 1ˢᵗ, 2ⁿᵈ, and 3ʳᵈ stages are 23.75 in., 31.75 in., and 39.75 in. (60.3 cm, 80.6 cm, and 101.0 cm), respectively. We mounted thermocouples from the shroud wall at the half-height of each stage and at the full-height. For the first stage, thermocouples were at the centerline and at 67% and 33% of the radius. In the second stage, thermocouples were at the centerline and at 75%, 50%, and 25% of the radius. In the third stage, thermocouples were placed at the centerline, 80%, 60%, 40%, and 20% of the radius. At the exit plane, we only placed a thermocouple at the centerline.

The thermocouples provided temperatures at the critical regions of the flow for comparison with the previous burner and as different operation parameters are varied. In particular, the centerline thermocouples detected the temperature at the centerline of the plume, where we anticipated that the oil would be largely unburned. Near the wall, the thermocouples detected the temperature of the entrained air.

Fig. 13-Photograph of assembled engineering-scale burner.

We should note that thermocouples are not a completely accurate method to detect gas temperature. By their very design, they work best in situations

15

with low-gradient, high conductive or convective heat transfer. We can think of a thermocouple junction (bead) and the wires leading to it as large pin fins, used for augmenting heat transfer [18]. Unfortunately, thermocouples are biased by radiation [19]. This is especially a problem in sooty or particle-laden combustion flows, such as crude oil, where the radiative heat transfer to the thermocouple is as large as or greater than the convective heat transfer. Therefore, the thermocouple will not accurately reflect the gas temperature unless the radiative loading can be calculated [19]. But thermocouples are the most robust temperature measurement method and their results are provide relative performance metrics that are comparable between architectures for the same fuels.

Laboratory-Scale Experimental Investigation

The laboratory-scale experiment provided a more accessible, measurable platform to examine the fundamental behavior of both the flow blurring atomizer and crude oil combustion. The laboratory experimental effort was composed of droplet combustion tests using our existing laboratory spray burner (see Fig. 14), with an FBA insert. We examined droplet evaporation and combustion and how those behaviors change with various design parameters. Specifically, we examined the influence of the crude oil, initial droplet diameter distribution, the upstream heat source, oil emulsification, dispersant, and oil weathering on the spray combustion behavior. We used droplet measurement to examine the spray plume and measure how these parameters influence the droplet evaporation and combustion process. Coherent Anti-Stokes Raman Spectroscopy (CARS) provided *in situ*, plume measurements of temperature and mole fractions of O_2 and CO_2 [15-17]. A portable, NDIR gas analyzer provided measurements of the exhaust emissions.

These measurements provided insight into the flame stability and droplet combustion mechanisms of atomized crude oil and how these behaviors change with crude oil, emulsification, and weathering. Understanding of these basic behaviors and the analytical and empirical correlations that predict them provide design insight for the sub- and full-scale burner designs, as well as optimal burner parameters, such as the air-liquid ratio (ALR), plasma torch power, and flow rates. These relationships can be used to optimize performance of the burner during deployment in a wide range of spill environments.

Laboratory-Scale Spray Burner Design

The laboratory-scale experiment is composed of a flat flame burner, which surrounds a spray jet. The laboratory-scale atomizer, shown in Fig. 15, is composed of similar components to those of the previous study and to the subscale atomizer described above. The crude oil traveled upward through a central fuel tube (i) toward the shear and atomization zone (ii), where air from a co-axial, annular duct (iii) flows radially inward across the face of the crude oil and atomizes it. A strainer (iv) centers the fuel tube and allows air to flow toward the shear zone. The total diameter of the assembly is 9.53 mm (0.375 in), with a 3.18 mm (0.125 in) outside diameter and a 1.40 mm (0.055 in) inside diameter fuel tube. The spray orifice diameter matches the inside diameter of the fuel tube.

Fig. 14- Laboratory spray burner operation with heptane spray.
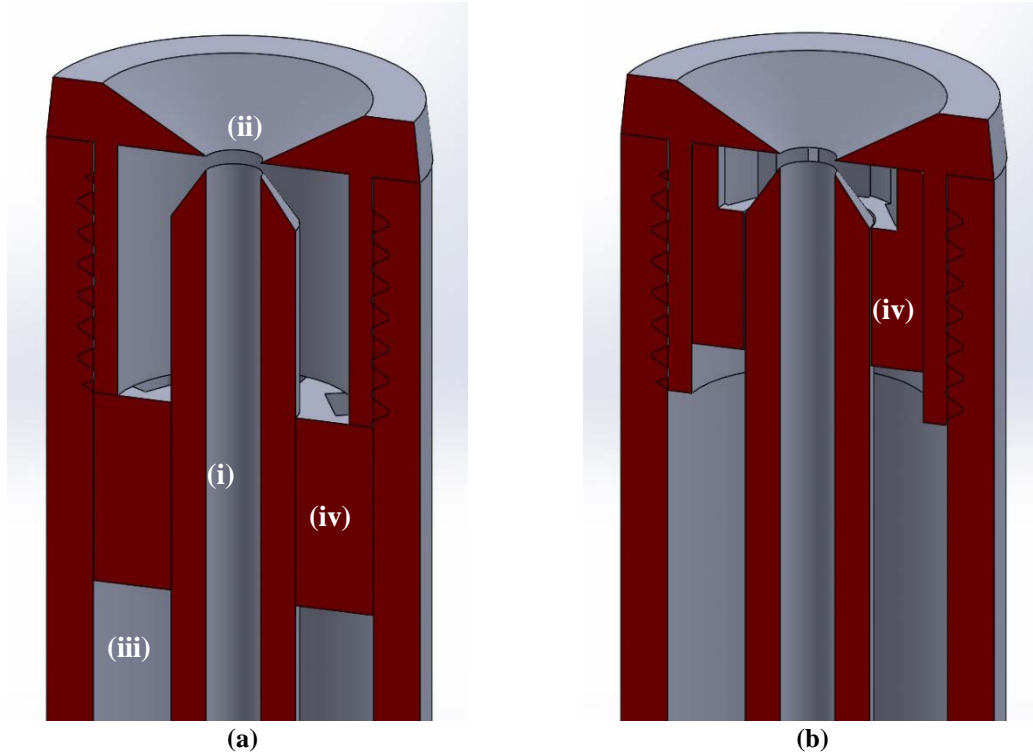
Fig. 15-Cross-sectional view of the laboratory-scale atomizer. The central fuel tube (i); shear and atomization zone (ii); co-axial, annular duct (iii); and strainer (iv) are shown. (a) The original design and (b) the final design used different approaches to center the fuel tube. The newer atomizer has bushing that centers the fuel tube more effectively than the older, looser bushing.
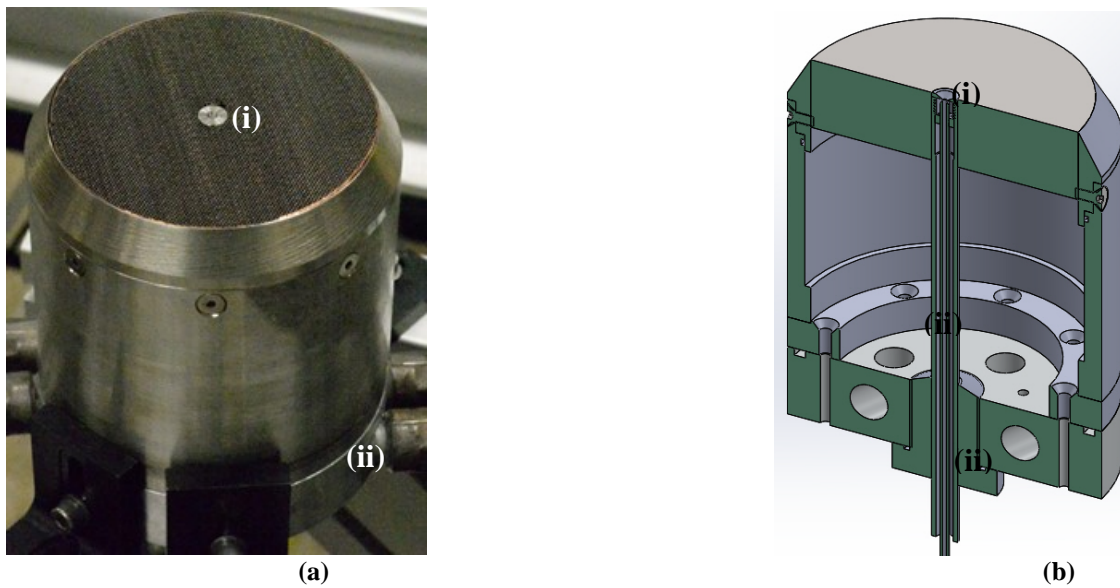
Fig. 16-The (a) complete view and (b) cross sectional view of the flat flame burner. The stainless steel honeycomb (i) as well as the fuel-air mixture inlet ports (ii) are shown.

The flat flame burner, shown in Fig. 16, was constructed during the principle investigator's time as an NRL Karles' Fellow. It was originally designed for use with a spray jet composed of droplets produced by an ultrasonic nebulizer and a co-flow of air (not shown), but was designed to be modular and adaptable for use with any atomizer that could be designed for the geometry.

For this investigation, we placed the atomizer described above in the center of the flat flame burner, composed of stainless steel honeycomb (i), 1 in thick with 0.030 in cells. A mixture of air and hydrogen or flowed into the base of the burner through inlet ports (ii) then upward through a series of perforated plates (not shown) that uniformly distributed the flow before it entered the honeycomb flame holder.

The air flow metering system used in the laboratory is similar to that used at NRL's Chesapeake Bay Detachment (CBD) and contains some of the same components. In contrast, it only has one air channel with a critical flow Venturi tube, but it has three additional channels that use orifices (O'Keefe Controls, KH-##-BR) to meter airflow. Air is supplied by a building-wide air supply system. The propane or hydrogen is supplied from compressed gas cylinders and then metered by a choked-flow orifice. The crude oil was pumped by a Harvard Apparatus dual-syringe pump using stainless steel syringes.

Physical Property Measurement

An integral part of the laboratory effort was the careful measurement of the physical properties of the crude oil mixtures. These measurements included the density, viscosity, refractive index, and surface tension.

The density was measured using two American Petroleum Institute (API) hydrometers with a combined degree range 18 to 41. A hydrometer is a long piece of glass with a capsule of enclosed air and a thin tube with a degree range on the tube. The hydrometer is submerged into a liquid and is allowed to float in the liquid sample. The degree on the hydrometer at the liquid and hydrometer interface represents the API of the liquid. If the API is above 10, the petroleum liquid will float on water and if it is below 10, it is heavier and will sink. Therefore, the larger the API value, the less dense the liquid.

The viscosity was measured using a glass viscometer, with a constant of 0.10783 at 25°C. Liquid samples were poured into the viscometer and a suction bulb was used to transfer the liquid sample up the viscometer. Once the liquid was above an indicator line, the bulb was removed. A stop watch was then used to measure the time it took the liquid to travel between two indicator lines. The time (in seconds) was then multiplied by the constant to achieve the units cP.

A MISCO Hand-held refractometer was used to measure the refractive index. A small liquid sample (1-2 drops) is placed over a lens of the refractometer. The amount of light refracted through the sample is then measured and displayed on the hand-held device. Water is used to calibrate the instrument to ensure accurate measurements.

The surface tension was measured using a DuNoy-Ring tensiometer. A titanium ring is suspended above a pool of the liquid sample. The ring is then slowly lowered into the liquid until the interface of air and liquid is reached. The ring then moves below the surface 5mm and begins to back towards the surface. The force exerted on the ring to break through the surface is then measured and compared to the surface area of the ring resulting in mN/m.

Phase Doppler Anemometry

The flat flame burner was placed on a three-axis traverse for interrogation by phase Doppler anemometry (PDA). The traverse system is similar to that used in the concept demonstration study[1], while the phase Doppler interferometry system is an upgraded version.
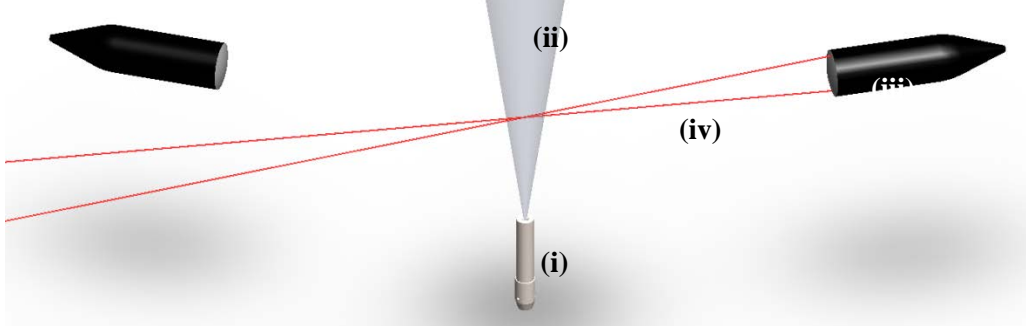
Fig. 17-Simplistic diagram of the phase Doppler interferometer with the spray nozzle (i), plume (ii), laser transmitter (iii), laser beams (iv), and receiver (v).

Phase Doppler anemometry operates using light scattered by a spherical droplet as it passes through a measurement volume formed by crossing two laser beams. The laser beam is first split into two equally powered beams; one beam passes through a Bragg cell oscillating at 80 MHz, which modulates the wavelength for that beam before interacting with the other beam to form the measurement volume. As a result, the interference pattern formed where the beams cross translates in space at a constant rate. When a droplet or bubble passes through the measurement volume, it refracts the light, which is gathered by the receiver and amplified by a photomultiplier. The signal processor uses the frequency shift in the scattered signal to calculate the velocity. The signal processor uses the phase differences between three spatially separate detectors in the receiver to calculate and validate droplet diameters.

We have replaced the 10 mW, 632 nm HeNe laser transmitter we used previously[1] with a 120 mW, 660 nm laser (Dantec 9065X0341 FlowExplorer 2D) to measure vertical velocity and droplet diameter. We also added a 120 mW, 785 nm laser for horizontal velocity. The receiving optics are the same, except for an additional photomultiplier to gather the 785 nm signal. We have also replaced the processor unit, which processes the analog signals from the receiver photomultipliers and digitizes it. The newer processor (Dantec 9062N0551 BSA P80) is compatible with conventional computer hardware and is capable of multi-dimensional velocity measurements. The traverse is similar, though smaller, than that used in the concept demonstration droplet measurements.

For droplet diameter notation, we used the mean diameter (D_{10}) and the Sauter-mean diameter (D_{32} or SMD), which is used in literature when calculating mass transfer and reaction rates of sprayed fuel [20]. The statistical expressions are as follows:

$$D_{10} = \frac{\sum N_i D_i}{\sum N_i} \tag{1}$$

$$D_{32} = \frac{\sum N_i D_i^3}{\sum N_i D_i^2} \tag{2}$$

where N is the number of droplets in a particular statistical bin of the probability distribution and D is the diameter for that bin. The mean diameter is the conventional statistical expression and provides a conventional comparison between measurements, but it does not reveal the distribution or spread of the data. The Sauter mean diameter (SMD) is statistically representative of the volume-to-surface area ratio of the droplet distribution of the spray. The SMD provides a comparison between measurements and provides some insight into the statistical spread of the data. It is used because the volume-to-surface ratio of a droplet is representative of the ratio of the thermal capacitance ($c_p \rho \pi d^3/6$) to the rate of heat and mass transfer at the surface ($\dot{q}_{m,e} \pi d^2$). The dominant parameters are c_p (heat capacity), ρ (density), d (diameter), and $\dot{q}_{m,e}$

(mass flux from the droplet or heat flux to the droplet driven by temperature gradient, concentration gradient, or surface combustion).
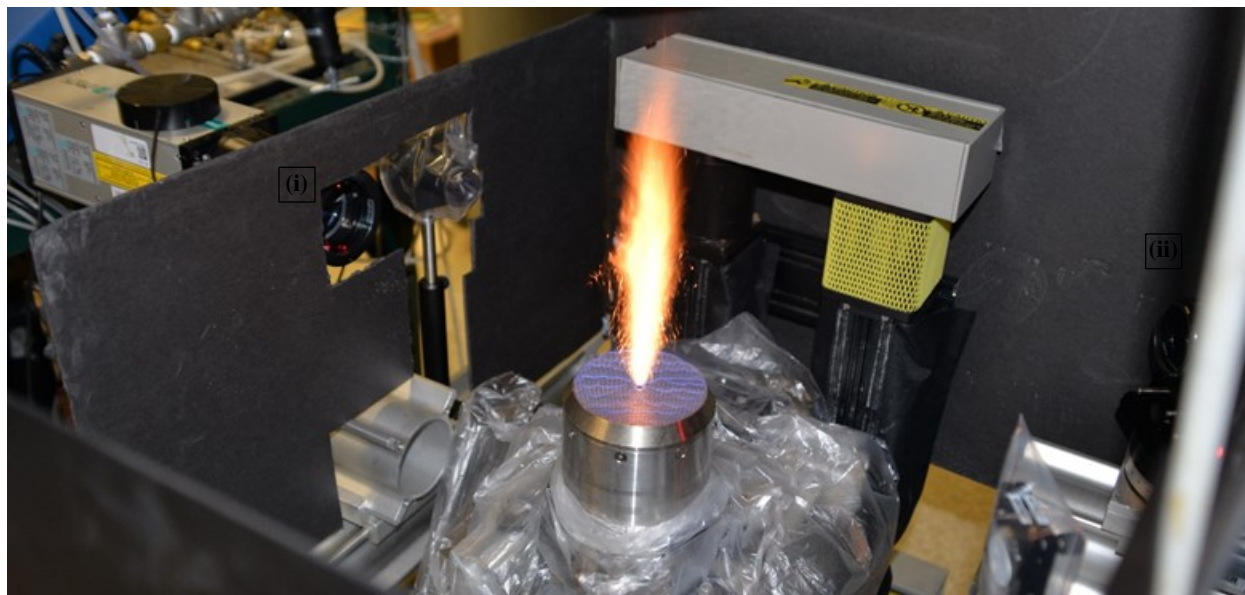
Fig. 18-Photograph of the experiment with a flat flame co-flow of premixed propane and air at $\phi = 0.69$. Oriente crude oil is spraying through the nozzle at a rate of 10 mL/min and an air loading ratio of 6.8. The laser transmitter (i) and receiver (ii) are shown.

Ignition Delay

In the course of our combustor tests at CBD, we observed a significant ignition delay with all of the oil mixtures, especially with the emulsion of 50% synthetic seawater. This contrasted with how the laboratory flat flame burner performed. In our previous reports, the co-flow burned propane and air at an equivalence ratio (ϕ) of 0.69, where ϕ is defined as the actual fuel-air ratio (F/A) to the stoichiometric fuel-air ratio (F/A)$_{stoic}$, detailed in Appendix A and Ref. [21]. Air and propane at $\phi = 0.69$ have an adiabatic flame temperature of nearly 1860 K (2890 °F), as calculated by Chemkin [22]. As we have observed in the laboratory, this creates an almost negligible ignition delay at the base of the spray plume.

In order to produce lower temperatures, we needed to burn either a mixture of hydrogen and propane or pure hydrogen. We decided to burn pure hydrogen, since the experimental setup and control is simpler. From a similar spray combustion study by O'Laughlin *et al.*[23], we know that by decreasing the co-flow temperature to the range of 1200 K to 1400 K, we would be able to observe noticeable ignition delay, or spray plume lift-off from the flat flame burner surface. In order to produce this behavior in the laboratory, we needed to reduce the temperature of the annular co-flow surrounding the spray plume.

Hydrogen has a lean flammability limit of $\phi = 0.18$ [21], but there are a number of laboratory issues with hydrogen. First, a pure hydrogen flame luminesces in the ultraviolet (OH) and infrared (H$_2$O) light wavelengths, but not in the visible. In simpler terms, it is invisible when it burns. UV or infrared imaging, light diffraction, or temperature measurement are common methods to detect hydrogen flames. In contrast, propane-air flames luminesce in the visible wavelengths from CH radicals. Hydrogen also has a very fast flame speed, making it potentially dangerous in any enclosed environment or duct. We addressed the flame

20

invisibility by monitoring the flame with an infrared camera. The rapid flame speed is addressed by reducing ϕ to reduce both the flame speed and the flame temperature.

(a)

(b)
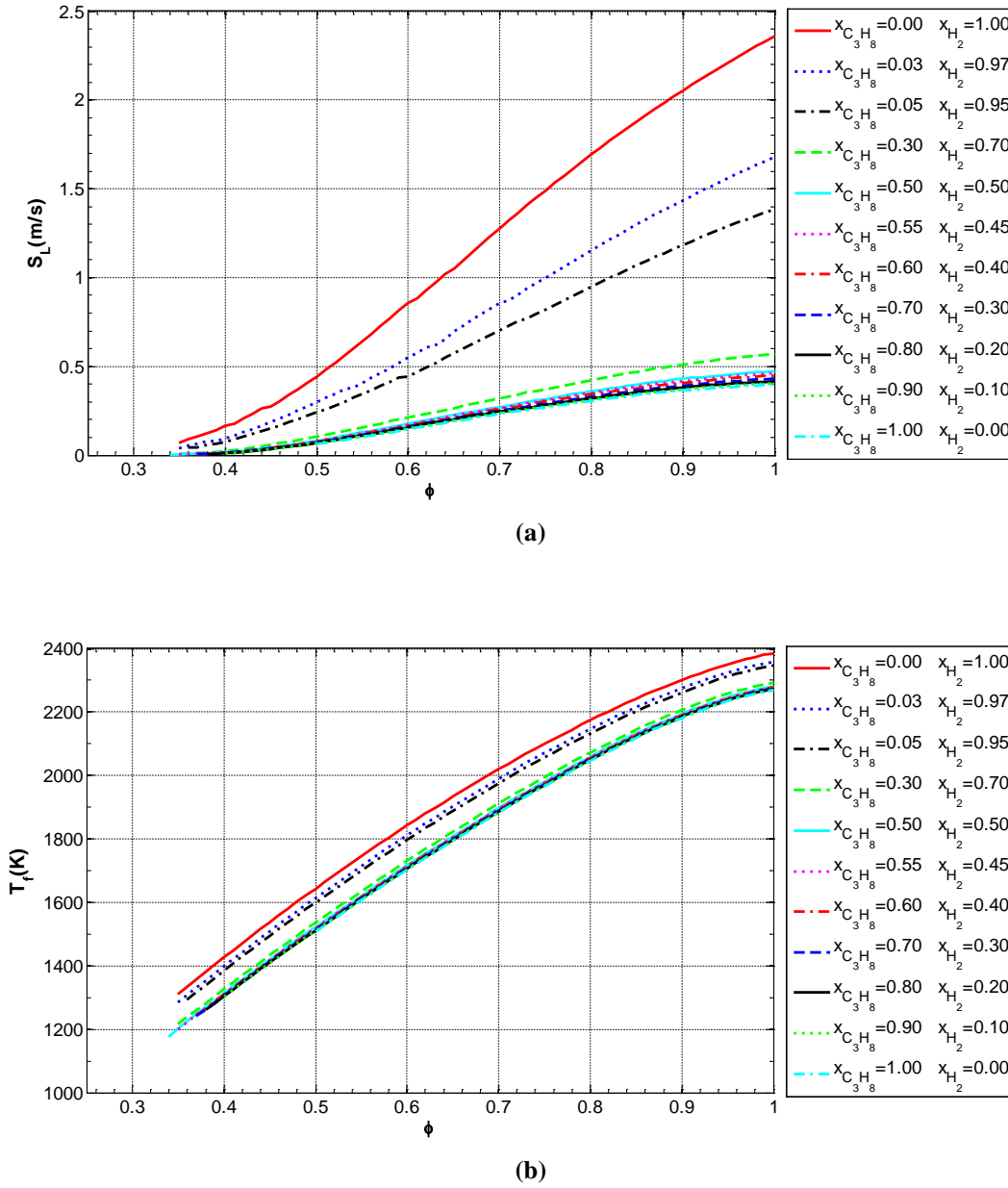
Fig. 19-(a) Predicted flame speeds and (b) flame temperatures for a range of propane and air mixtures, ranging from pure hydrogen to pure propane, using Chemkin.

Figure 19 shows the flame speeds and temperatures, as predicted by Chemkin [22], for a range of mixtures of propane, hydrogen, and air. These plots allowed us to anticipate the temperature and flow rates for the hydrogen flames we used to create an ignition delay.
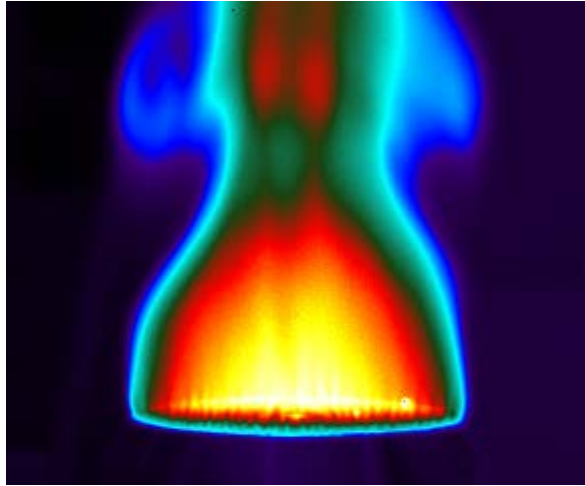
| (a) | (b) |
| Infrafred view of hydrogen flame | Infrared view of cold burner |
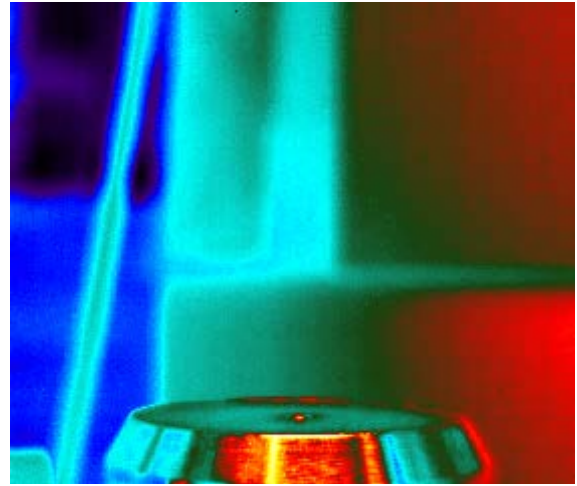
Fig. 20-IR view of a hydrogen flame (a), at $\phi = 0.30$, with an adiabatic temperature of 1190 K. A (b) room temperature view is shown for reference.

After changing the propane plumbing over to hydrogen, we examined the resulting flame. We first examined a very low equivalence ratio, since we were concerned with the safety of hydrogen in the laboratory and we anticipated that the recirculation zone temperature in the actual burner would be low. The flame in Fig. 20 was at $\phi = 0.30$. Using GasEq, an equilibrium combustion temperature code [24], we predicted an adiabatic flame temperature of 1190 K.
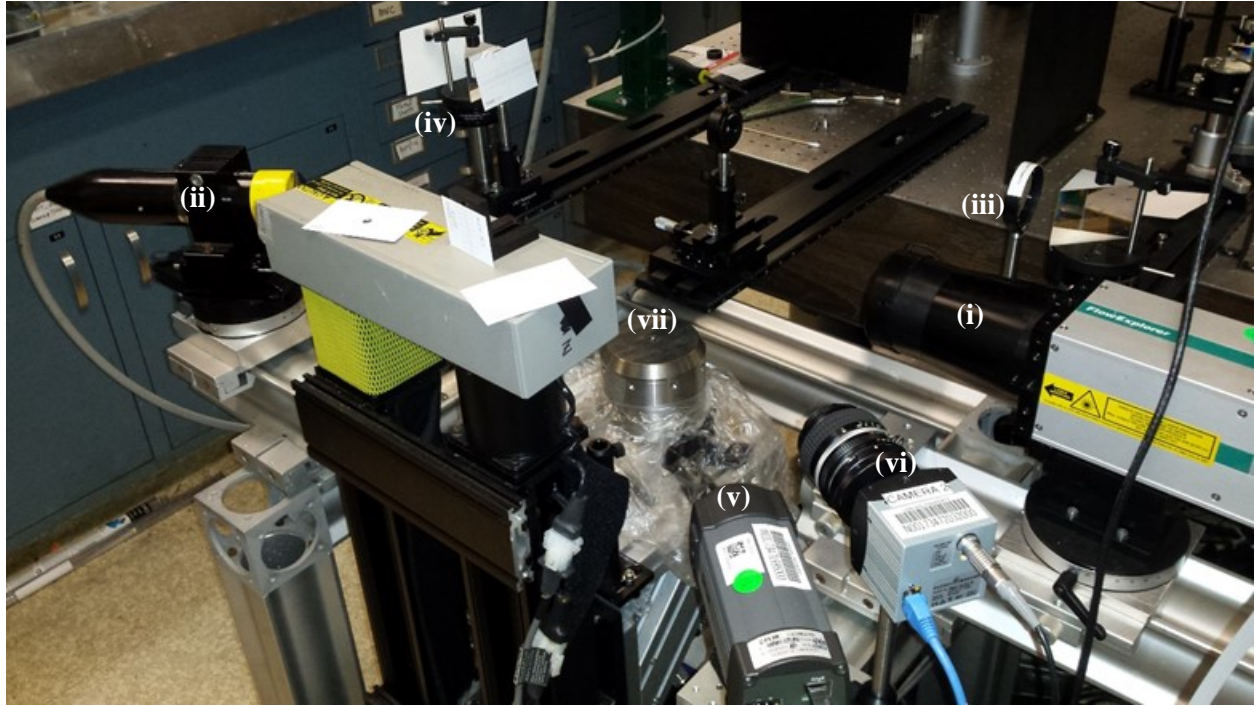
Fig. 21-Photograph of the instrumentation layout that surrounded the laboratory spray burner. These include the PDA transmitter (i), PDA receiver (ii), CARS transmission optics (iii), CARS receiving optics (iv), IR camera (v), high-speed visible camera (vi), and spray burner (vii).

(a)	(b)	(c)
Near-field image calibration	**Far-field image calibration**	**Example still-frame of flame**
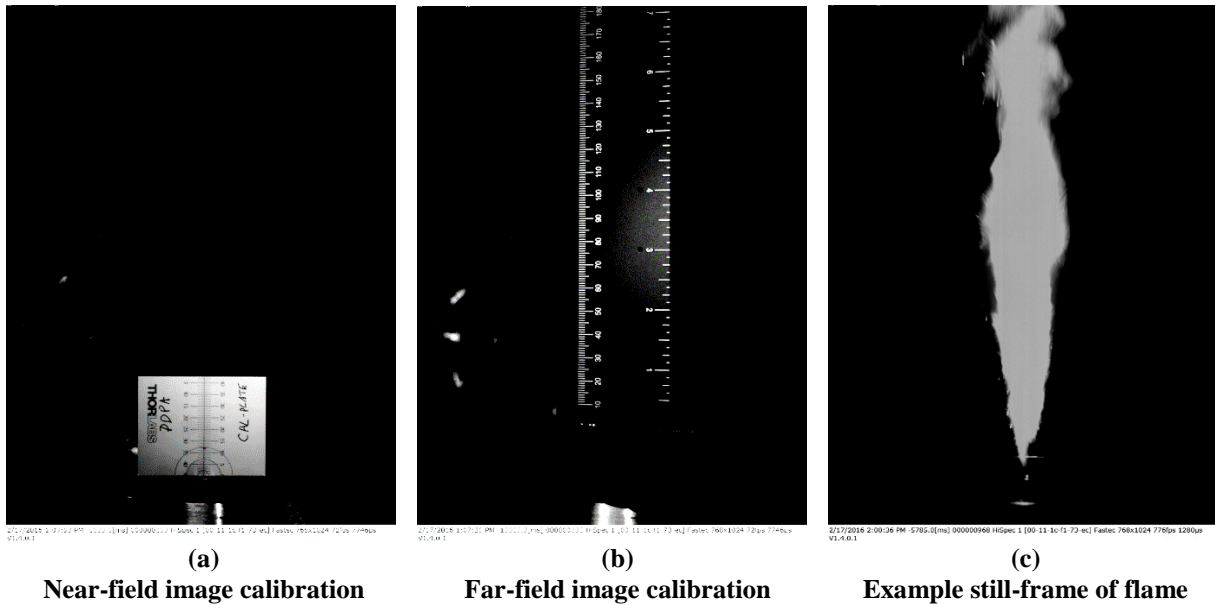
Fig. 22-Images of the (a) base calibration plate, (b) extended calibration, and (c) high-speed still of spray flame corresponding to an air flow 1.4×10^{-4} kg/s with an ALR of 1.62 with ANS.

In order to conduct this experiment, we needed to measure the lift-off height; the distance between the atomizer and the flame anchoring region. In order to make this measurement, we placed a high-speed camera and focused it toward the spray plume, with the centerline of the camera aligning with the base of the atomizer exit.

The high-speed visible camera (HighSpec I) recorded the instantaneous flame anchor height. We calibrated the spatial variation of the pixels with local and wide view calibration, as shown in Fig. 22. Flame lift-off studies were performed at air flow rates of 1.1, 1.4, 1.7, 2.0, 2.3, 2.6, and $2.9x10^{-4}$ kg/s. For each air flow, we examined an ALR of 0.5, ~0.7, 1.0, ~1.7, and 3.0. The ALR correspond to the sub-scale testing conditions, described in Table 3. The mass flow also corresponded to the area-scaled mass flows examined in the sub-scale burner.

We calibrated the image to determine the length of each pixel and then we queried each image, using a Matlab script. We summed the pixel intensities across each row (horizontal) of pixels and then set a threshold, above which we assumed was the location of the flame. The image below, Fig. 23, shows one of the images we captured and a plot of the horizontally-binned pixel intensities. The threshold is set to 150 arbitrary units (a.u.) of pixel intensity. The location where the threshold is exceeded is recorded for each image and then averaged for the entire set. The peak located at 0.03 m corresponds to a reflection of the flame emission from the top edge of the flat-flame burner.

(a)
Binary flame image

(b)
Row-integrated profile of flame intensity
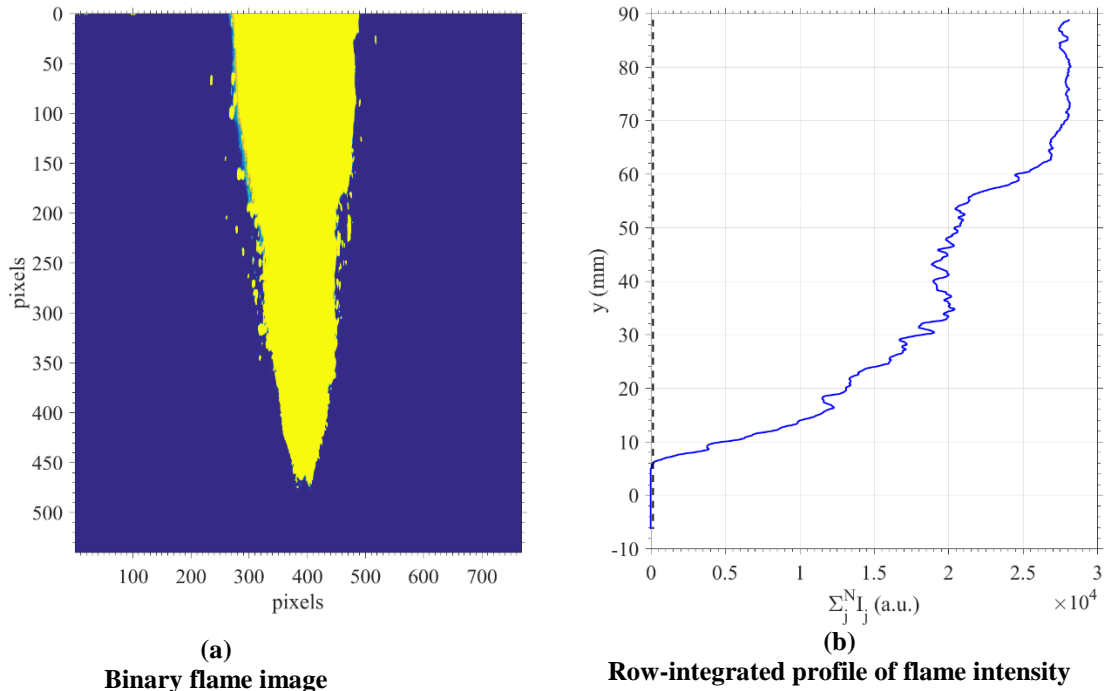
Fig. 23-(a) Example binary flame image with $\dot{m}_{Air} = 1.11x10^{-4}$ kg/s, $\dot{m}_{Oil} = 2.21\ x10^{-4}$ kg/s, and the (b) row-integrated pixel intensities summed horizontally across the image, with a threshold of 150 au defining the flame height.

We set an intensity threshold corresponding to the estimated visible flame anchor height that was set to all images in the series. The mean flame anchor height was then calculated, stored in a table, and then plotted as a function of air flow. We programmed into the data acquisition control system the ability to fix

the ALR and then independently adjust the airflow rate. From each video frame, we extracted the minimum flame height to produce a series of instantaneous flame heights. The averages from each set revealed how the flame anchoring changed with air flow, ALR, emulsion fraction, and weathering.

Laboratory Oil Weathering

To determine the effect of time on crude oil properties and how that may relate to combustion, we designed an experiment to simulate an aging process by using sparged nitrogen. This process was designed to simulate the weathering process that occurs when the spilled oil is exposed to air, but not the photochemical reactions of the spilled oil as it reacts with sunlight nor the chemical reactions of the oil as it reacts with compounds in the environment, including those in seawater, freshwater, soil, and the associated geology and biology. Therefore, the laboratory weathering process we used here was design to isolate the influence of the evaporation of the oil only, not the chemical changes. The resulting laboratory weathered oil provided test stock for emulsification and burn testing with the laboratory burner. Specifically, we wanted to understand how the weathered oil, with and without emulsification, burned in comparison to the neat oil.

We conducted small-scale or proof of concept tests with glass spargers to aerate the crude oil samples with dry nitrogen. A sparger is a tube or pipe with an exit composed of a porous, sintered glass exit. When the exit is immersed into a liquid and gas flows through it, small bubbles form at the exit that float upward and out of the fluid. Small bubbles produce higher surface area interaction than large bubbles, allowing greater evaporation of volatile constituents. Once we developed the process, we built hardware to conduct larger-scale aeration. Full tests used an 8 L container. Figures 24 and 25, below, illustrate the components:
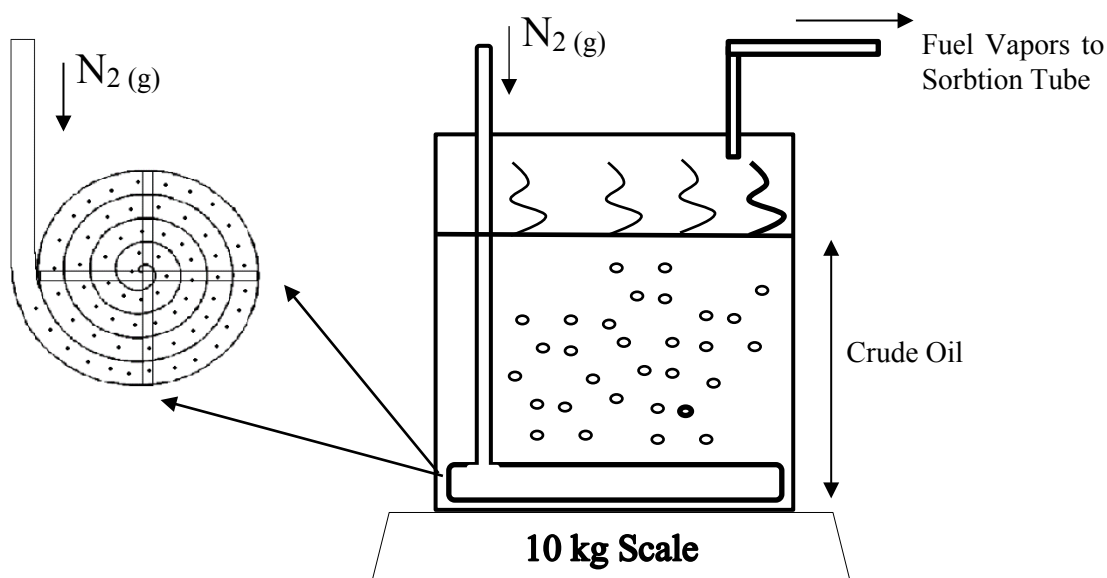
Fig. 24-Experimental design of crude oil weathering apparatus.
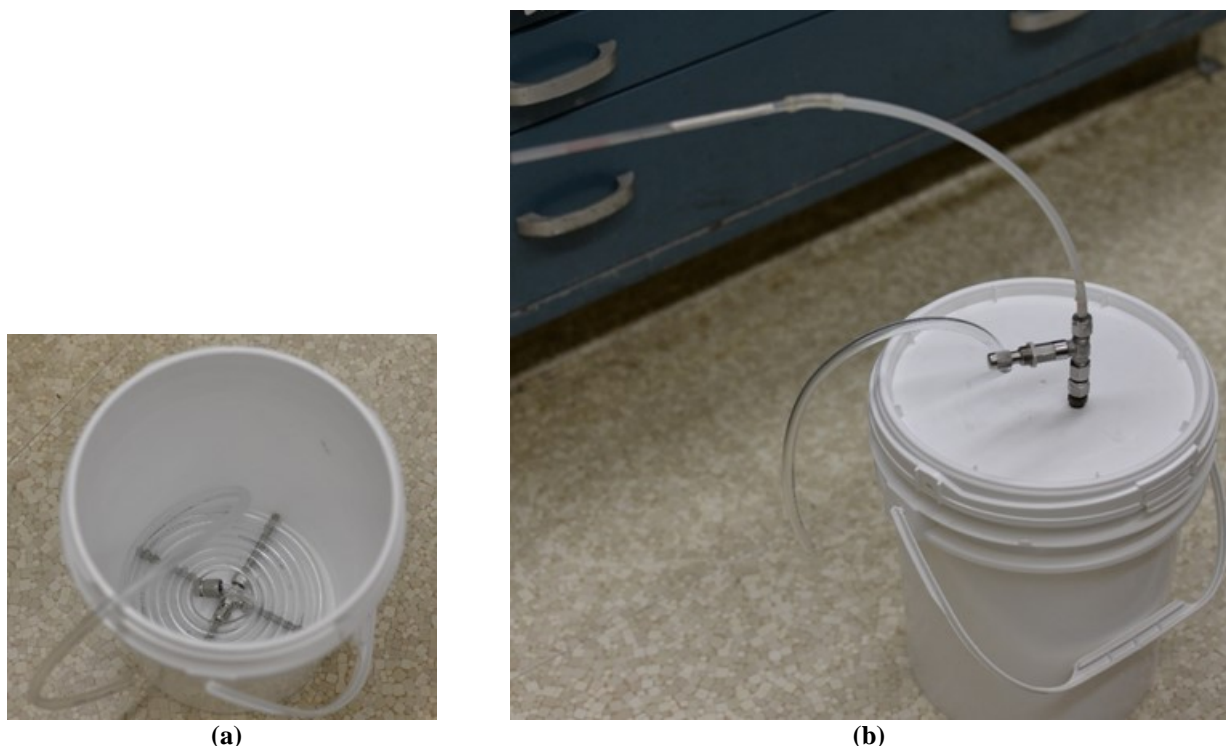
Fig. 25-Inside (a) and outside (b) of the weathing container.

The larger-scale sparger was composed of flexible tubing, coiled around a metal cross and that we placed in the bottom of an 8 L container. The diameter of the tubing coil matched the diameter of the container and the metal cross acted as a weight to ensure the tubing remained at the bottom of the container. Perforations along the length of the tube and a cap on the end ensure that the nitrogen gas bubbled uniformly across the oil in the container. A lid covered and contained the nitrogen-entrained vapor and forced it to flow through a sorbent tube. The entire apparatus rested on a 10 kg scale, allowing the mass of the empty and then full apparatus to be measured and recorded during the weathering process. The bubbled nitrogen captured fuel vapors of lighter hydrocarbons in the crude oil and let them escape through the hole in the top of the bucket. The evaporation reduced the initial mass of the crude oil. The mass was recorded every 30 minutes. Nitrogen was turned off to record the mass and turned on after the value is recorded. Samples were collected after a 10% reduction in mass to assess chemical composition and physical properties of the weathered crude oil.

Coherent Anti-Stoke Raman Spectroscopy

Coherent anti-Stokes Raman scattering (CARS) spectroscopy is a four-wave mixing technique whereby the Raman active transitions of a molecule are stimulated by a pump and Stokes beam and a signal is scattered by a probe beam [25]. The spectrum in the CARS signal carries a signature of the temperature and concentration of the molecules in the probe volume. In this study, we measured the temperature and concentration of N_2 in the flame at various parametric conditions. Similar measurements of N_2 thermometry have been performed previously in turbulent combustors and flames [26,27]. Additionally, the spray burner sat on a traverse to allow three-dimensional translation and study of the flame. Therefore, temperature and concentration of N_2 were to be probed in the radial and axial directions from the center of the flame.
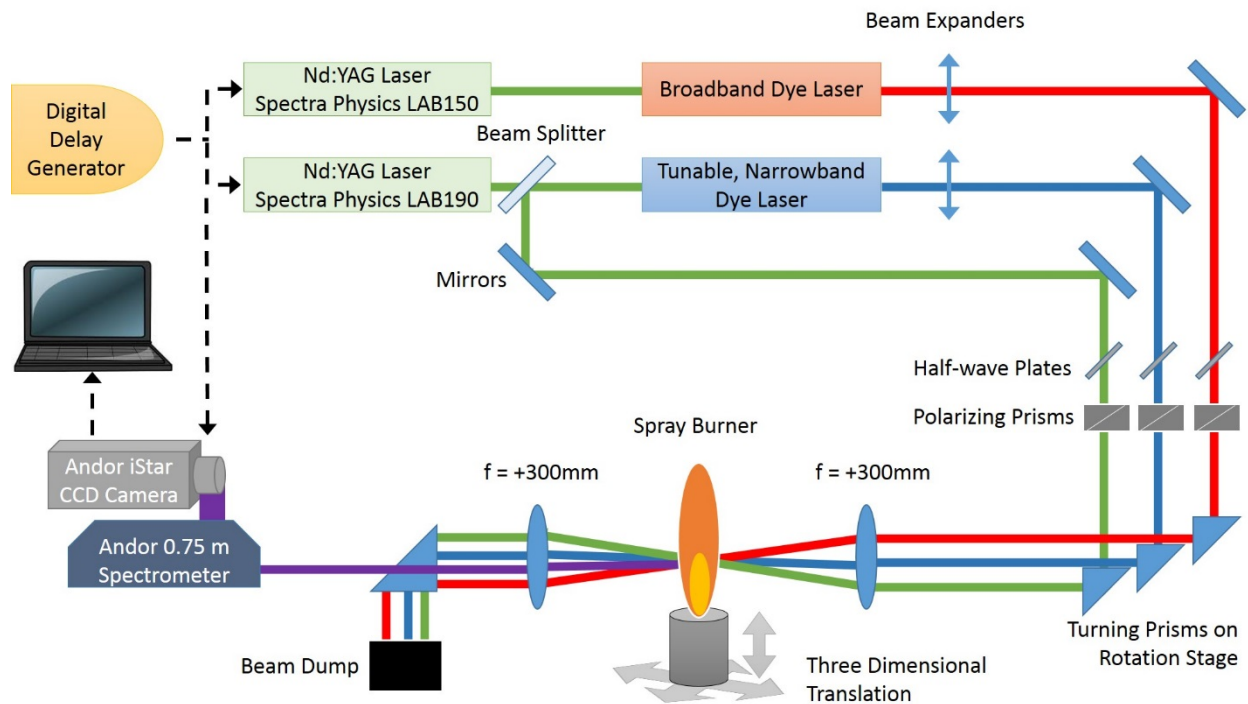
Fig. 26-Schematic diagram of the DPCARS and spray burner system.

In dual-pump CARS (DPCARS) the concentration of other molecules can be interpreted with respect to the concentration of N_2 [28]. DPCARS makes use of a tunable, narrowband dye laser in combination with the a broadband dye laser to pump and probe the Raman active transitions of a secondary, and sometimes tertiary, molecule and simultaneously generate its spectrum in the vicinity of the N_2 spectrum. We expected to measure the concentration of CO_2, and possibly that of O_2 and H_2 depending on their availability in the flame and the signal-to-noise ratio achieved with the CARS system [26,27].

Typically, the second harmonic of a Nd:YAG laser is used to pump the dye lasers and generate the broadband, Stokes beam and the tunable, narrowband probe beam in addition to providing the pump beam at 532 nm. However, this could have lead to a significant decrease in beam energies adversely affecting the signal-to-noise ratio. In this study, we synchronized and utilized two separate Nd:YAG lasers to generate these beams in order to maintain high energies in each beam and improve the signal-to-noise ratio of the CARS spectrum.

The schematic diagram in Fig. 26 illustrates the generation of the Stokes beam and the tunable, narrowband probe beam from the dye lasers which were pumped by the second harmonic of two synchronized Nd:YAG lasers. In addition, a third beam was split from one of the Nd:YAG lasers to provide the pump beam. The energy and polarization of the beams were controlled by half-wave plates and polarizers. Three prisms were mounted on two-axis tilt and rotation stages with high sensitivity to carefully orient the three beams into the flame. A lens with focal length of +300 mm converged the beams creating a probe volume within the flame. The CARS signal was generated (purple beam) from the probe volume and another lens with focal length of +300 mm was used to realign the beams. Finally, the CARS signal was collected with a spectrograph and charge-coupled device (CCD) camera system. A Stanford Research Systems digital delay generator (DG535) was used to synchronize the Nd:YAG laser lamp and Q-switch triggers as well as the Andor iStar CCD camera.

The synchronization of the lasers and camera was such that the pulse of each beam reached the focal point within the flame simultaneously, within 2 ns, and the camera was triggered to detect the CARS signal. This was important for various reasons. Each laser pulse was 10 ns and they must overlap in space and time in order to generate the CARS signal. With the digital delay generator, the delay in the pulse of one Nd:YAG laser may be controlled very carefully with respect to the other. As part of this procedure at a location where the three beams meet, photodetectors measured the scatter of each pulse against a white surface and an oscilloscope showed the temporal position of each pulse. The digital delay generator was then used to move the pulse of each beam closer to each other.

The same Nd:YAG laser was used to pump the 607 nm and provide the 532 nm beams, as shown in 6. In this case, the digital delay generator could be used to separate pulses in each beam. However, mirrors were used to create a delay in a pulse spatially. Approximately 0.3 m (1 ft) provides a delay of 1 ns. This technique was applied in a number of locations, as shown later.
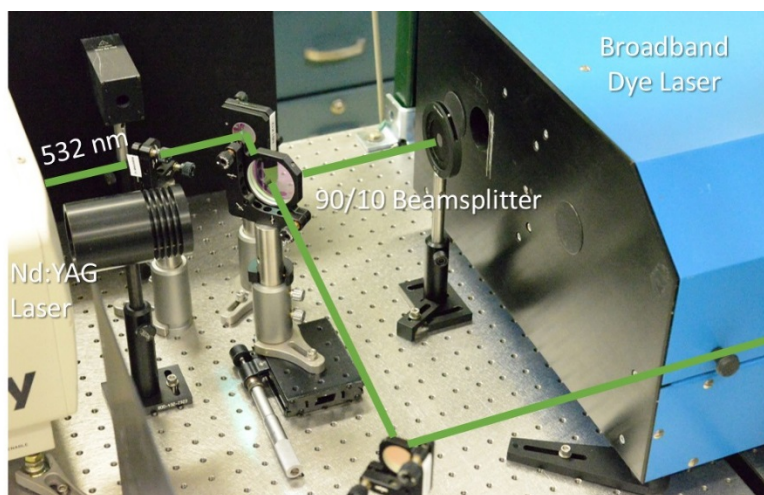
Fig. 27-Image demonstrating the pumping of broadband, dye laser at 607 nm with the Nd:YAG laser. A beamsplitter is used to pick 10% of the beam and provide the 532 nm beam.
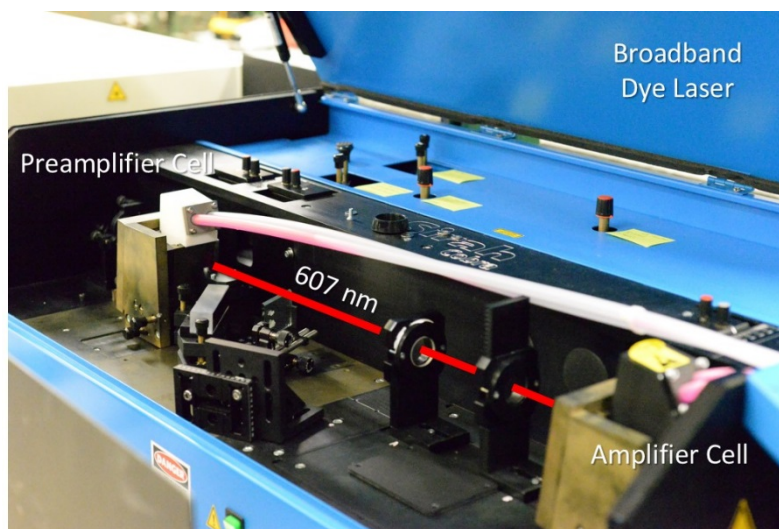
Fig. 28-Image of the preamplifier and amplifier cells in the broadband, dye laser.

Most of the Nd:YAG laser energy was used to pump the broadband, dye laser since the efficiency of the dye was at most 25%. To generate the beam at 607 nm, Rhodamine 640 (55 mg) and Rhodamine 610 (10 mg) were mixed in 750 mL of methanol. The solution ran through the preamplifier cell shown in Fig. 28. As prescribed in the manual, the concentration of dye in methanol needed to be diluted in the amplifier. Therefore, a third of the concentration was used.

The dye laser had to be modified to provide a broadband beam. As part of the oscillating cavity, a grating is generally used to narrow the bandwidth of the laser, but we removed and replaced it with a broadband mirror to generate a broadband beam.
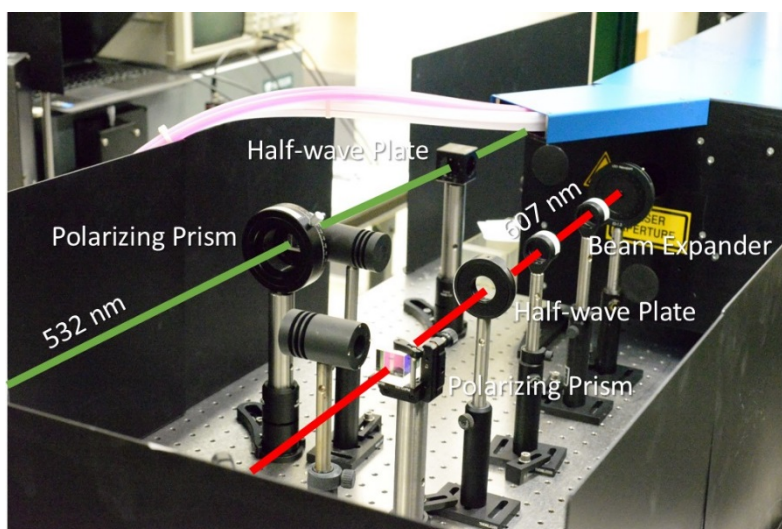
Fig. 29-Image demonstrating the half-wave plate and polarizing prisms for the 532 (green line) and 607 nm (red line) beams.

When pumped, the broadband, dye laser at 607 nm had a square profile, approximately 4 mm x 4 mm. To stay within the damage threshold of the optics and to make its profile comparable in size to the 532 nm beam, the 607 nm beam was passed through a beam expander composed of two spherical lenses, shown in Fig. 29, increasing its profile size to approximately 6 mm x 6 mm. Each beam also passed through a half-wave plate and polarizing prism, which provided the capability of adjusting the intensity of the passing beam.
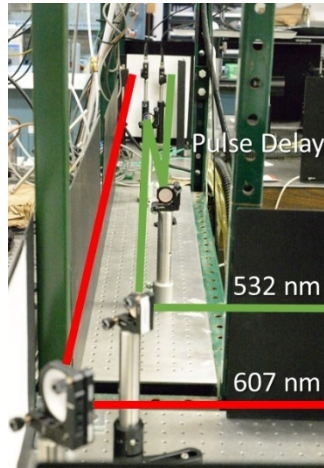
Fig. 30-Image of the pulse delay created spatially with two mirrors on the 532 nm beam.
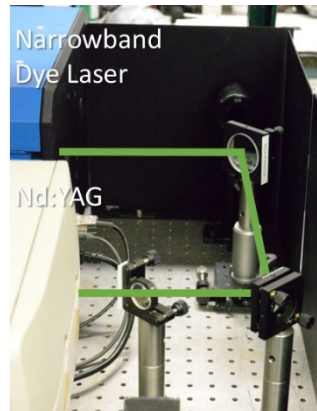
Fig. 31-Image of Nd:YAG laser pumping narrowband, dye laser.

As previously discussed, the temporal overlap of the beams was crucial. Two mirrors were used, shown in Fig. 30, to delay the 532 nm pulse spatially with respect to the 607 nm, such that the beams struck a white surface on the other side of the table simultaneously, within 2 ns. Two photodetectors, also shown in Fig. 30, collected the scatter from the beams.

Because one Nd:YAG laser did not have the sufficient energy to pump two dye lasers and also provide 532 nm light, a second Nd:YAG laser was used to pump the narrowband, dye laser as shown in Fig. 31.
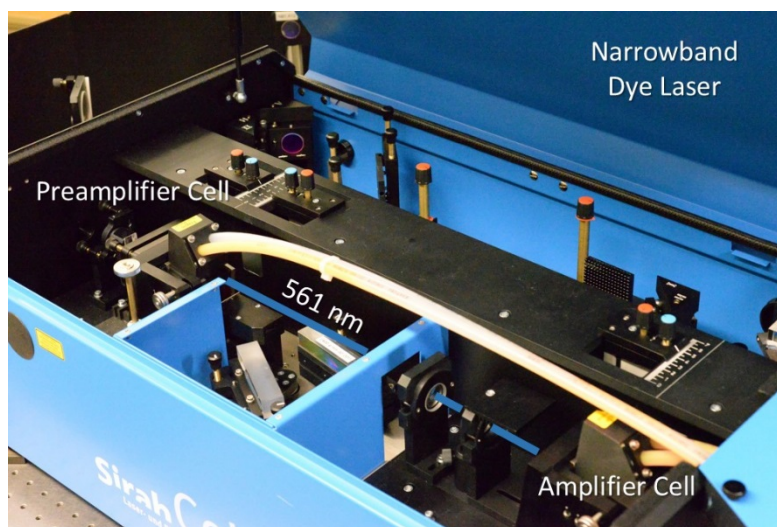
Fig. 32-Image of the preamplifier and amplifier cells in the narrowband, dye laser.

The internal components of the narrowband, dye laser, shown in Fig. 31, were the same as the broadband, dye laser with one exception: a grating was used rather than a mirror as part of the oscillating cavity. Also, the dye used to generate the 561 nm beam was Rhodamine 590 (20 mg) in 1 L of methanol. A third of this concentration was used in the amplifier as in the broadband, dye laser.
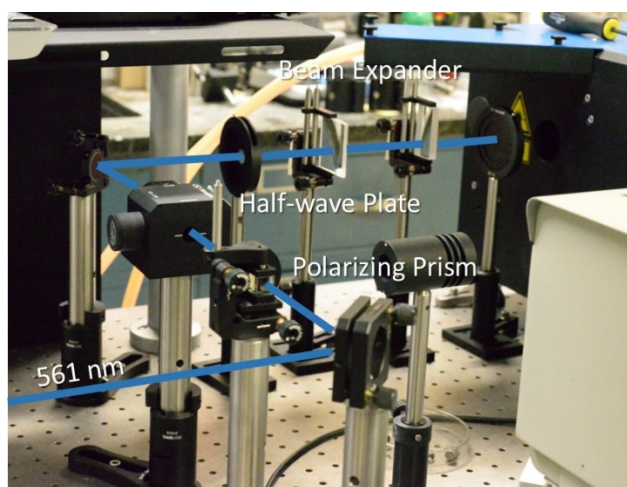
Fig. 33-Image of the beam expander, half-wave plate and polarizing prism through which the 561 nm beam passes.

The profile of the 567 nm beam was rectangular. As a result, two cylindrical lenses were used increasing its size to approximately 5.5 mm x 5.5 mm. The beam then passes through a half-wave plate and polarizing prism, shown in Fig. 33. Because the 561 nm beam was generated using a second Nd:YAG laser, the digital delay generator could be used to synchronize the arrival of the its pulse with respect to the 532 and 607 nm beams. The beam struck a white surface near the location where the other two beams strike and a photodetector was used to observe its delay on an oscilloscope.
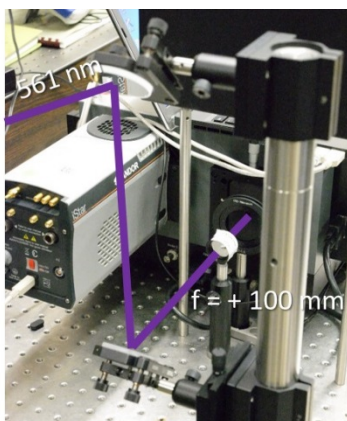
Fig. 34-Image of instruments collecting CARS signal showing spectrograph entrance slit and CCD camera.

An Andor iStar CCD camera, coupled with an Andor 0.75-m spectrograph collected the CARS signal. As shown in Fig. 34, the CARS signal was directed by two mirrors through a focusing lens (f = +100 mm) into the entrance slit of the spectrograph. The camera was triggered by the digital delay generator to receive the CARS signal. Finally, a laptop was used to control the spectrograph and record the data from the camera.

Analytical Chemistry Methods

A range of analytical methods revealed the distribution of the hydrocarbons and chemical species in the crude oil, weathered crude oil, and exhaust. These will be described in turn to provide the reader some familiarity with the basic methods and their results.

Mass spectra of the crude oils were obtained with a Waters Xevo TQD mass spectrometer, using a combination Atmospheric Solids Analysis Probe (ASAP). The ASAP provides rapid direct analysis of volatile and semi-volatile solid and liquid samples using atmospheric pressure ionization. Crude oil samples were deposited onto glass melting point tubes by dipping them into the fuel. Operating conditions include a scan range of 150 to 1500 m/z, cone voltage 40 V, source temperature of 150 °C, capillary current of 6.5 mA, collision cell energy of 2 V, desolvation gas flow of 350 L hr^{-1}, and a cone gas flow of 30 L hr^{-1}. The ASAP probe was heated with a temperature ramp from 100 °C to 600 °C over a time period of 15 min. The ASAP probe provides the mass spectrum of every ionizable organic constituent in the crude oil and thus gives an indication of the distribution constituency by molecular weight.
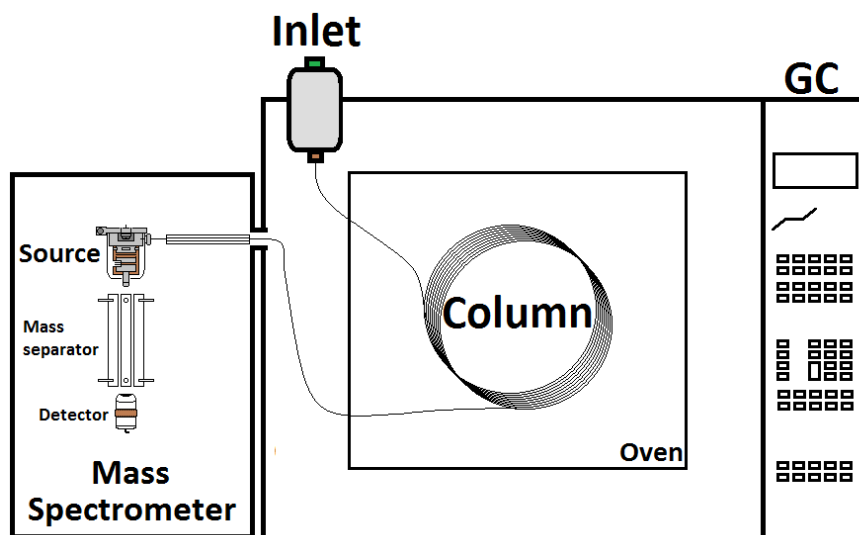
Fig. 35-Simplified diagram of a GC-MS system

In order to analyze what constituents are evaporating from the crude sample under simulated weathering by nitrogen gas washing, an analytical technique called gas chromatography (GC) was used. GC, shown in Fig. 35, is a useful method for looking at volatile material that is or can easily be heated into the gas phase. A sample is injected into a heated inlet, carried through a glass capillary column which is held in a temperature-controlled oven that can raise and lower the temperature precisely. The column is very narrow, typically with an inner diameter of 0.530 to 0.150 mm, and internally coated with a material that is selected to interact with the analytes in the sample. Compound structure, boiling point, polarity, and other properties will cause analytes to interact with the column coating differently, leading to different elution times from the end of the column. In order to "see" these eluting compounds a detector is required. There are various types of detectors that can be used with a GC that will show a peak each time an analyte exits the column. Generally the integrated area under the peak is representative of the concentration (volume percent) of that analyte in the sample, although exact concentration values (mass percent) requires calibration. A very powerful type of detector is a mass spectrometer (MS). A mass spectrometer is a type of instrument that can separate and measure the mass to charge ratio (m/z) of an ion. In the case of a standard GC-MS, the compound exiting the column is ionized through bombardment with electrons, separated based on m/z ratio, and detected. At each point in the chromatogram we can look at all the ions within a given range. Each compound will fragment and create a unique pattern of ions that can be reference to a MS database for rapid compound identification.

Collecting and sampling gaseous material requires a different approach. Typically gaseous samples are dilute and hard to inject into a GC-MS system. In order to concentrate and inject material in the vapor phase, one method is to trap that material onto a specially made material that has an affinity for the type of sample you are interested in. Once that material is trapped on the surface on the sorbent, we can then heat it removing the material that absorbed to the surface and elute the material into a GC inlet where is can be separated and analyzed by the MS detector.

Headspace analysis of evaporated crude oil samples were collected using 6 mm Grestel Tenax TA thermal desorption tubes that captured the evaporated material. The GC used for headspace analysis was an Agilent 7890 connected to a Joel AccuTOF GCv mass spectrometer. Samples were injected using a Gerstel thermal desorption system (TDS) connected to a Gerstel split/split-less CIS IV cryo-cooling GC

33

inlet. The TDS temperature was ramped from 100 to 300 °C with an adsorption flow of 150 mL min^{-1} onto a Tenax sorbent liner in the CIS IV inlet, which was cryogenically cooled to -10 °C. The CIX IV inlet was ramped at 12 °C min^{-1} to 250 °C and held for 4 min. The inlet used a split ratio of 100:1. The column flow rate was 2.2 mL/min helium operating in a constant flow mode. The column used was a Restek 60 m x 250 µm x 0.25 µm Rxi-1ms capillary column. The oven temperature program began at 30 °C for 2 min, then ramped at 5 °C/min to 150 °C with a 4 min temperature hold, and this was followed by a 50 °C/min ramp to 320 °C with a 6 min temperature hold. The MS acquisition time was 32 min with a total run time of about 40 min. The transfer line to the MS was held at 250 °C. The MS used electron impact ionization (EI) with a source temperature of 230 °C. The mass range scanned was between 35 and 300 m/z with a collection rate of 0.5 ns and a solvent delay of 5 min.

The exhaust measurements using the Alaska North Slope (ANS) crude oil were taken using a ¼" SS rake approximately 50 cm above the plume. Sample was drawn into a Gerstel tenax (10x) sorbent thermal desorption tube. GC-MS data were collected by heating the sorbent tube in a Gerstel thermal desorption system (TDS) inlet. As the temperature rises, different compounds evaporate at different times, which are then transported into the GC-MS system.

RESULTS

This section presents and discusses the experimental results for both the practical-scale and laboratory-scale experiments. The practical scale results reflect the engineering effort of developing the combustor and are focused on that objective. In contrast, the laboratory scale efforts are focused on understanding the fundamental behavior of crude oil as it is emulsified, weathered, sprayed, ignited, and burned.

Table 3-Scaling from sub-scale to laboratory and engineering scale

Sub-Scale Tests					D_o	0.510 in	13.0 mm	
					A_o	2.043E-1 in^2	1.32E-4 m^2	
	$\dot{m}_{Air}$ (kg/s)	$\dot{V}_{Oil}$ (L/min)	$\dot{m}_{ANS}$ (kg/s)	ALR$_{ANS}$	$\dot{m}_{ORN}$ (kg/s)	ALR$_{ORN}$	$D_{venturi}$ (in)	
Ignition	1.0E-2	1.0	1.5E-2	0.68	1.5E-2	0.66	0.177	
78% Full	2.5E-2	1.0	1.5E-2	1.71	1.5E-2	1.64	0.177	
78% Full	2.5E-2	2.0	2.9E-2	0.85	3.0E-2	0.82	0.177	
Full	3.2E-2	3.0	4.4E-2	0.73	4.6E-2	0.70	0.177	
Laboratory Tests					D_o	0.055 in	1.4 mm	
					A_o	2.376E-3 in^2	1.53E-6 m^2	
	$\dot{m}_{Air}$ (kg/s)	$\dot{V}_{Oil}$ (mL/min)	$\dot{m}_{ANS}$ (kg/s)	ALR$_{ANS}$	$\dot{m}_{ORN}$ (kg/s)	ALR$_{ORN}$	$D_{venturi}$ (in)	
Ignition	1.2E-4	11.6	1.7E-4	0.68	1.8E-4	0.66	0.022	
78% Full	2.9E-4	11.6	1.7E-4	1.71	1.8E-4	1.64	0.022	
78% Full	2.9E-4	23.3	3.4E-4	0.85	3.5E-4	0.82	0.022	
Full	3.7E-4	34.9	5.1E-4	0.73	5.3E-4	0.70	0.022	
Engineering-Scale Tests					D_o	1.010 in	25.7 mm	
					A_o	8.012E-1 in^2	5.17E-4 m^2	
	$\dot{m}_{Air}$ (kg/s)	$\dot{V}_{Oil}$ (L/min)	$\dot{m}_{ANS}$ (kg/s)	ALR$_{ANS}$	$\dot{m}_{ORN}$ (kg/s)	ALR$_{ORN}$	$D_{venturi}$ (in)	
Ignition	3.9E-2	3.9	5.7E-2	0.68	6.0E-2	0.66	0.25	0.354
Comp. Full	6.7E-2	2.7	3.9E-2	1.71	4.1E-2	1.64	0.25	0.354
Comp. Full	6.7E-2	5.2	7.9E-2	0.85	9.6E-2	0.82	0.25	0.354
78% Full	9.8E-2	3.9	5.7E-2	1.71	6.0E-2	1.64	N/A	0.354
78% Full	9.8E-2	7.8	1.1E-1	0.85	1.2E-1	0.82	N/A	0.354
Full	1.3E-1	11.8	1.7E-1	0.73	1.8E-1	0.70	N/A	0.354

Table 3 shows the operating conditions for the three scales of investigation: sub-scale, laboratory, and engineering. The sub-scale tests have set the baseline operation, from which the other sizes have been scaled by the nozzle area. This assured that the exit velocities were nearly equal, such that at the base of the spray plume, the shear between the ambient air and the plume is the same. But, because the nozzle diameters vary between 1.4 mm and 25.7 mm, the bulk behavior was different. In particular, the surface to volume ratio of the reacting flames (surface) and plume (volume) were different. The surface increased with (Length)^2,

while the volume increased with (Length)³. Therefore, the convective mixing of heat and momentum with the environment was faster for the smaller, laboratory-scale burner. As a result, we could expect greater flame lift off and more instability with the laboratory burner. Furthermore, the burning spray plume was enclosed by a shroud that limited mixing with the ambient air while providing radiative heat transfer back to the plume while convectively heating entrained air. As a result, we could expect better flame holding with the practical scale burner. Even with these differences, the practical-scale and laboratory-scale testing inform one another and provide valuable engineering insight and fundamental scientific understanding of the spray combustion behavior of emulsified crude oil.

Sub-Scale Burner Component and System Performance

The results we present in this section follow the development process, starting with the atomizer and proceeding with the plasma torch, initial testing of the assembled sub-scale and engineering-scale burners, performance testing, and refinement of the ignition process.

Atomizer Operability and Performance

Fig. 36-Photograph of the LFBA atomizer test at an ALR = 0.91, performed at CBD. Airflow was 3.2×10^{-2} kg/s and the water flow rate was 2.1 L/min, or 3.5×10^{-2} kg/s.

The spray testing evaluated the performance of the four different spray nozzles to determine which produced the most appropriate spray plume for the burner study. Because the spray medium was water, which is environmentally benign, we directed the plume onto the grass on the north side of the testing platform, or deck, as shown in Fig. 36.

Table 4-Atomizer evaluation test plan.

Test #	Liquid	Atomizer	Air flow (kg/s)	Minimum Water Flow (L/min)	Air Loading, by mass
1	Water	L-FBA	3.2×10^{-2}	2.1	1-0.2
2	Water	VT-FBA	3.2×10^{-2}	2.1	1-0.2
3	Water	LS-FBA	3.2×10^{-2}	2.1	1-0.2
4	Water	HS-FBA	3.2×10^{-2}	2.1	1-0.2

Table 4 shows the test plan for the nozzle testing. We were not able to use the phase-Doppler anemometry system to measure the droplet formation and plume behavior because the system is at our DC laboratory, nor is it suited for environments with uncontrolled humidity and temperature.

(a) LFBA   (b) VTFBA   (c) LSFBA   (d) HSFBA
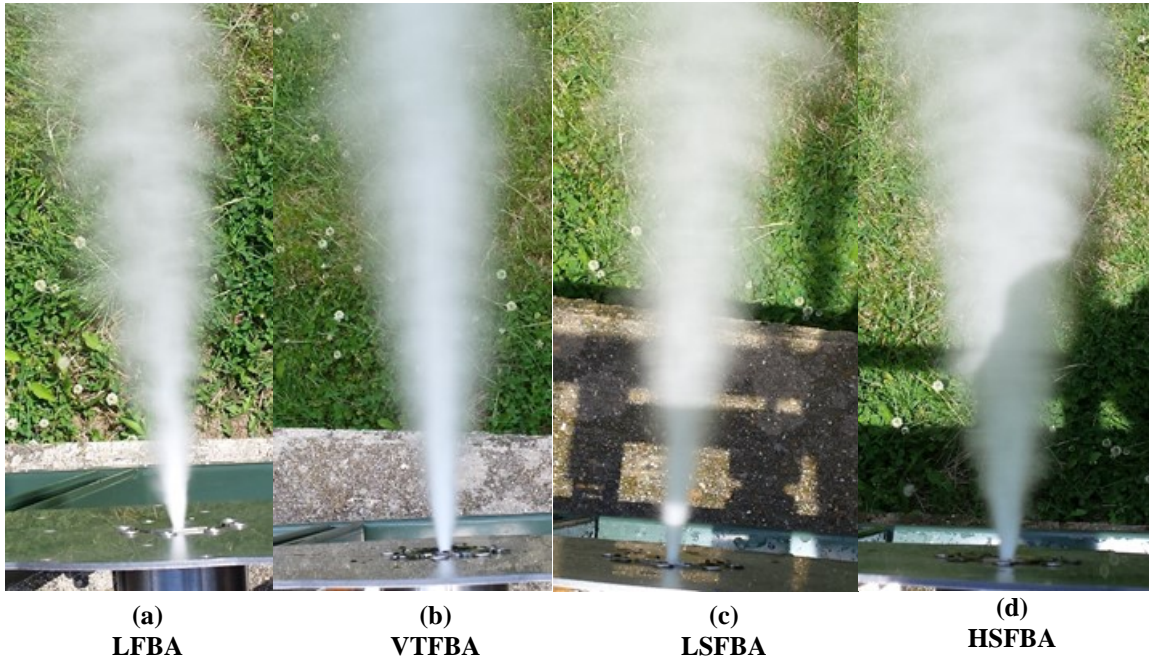
Fig. 37-Spray plumes from the four configurations of the atomizer nozzle: (a) conventional, (b) VTFBA, (c) LSFBA, and (d) HSFBA. All test were performed at the same conditions: airflow at 3.2×10^{-2} kg/s, water flow rate at 2.1 L/min, or 3.5×10^{-2} kg/s.

Figure 37 shows photographs of the spray plumes from the four nozzles. Though the pictures show subtle differences between the plumes, there is slight indication of plume broadening in the VTFBA nozzle, while the HSFBA nozzle broadened the plume even more. We observed that all of the atomizers produced fine mist sprays at an ALR of 1.0 that transitioned to a coarser mist, containing mm-scale droplets at an ALR of 0.3. We also observed that the HSFBA produced finer droplets at smaller ALR, 0.5, than was observed with the other atomizer tips. A broader plume will mix more rapidly with the surrounding air, entraining more oxygen and recirculated hot combustion gases to initiate and stabilize combustion. Fine droplets at a lower ALR will allow greater oil flow rates while maintaining efficient atomization. Given the broader plume and

finer droplets produced by the HSFBA, we moved forward with that design as the atomizer of choice for burn testing.

Plasma Torch Operability
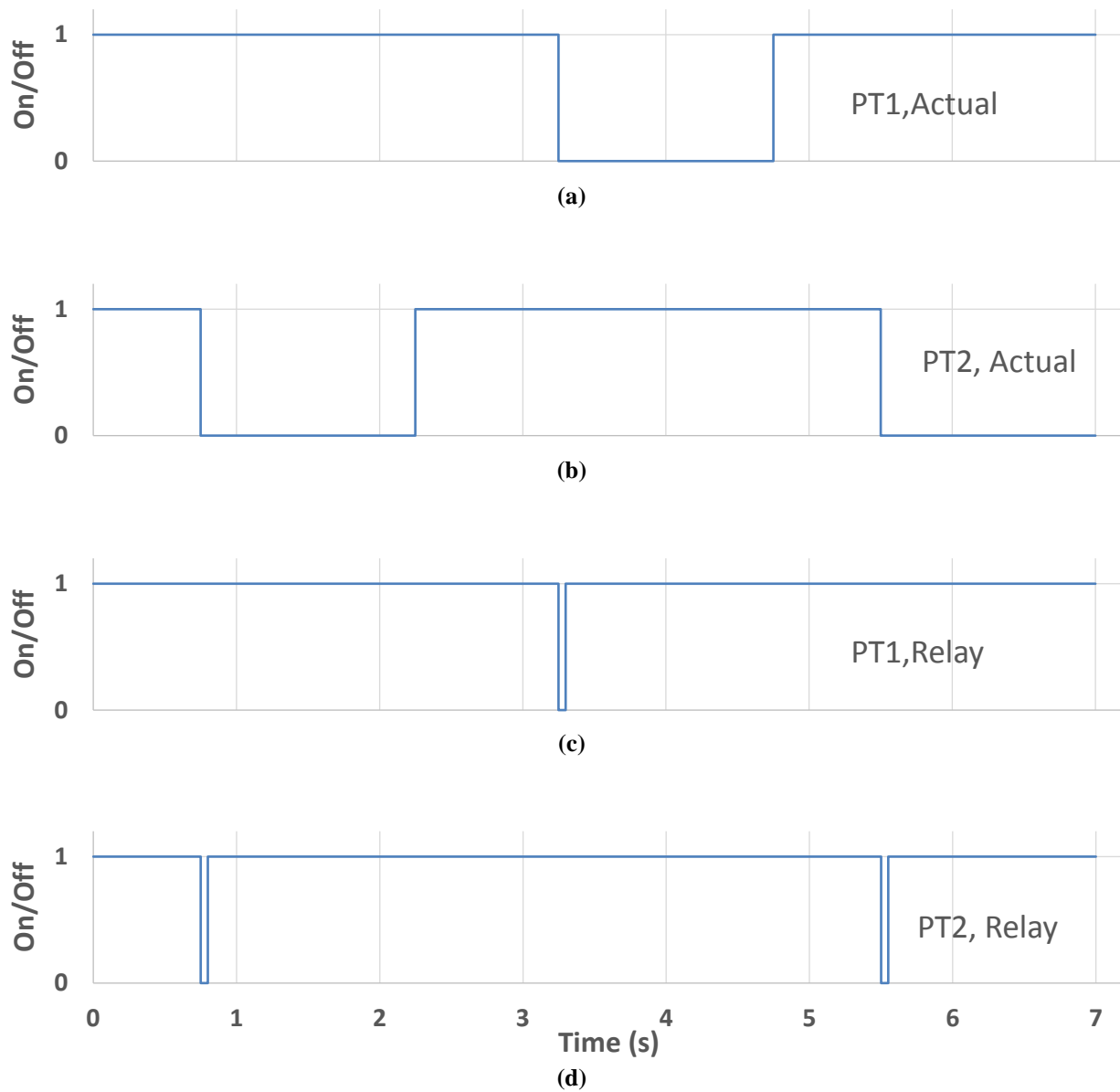
Fig. 38-Plasma torch activation (on/off) over time: (a) torch 1 plasma stream, (b) torch 2 plasma stream, (c) torch 1 relay signal, and (d) torch 2 relay signal.

The Miller plasma torches were designed to cut metal, but we had to adapt their operation for this application. During startup, the torches first use a high frequency (~ kHz) alternating current (AC) to establish an arc inside the torch nozzle and expel the high-temperature, ionized gases for 3.25 seconds. Then, they switch to high voltage (~kV) direct current (DC) to cut the metal. The grounded metal acts as a

cathode, while the torch acts as an anode. If there is no metal to act as a cathode, the torch turns off and conducts a 1.5 second cooling procedure.

In order to use the plasma torches to continuously supply hot ionized gases, we had to establish the timing and switching between the two to always maintain at least one torch on. Figure 38 shows the actual torch streaming and the controlling relay signals over time. A full period lasts 4.75 s, with a 50 ms switch-off period, as shown in Fig. 38c and d.

Burner Operability and Testing

We performed burner operability testing incrementally to examine how the burner ignited and stabilized and what influenced and enhanced that behavior. Burner geometry variations and emulsion fractions were the variables fixed during set up, then the air and liquid flows were varied to examine their influence on ignition, stability, and flame characteristics.

(a) 1 L/min **(b) 2 L/min**
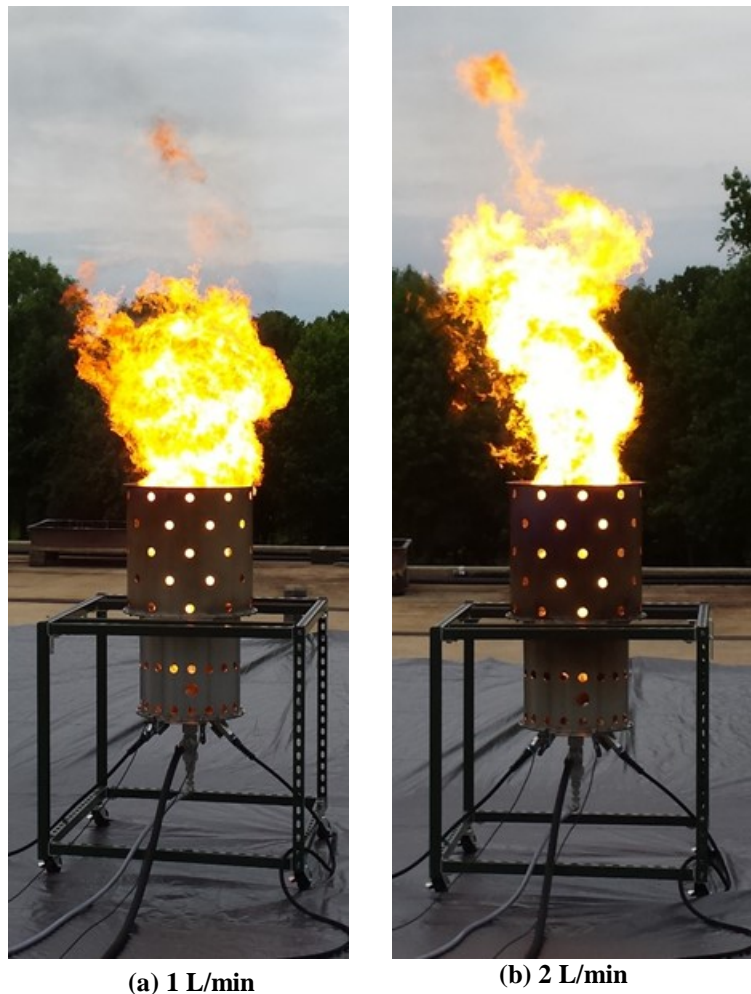
Fig. 39-Spray plume flames at an air flow of 2.0×10^{-2} kg/s and Oriente oil flow rates at (a) 1.0 L/min and (b) 2.01 L/min, for air-liquid ratios of 1.3 and 0.65, respectively.

Figure 39 shows the results from the first ignition and burn tests. Only the single 1st and 2nd burner stages were used. The test conditions for Fig. 39a and b are 2.0×10^{-2} kg/s of air with oil flows of 1.0 and 2.01 L/min (air-liquid ratio of 1.3 and 0.65), respectively. In both cases, there were no residual droplets that escaped the burn plume. This contrasts with the concept demonstration studies, wherein there were unburned droplets for ALR's of 1.0 and less. In this case, there were visible soot emissions, without residual crude oil droplets. This indicates that the HSFBA was effectively atomizing the crude oil and that there was sufficient heat produced by the spray flames and reflected back to the plume by the combustor shroud to evaporate all and burn most of the crude oil mixture.

The soot in this and following studies may be from two possible sources. In the process of burning conventional fuels, soot is formed by incomplete combustion of hydrocarbons and the subsequent formation of mono-, then polycyclic aromatic hydrocarbons (PAH), followed by their agglomeration into solid particles. In particular, the incomplete combustion of aromatics within a fuel increases the formation and agglomeration of soot particles [21,29]. The presence of asphaltenes in the crude oil is another source of solid carbonaceous particulates. Asphaltenes do not evaporate, but as bituminous compounds, undergo pyrolysis much like coal. Therefore, the visible soot may be a mixture of PAH soot from incomplete hydrocarbon combustion and the remnants of asphaltene pyrolysis.

(a) 2 L/min   **(b) 4 L/min**
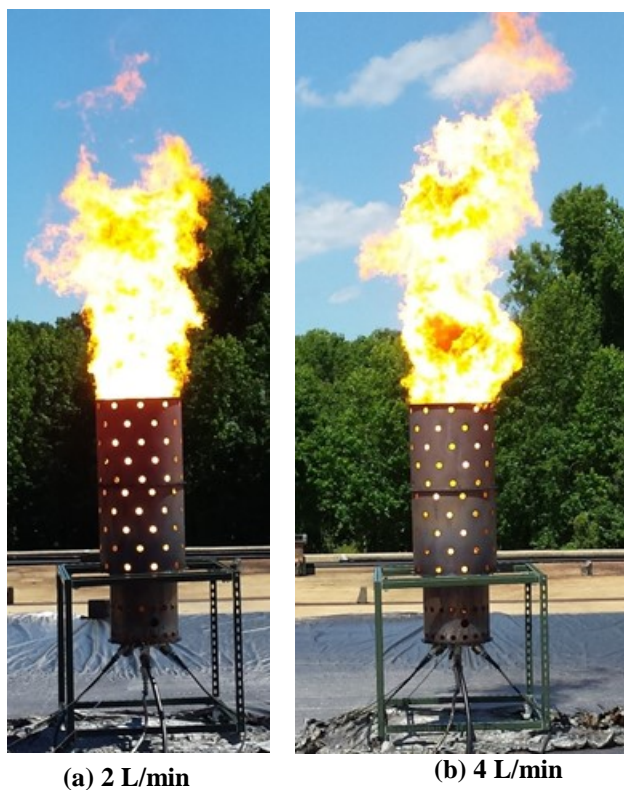
Fig. 40-Spray plume flames at an air flow of 3.2×10^{-2} kg/s and (a) pure Oriente crude flowing at of 2.0 L/min for 1.0 ALR and (b) a 25% synthetic seawater and Oriente emulsion flowing at 4.0 L/min flow for 0.47 ALR.

In a following test, we used two large, second stage burners. This geometry change appeared to produce less soot with pure crude oil. We also tested emulsified Oriente crude oil, with 25% synthetic seawater and observed that the emulsion appeared to burn with less soot than pure crude oil to flow rates

up to 4 L/min. The possible reduction in soot can be understood by the additional atomization emulsified droplet undergo as the water vaporizes. As observed in the concept demonstration study and by Ocampo-Barrera *et al.* [1,30], water in the emulsion flash vaporizes and creates droplets smaller than the original spray produced, which evaporate more rapidly, and thus allows more rapid and complete burning.

Figure 40 shows the burn behavior with the full assembly of two large second stage burners, with an airflow of 3.2×10^{-2} kg/s. Fig. 40a shows Oriente crude being burned at 2.0 L/min while Fig. 40b shows a 25% emulsion being burned at 4.0 L/min. Both appeared to produce the same amount of soot, but we can see some significant differences. First, the pure crude oil heated the combustor shroud to higher temperatures, which we can see by the hot, red metal. We also notice that the pure crude flames stabilized slightly higher along the length of the plume. This change in height is a visible indication of ignition delay; the time it takes for the spray plume to heat with recirculated hot combustion gases, mix with fresh air, and begin burning. It is counter intuitive that the spray mixture with more water ignites earlier, but there are some logical explanations. First, the water in the emulsified droplets would boil at much lower temperature than much of the hydrocarbons, causing additional atomization, which would produce smaller oil droplets, which evaporate faster. In fact, evaporation times scale with D^2K, where K_{evap} is an evaporation constant and D is the droplet diameter:

$$\tau_{evap} = D^2 K_{evap} \tag{3}$$

We should also note that the liquid flow rate for the emulsion mixture was twice that of the pure crude, which will approximately double the bulk spray (air and liquid) velocity, which would in turn, double the entrainment and mixing rates. The same flow rate could not be used with straight crude without the risk of inefficient, or inadequate atomization, as we observed with the atomizer test.

From this operability test and comparison, we can make some significant observations. First, emulsification, at least up to 25%, aids in stability and performance because the rapid water evaporation drives a secondary atomization process. Since spilled oil usually has an appreciable moisture content, this behavior is an advantage. The cooler combustion process may also help the durability of the combustor, since the emulsified crude burns cooler, but there is a greater risk for corrosion, since heat increases salt corrosion rates of stainless steels [31-33]. Comparing the flame lengths in Fig. 39 with Fig. 40, we also notice that the plume 2.0 L/min is shorter for an air flow of 2.0×10^{-2} kg/s and a shorter combustor than it is for 3.2×10^{-2} kg/s and a taller combustor. This difference suggests that the second stage combustors need additional holes or larger holes to entrain more air.

We note that the diameter of the burning spray plume was contained entirely within the burner shroud in Fig. 40. If the burn plume had spread outside of the shroud, we could assume that the spray plume needed additional space to spread out or needed additional air. At low fuel flow rates, the plume burns some distance from the walls of the burner and will not extend far from the exit of the shroud. At higher flow rates, the plume extends downstream to allow greater mixing length and there is greater soot production. This will be explored in greater detail during the performance testing.

In order to test higher emulsion fractions, we reconfigured the geometry of the burner to increase the entrainment and mixing of air and to examine different ignition locations, as shown in Fig. 42. We placed a medium 1st stage section upstream of the burner configuration we had already tested. This created three annular recirculation zones to increase air entrainment and mixing to enhance flame stability and propagation. We also installed the side ports for mounting the plasma torches.

We first tested with pure Oriente crude oil and observed that the plume would not ignite with the torches at any of the side-mounted ports. We suspect that along the greater distance the plasma jet must travel to reach the plume, the hot jet had mixed with enough air that it is not hot enough to produce ignition.

Therefore, we moved the plasma torches back to the bottom of the combustor shroud. We were then able to produce stable ignition with pure crude and we observed that the plume stabilized lower in the combustor.

Fig. 41-Reconfigured burner burning an assumed-50% emulsified crude oil, with an air flow of 1.60×10^{-2} kg/s and a liquid flow rate of 0.75 L/min, for an ALR of 1.32.

Once combustion had heated the shroud and burned off any unburned crude that accumulated inside, we switched the flow over to a mixture we estimated was 50% emulsified Oriente. We combined this mixture during the previous concept demonstration phase of this research. The burner, as Fig. 42 shows, produced stable combustion, with flame anchoring dependent on the plasma torches.

The emulsion was a mixture of synthetic seawater, Oriente crude oil, each at 50%, with an addition of Tween® 85, Span® 85, and Corexit® 9500. We observed that the addition of 50 mL Corexit® 9500 into the volume of 10 L of crude oil and seawater, Span® 85 and Tween® 85, with mixing by a paint mixer and a hand-held drill motor for 5 minutes, produced a smooth emulsion without separation. The test shown in Fig. 42 burned the entire 10 L mixture. Given that the plume was contained entirely in the burner, we can assume that there was sufficient oxygen from the atomizing air and the entrained air for stable combustion. The asymmetry in the flame is due to the influence of the plasma torches.

We later mixed up a larger batch of 48 L with only Corexit®, with the assumption that the broader range of surfactants would emulsify the seawater-oil more effectively. We observed that we were not able to emulsify the mixture sufficiently by using the hand-held drill motor. Therefore, we used a floor drill press to emulsify the mixture of synthetic seawater, Oriente crude oil, and 600 mL of Corexit® (1.667%). Two hours of mixing formed an emulsion that appeared to stay stable for more than two hours. A number of tests using the burner configuration in Fig. 42 were not able to produce stable combustion. We observed that burning residual oil along the length of the burner provided heat to stabilize combustion, but once that residual oil burned away, the plume extinguished or burned intermittently. We tried moving the ignition torches further away from the plume and varied the liquid and air flow rates, but none of these steps produced stable combustion. When we examine the interaction of the plume with the plasma torches, we could observe local combustion and noticed there was not enough heat released to form propagating flames along the plume.

The lack of stable combustion without external heat addition, and the poor flame propagation at the base of the plume, suggests that the plasma torches are not able to raise the temperature sufficiently to ignite this emulsified spray plume. This occurs because the evaporating water cools the mixture of atomizing air, oil vapor, oil droplets, and plasma air to temperatures less than 700 – 1000 K. At higher temperatures, the ignition delay is short enough to initiate and propagate combustion.

At least three possible reasons may explain the inconsistent results with the 50% emulsion. The first is that the older mixture had a lower emulsion fraction than we thought. The second, though related, reason is that the emulsion did not hold for the first or second batch of 50% seawater. The third reason is that the

original mixture, which contained a mixture of Span® 85, Tween ® 85, and Corexit® 9500, was a more stable emulsion.

The first possible explanation for this change in operability is that the older mixture used in the first successful test may have contained a smaller seawater fraction than we had assumed, lost during the initial test performed during the previous research. This is plausible since we were still learning how to effectively emulsify crude oil at high seawater fractions. Therefore, the initial testing done in 2014 may have consumed some of the seawater that separated out of the mixture, which in turn lowered the emulsion fraction.

The second explanation that the new emulsion did not hold long enough between mixing and testing, is reasonable. We conducted an emulsion test at two drill press speeds (250 and 500 rpm) with the remaining 50% emulsion mixture, which contains only Corexit® 9500, and extracted samples during mixing into 50 mL glass bottles. When mixed at both low and high speeds for more than an hour, the Orient 50% emulsion starts to separate within an hour. This suggests that by the time we blended the mixture and attempted the test, the mixture had already started to separate.

The third explanation, that Span® 85 and Tween ® 85 were more effective emulsifiers than Corexit® 9500, is revealed to be a reasonable explanation. A parallel laboratory study was conducted to examine the emulsion characteristics of Span® 85 versus Corexit® 9500 and is reported in the Emulsification sub-section of Laboratory-Scale Experimental Results. We also found that the second batch of 50% emulsion, after repeated mixing attempts, was not stable enough for reliable testing. In contrast, Dr. Rangwala's group has blended various emulsions of ANS and fresh water using a drill press at 700 rpm for 6, 12, and 18 hours and observed separation times on the order of days. They did not use any surfactant or emulsifying agent. For comparison, a 25% emulsion mixture of synthetic sea water and Oriente (ORN) crude oil, with a 2% Corexit® fraction, remained mixed for much longer. After 43 minutes of mixing at high speed, it only started to separate after 70 minutes. After 113 minutes of mixing, it remained mixed for more than an hour, allowing successful burn testing.

From the operational studies of 25%, assumed-50%, and actual 50% emulsion fractions, we also observed that ignition delay is a significant influence on the ignition and flame anchoring process of the spray plume. However, the sub-scale spray combustor is not ideal to measure that behavior. We will discuss this in detail in the sections covering the laboratory results.

Burner Performance Testing Results
We carried out performance testing to compare the performance of the burner with different emulsions and alterations. The second objective was to compare the spray burn emissions to those from *In Situ* burning. Figure 42 shows two plumes burning with the sampling rake in place. We performed the tests early in the morning, near sunrise, to assure that there was minimal wind to blow the plume away from the rake.
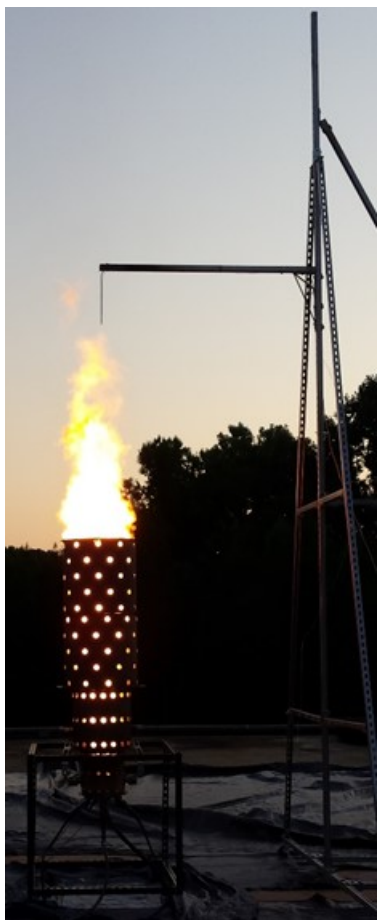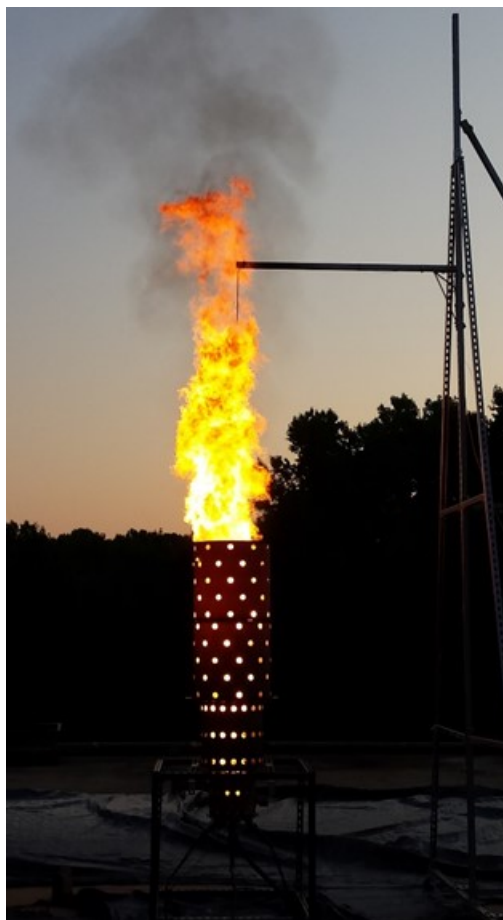
(a) 1 L/min　　　　　　　　　　**(b) 1 L/min**

Fig. 42-Spray plume flames burning with the sampling rake at an air flow of 2.5×10^{-2} kg/s and pure Oriente crude oil flowing at (a) 1.0 L/min and (b) 2.0 L/min. The soot is clearly visible in the higher flow rates.

Table 5-Soot measurement data.

Test	$\dot{m}_{Air}$ (10^{-2} kg/s)	V_{fluid} (L/min)	$\dot{m}_{Oil}$ (10^{-2} kg/s)	Oil	Emul-sion	ALR	Vacuum Flow (10^{-4} m^3/s)	Soot Gain (g)	Soot Rate (10^{-4} g/s)	Scaled Soot (10^{-4} kg/s)	Smoke Yield
1	2.50	2.00	3.05	ORN	0%	0.82	2.62	0.024	1.7	20	0.07
2	2.50	1.00	1.52	ORN	0%	1.64	4.08	0.016	*2.2	26	0.17
3	2.50	1.00	1.52	ORN	0%	1.64	2.47	0.002	0.12	1.5	0.01
4	2.50	1.00	1.52	ORN	0%	1.64	2.37	0.003	0.14	1.7	0.01
5	2.50	1.00	1.47	ANS	0%	1.71	3.57	0.005	0.38	4.6	0.03
6	2.50	1.00	1.47	ANS	0%	1.71	3.10	N/A	N/A	N/A	N/A
7	2.50	2.00	2.93	ANS	0%	0.85	3.32	0.006	0.50	6.0	0.02
8	2.00	1.33	1.57	ORN	25%	0.96	3.57	0.007	0.74	8.9	0.06
9	2.50	2.66	3.13	ORN	25%	0.60	3.63	0.010	0.77	9.2	0.03

* Unreliable

Table 5 shows the preliminary soot measurement data for a range of crude oil mixtures. There was some inconsistency in early tests with the accumulated mass and the volumetric flow rate. In order to eliminate the possibility of soot, accumulated in the rake tubing, from influencing the measurement, we blew out the tube with compressed air. We do not have an explanation for the inconsistency in the volume flow rate. Careful tightening of the adjoined lines helped, as we can see in the tests 8 and 9. In order to correct that issue, we calculated a gain rate, by dividing the mass gain by the duration of the sampling, normalizing by a vacuum flow rate of 3.57×10^{-4} m^3/s. This brings repeated measurements (3 and 4) closer in value with one another. A scaled soot rate is calculated by scaling the rake inlet to the combustor exit area, which is then divided by the mass flow of the oil to produce the smoke yield [34]. For comparison, an indoor In Situ burning study performed by NIST with an Alaska North Slope oil produced a smoke yield of 0.065 and 0.095 in two separate tests [35], which is appreciably higher than the 0.02 and 0.03. Their calculation method scaled from carbon emissions instead of an area balance, which is another accurate, accepted approach [35,36]. We should note some general trends in soot production. First, Oriente crude oil produces more soot than ANS crude oil. This can be traced back to the high asphaltene fraction and heavier hydrocarbon content in the Oriente (See Analytical Chemistry Results and Appendix A Crude Oil Assay). We also noticed there is less soot produced in the emulsified Oriente. We can trace this back to the improved atomization of emulsified mixtures [1,30]. Finally, soot content increases with greater fuel flow for a given airflow. This is a normal result of richer fuel-air mixtures [21,29].

Table 6-Temperature measurements in the recirculation zone along the centerline of the burner at different stages. The highest temperatures for each geometry are highlighted red.

Stage	Burner Configuration			Blocked Hole Row			$\dot{m}_{Air}$ (10⁻² kg/s)	$\dot{V}_{oil}$ (L/min)	Oil	E %	Temperatures									
	1st	2nd	3rd	1st	2nd	3rd					RZ1	RZ2	C1.5	C1.9	C2.0	C2.5	C2.9	C3.0	C3.5	C3.9
Size	L	L	None				2.50	1.0	ANS	0	339	349	297		300					
				B			2.50	1.2			466	475	346		592					
				B	B		2.49	1.0			522	539	358		599					
				B	B	B	2.50	1.0			661	721	425		779					
					B	B	2.50	1.0			463	524	408		607					
						B	2.50	1.0			449	456	457		568					
				B		B	2.49	1.0			403	404	326		373					
	M	M	L	B			2.49	1.0			543		604		1166	1398		1396	1397	
				B	B		2.46	1.0			498		605		1022	1185		1206	1207	
				B	B	B	2.50	1.0			526		757		1238	1416		1424	1408	
				B		B	2.51	1.0			530		641		1214	1392		1408	1410	
					B	B	2.50	1.0			487		634		1194	1401		1411	1414	
							2.49	1.0			639		556		1266	1372		1449	1428	
							2.51	1.0			612		600	526	846	1399	811	1498	1416	
							2.51	1.0		25	598		380	386	801	1377	689	1417	1389	
							2.50	2.0		0	716		665	548	706	1340	779	1465	1326	
							2.52	2.0		25	663		373	398	711	1253	494	1363	1300	
							2.50	1.0	ORN	0	740		460	1205	1301	959	1425	1473	1376	1320
							2.51	1.0		38	670		345	1026	1262	1077	1368	1403	1267	1170
							2.50	1.6		38	758		346	977	1267	912	1315	1322	1128	1234
							2.50	2.0		0	847		437	1080	1345	833	1342	1377	1191	1319
							2.50	2.0		38	809		347	989	1278	889	1304	1313	1113	1214

Until this point in the program, we had been examining two burner configurations: one with a large first stage and large second stage (LL) and another with a medium first stage, medium second stage, and large third stage (MML). Because of the move out of Bldg. C252, we were not able to make adequate soot measurements, so we needed a different performance metric. Since temperature is a good relative indicator of heat release rate, we placed thermocouples at similar locations in both burners to compare their performance, while blocking off the dilution holes that allow air to entrain into the plume. The first-stage burner contains three rows of dilution holes. We blocked, in turn, the first, second, and third row of holes in a number of permutations. Table 6 shows the temperature measurement results for the burner performance tests.

Temperature measurements are labeled with RZ or C prefixes, followed by numbers. RZ specifies that the thermocouple was placed in the recirculation zone. C specified the combustor. RZ1 was placed between the plasma torches, beside the spray nozzle, while RZ2 was placed directly behind a plasma torch. The combustor number specifies the stage and the placement within that stage. For example, C1.5 specifies the first stage, half-way up the stage.

Our objective was to determine the burner and hole geometries that created the highest first stage recirculation zone temperatures. This would indicate which geometry drove the greatest recirculation of heat from the plume to the flame anchoring regions, creating the largest spray evaporation region at the base of the burner plume. This process is especially important for emulsified crude oil mixtures.

After testing both burners and measuring their recirculation zone temperatures, we observed two different trends based on the first stage burner size as the air entrainment influenced both the temperature and the burner stability. The LL burner geometry showed the highest temperatures in the recirculation zone when we blocked all of the 1st stage holes, while exhibiting the greatest burn instability during ignition and ramp up. For the large first stage, we can conclude that blocking off more holes reduced the entrainment of the cooler air, which cools the recirculation zone, but inhibited the flame anchoring process during ignition and ramp up. This suggests that the recirculation zone in the large first stage burner entrains much more air and has a longer residence time and that the recirculation process does not carry as much hot products upstream, or they are cooled more, than the medium first stage burner.

In contrast, if we consider the MML burner, we observe that open holes allowed the greatest temperature in the recirculation zone and for most of the plume. We also observed stable combustion during ignition, ramp up of air and fuel flow, and during full flow. We can conclude that the greater air entrainment increased flame anchoring, plume burn rate, and the recirculation of hot products, without reducing the temperature in the recirculation zone.

We conducted later studies to examine the influence of liquid flow rates, emulsification, and compared the behavior of ANS and Oriente crude oils. Generally, we observed some consistent trends. First, emulsification reduced the recirculation zone temperature – a behavior that is not surprising. We examined emulsion fractions of 25.0% and 37.5% with ANS and Oriente crude oils, respectively. We observed a general decrease in temperature with increasing emulsion fractions and the liquid flow rate, since both increased the cooling effect of the water and flame weakening of the sea salts. Increasing the volumetric flow of the liquid also increased the plume velocity, which shortened the combustion residence time while increasing the entrainment of cool air. We also observe that for the same emulsion fractions, increasing the liquid flow rate increased the recirculation zone temperatures. This is best understood in context of the recirculation zone radiative heat transfer, which we will discuss later in this report.

Instead of testing a 50% emulsion, we opted instead to try a 37.5% emulsion. We discovered that with 2%, by volume Span® 85, the emulsion held for 16 days after two hours of mixing. We also found that ignition and stable combustion did not need to be preceded by burning only crude oil.

Burner Ignition

There are a number of changes in the ignition procedure that we adopted from laboratory-scale observations. Although we will not describe them in detail in this section, there are some major qualitative observations immediately relevant to ignition. First, we observed that the spray plume anchored lower with decreasing ALR. As the ALR increases, more light-weight hydrocarbons, which evaporate at lower temperatures, to mix with air and combustion products and burn. Furthermore, the flame radiation increases with decreasing ALR as more soot and asphaltenes in the flame radiate and transfer heat to the unburned droplets.

Applying these laboratory observations to the burner ignition process, we observed that ignition occurred more rapidly with a lower ALR. We also observed the need to decrease the plume velocity by using an air flow rate of 8.6×10^{-3} kg/s, but we found that increasing the oil flow rate to 0.5 or 1.0 L/min decreased the ignition time, even for a mixture with 25% or 37.5% synthetic seawater.

Summary

We successfully developed an operable, low pressure, low-soot burner that is capable of burning neat and emulsified crude oil for oil spill remediation. The nozzle and burner are capable of scaling from laboratory to practical dimensions, allowing the basic burner design to be adapted to a range of engineering requirements.

A number of design issues remain to be resolved that the sub-scale testing has brought to light. First, a steady-flow hot plasma torch is crucial to igniting and stabilized highly emulsified crude oils, especially those with fractions approaching 50%. Furthermore, the design we used for the sub-scale shrouds relied on rolled sheet metal welded to bolt flanges. The thermal expansion of the shroud body created structural strain that broke the welds between the shroud and flanges. Furthermore, the bulkhead between the combustor sections and the inlet bulkhead were all warped by the thermal strain. Given that these combustors would need to be repeatedly assembled, thermally cycled, disassembled, and stored, the design of the burner needs to be refined to meet the structural demands.

Fig. 43-Photograph of the engineering-scale burner during operation, burning Oriente crude oil.

Engineering-Scale Burner Component and System Performance

We were able to test successfully the engineering-scale burner a single time, since the plume heat transfer was so high that it melted the ignition plasma torches. In the process, we gathered some important data that revealed the burner performance.

Burner Performance

Figure 44 shows a photograph of the engineering-scale burner while in operation, with a nominal airflow of 6×10^{-2} kg/s, oil flow rate 8 L/min, and an ALR of 0.45. We should take note of some crucial details. First, there is significant unburned oil coating the inside of the third stage: this is really from the lack of flame inside the final stage, which we can attribute to the lower air and fuel flow rates. The lack of combustion in the final stage again suggests that the third stage is unnecessary. Simultaneously, the plume is burning inside the first and second stages, and the metal is discolored with heat. It is not clear how low the flame is anchoring, but it is clearly upstream of the second row of air holes, which is 300 mm from the atomizer exit. We should also note that there is little indication of residual soot in the exhaust, indicating nearly complete and clean combustion.

Fig. 44-Time-history plot of airflow, oil flow, and GLR of the engineering-scale burner test.
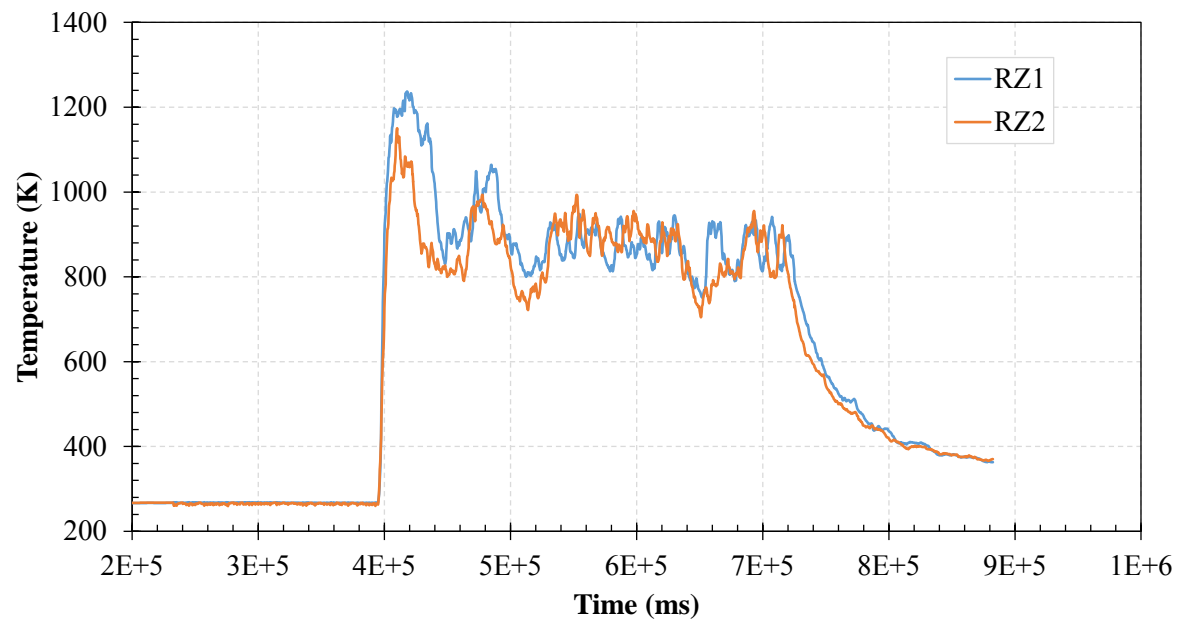
Fig. 45-Time-history plot of recirculation zone temperature. The RZ1 thermocouple resided at half-radius, adjacent to the plasma torch, 125 mm (5 in.) from the inlet bulkhead. The RZ2 thermocouple resided at half-radius, 90° from either plasma torch, 125 mm (5 in.) from the inlet bulkhead. See Fig. 11 for reference.

Figure 44 shows the time history of the test for the airflow, Oriente oil flow, and GLR of the test. The initial ignition attempt was not successful; we think the air flow velocity and sheer was too high to ignite and stabilize a flame. With this in mind, we reduced both the air and oil flow to 3×10^{-2} kg/s and 3 L/min, respectively, and the spray plume ignited and produced stable combustion. We then ramped both flow rates up. We were not able to ramp the air up to the full flow rate shown in Table 3; either the compressor was not able to provide the required flow and/or the pressure drop along the air feed hose was too great to provide the require metering pressure.

Once the flame was stable, we turned off the plasma torches, as we have in previous test burns. While in normal operation, the plasma torches cycle on and off to alternately provide a stream of hot plasma and cool the inner components. Once we turned off the plasma torches, they were exposed to the full heat flux of the burning plume, without any cooling. It was during this process that the plastic components inside the plasma torch heads melted.

Figure 45 shows the time history plot of the recirculation zone temperatures for the engineering-scale burner. During the initial ignition stage, the measured temperatures were greater than 1000 K. Though this temperature is undoubtedly biased from radiation, we should consider that the droplets emissivity is ~1, so the droplet were exposed to very high radiant heat flux. Once the plasma torches were turned off, at around 4.3×10^5 ms, the temperatures reduced to 800 – 1000 K. These are much greater temperatures than those measured for the sub-scale performance testing, shown in Table 6. We can attribute the higher temperatures to the larger plume, higher total heat release, and associated radiant heat transfer.
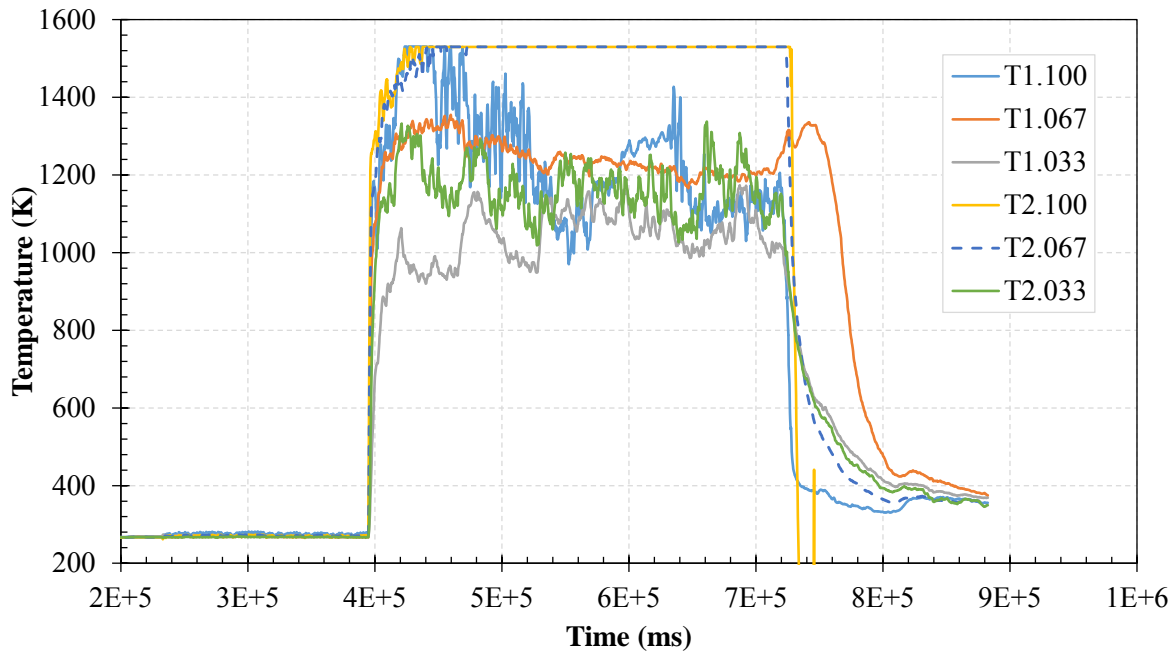
Fig. 46-Time-history plot of stage 1 thermocouples.

Figure 46 shows the time history plot of the stage 1 temperatures. The first thermocouple set, 1.#, denotes the temperature at the half-height of the first stage combustor. The second, 2.#, denotes the temperature at the first stage combustor full height. The second number specifies that the % the

thermocouple extended from the shroud wall to the duct centerline (e.g. #.100 is at the centerline). The highest recorded temperatures were at the full height, centerline and 67% from the wall (T2.100 and T2.067). The recorded temperatures were beyond the thermocouple limit of 1530 K, which was pre-set in the DAQ. This suggests that in these locations, the mixing and combustion was very rapid, efficient, and complete. This is especially promising, since high temperatures assure us that there is adequate heat release to vaporize and ignite the spray plume. We should note that during shut down, the combustion plume burned closer to stoichiometric and the higher temperatures damaged and destroyed the centerline (T2.100) thermocouple.

In the rest of the plume, the lowest temperatures were still at or above 900 K. These were near the walls (T1.033, T2.033) where cool air was being entrained and at the centerline, far upstream of the plume (T1.100) where the plume was still mixing. It is very promising that even with the larger atomizer and corresponding spray droplet sizes, the resulting heat is sufficient to vaporize and burn the spray.
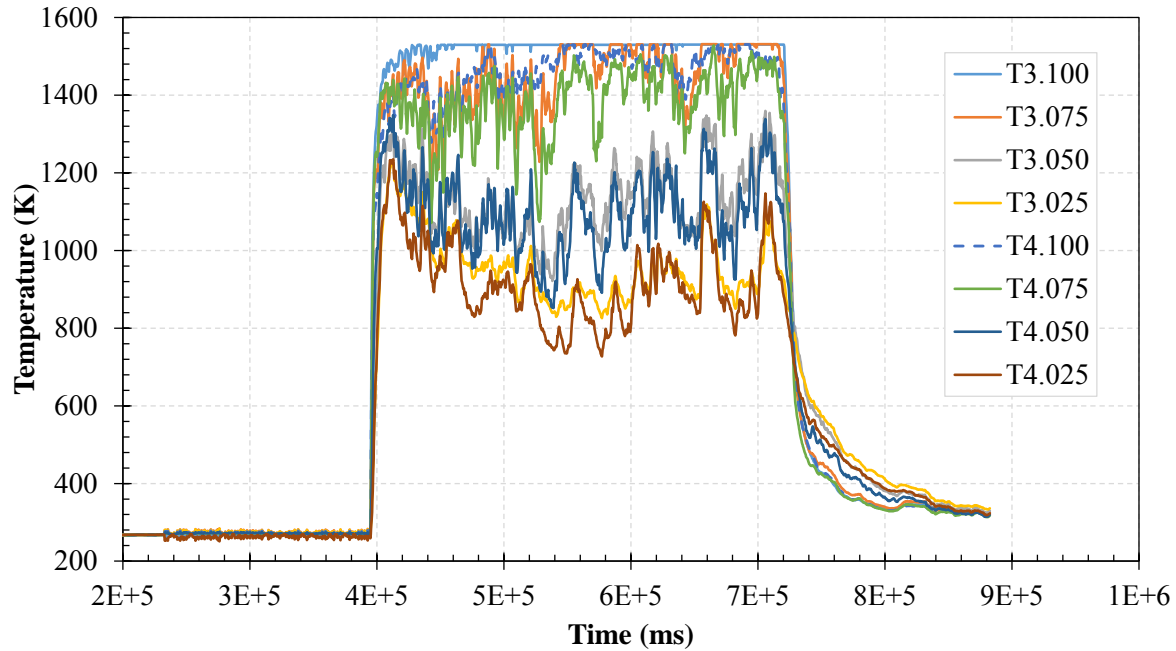
Fig. 47-Time-history plot of stage 2 thermocouples.

Figure 47 shows the time history of the stage 2 thermocouple measurements. Again, we observe similar maxima for the centerline thermocouples, with gradually decreasing temperatures with proximity to the shroud wall for both the half (T3) and full height (T4) thermouple arrays. In fact, for each radial location, there is substantial overlap in the plots at different heights. If we refer to the burner photograph, the flame appears largely uniform along the length of the second stage shroud (see Fig. 44). The higher centerline temperatures indicate that the plume has completely evaporated and combustion is progressing to completion.
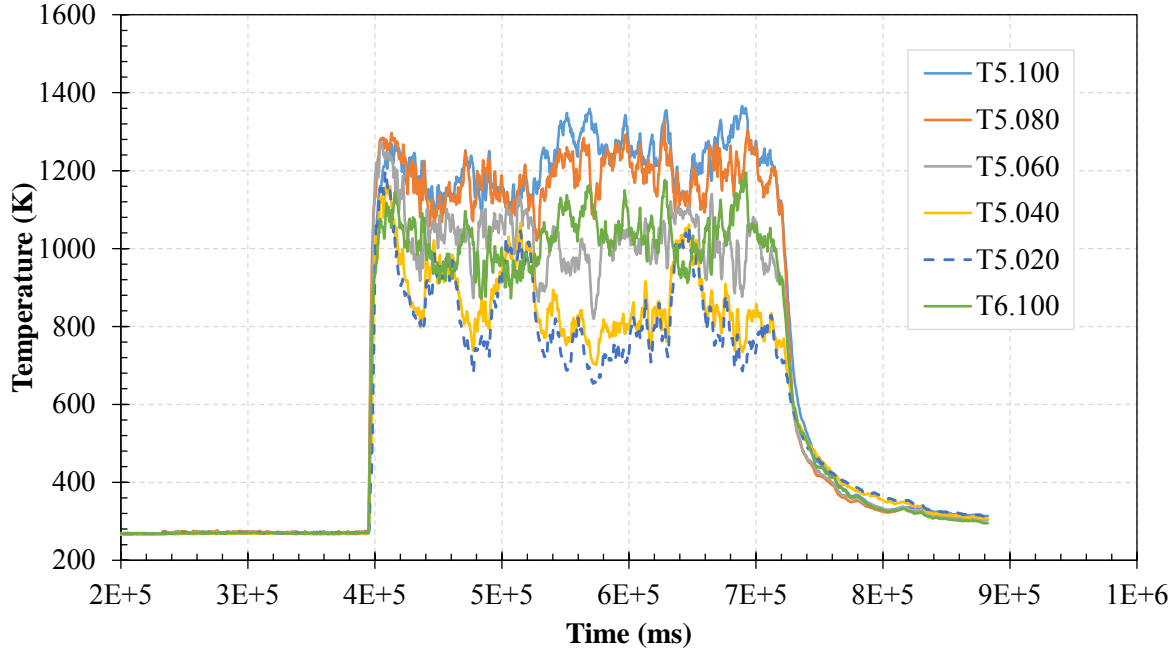
Fig. 48-Time-history plot of stage 3 thermocouples.

Figure 48 shows the temperature history of the final stage of the burner. At the combustor's half-height, the maximum temperatures are near the centerline and then cool progressively outward. The temperatures are in the range of 1200 K, indicating that the combustion has completed, heat release has ceased, and that the products are mixing with the surrounding air. By the combustor's exit, the temperature has dropped even further.

Summary

The first and final burn test for the engineering-scale burner successfully demonstrated that the atomizer and burner geometry could scale successfully to an even larger size and produce stable, complete combustion. The temperature profiles indicate stable, complete combustion that reacted within the length of the burner duct. The limited length of the burning plume, with respect to the burner length, was due to the limited flow capacity of the air compressor system. The very high measured temperatures indicate high radiative heat loading on all of the components. This high heat loading is the probable cause of the thermal failure of the plasma torches after the burner ignited and stabilized.

Prior to this effort, there was concern that the atomizer would not be able to operate at significantly larger dimensions than in previous studies [1,37-39]. We can attribute the atomizer performance to the increase in the nozzle Reynolds number:

$$Re_{noz,air} = \frac{\rho_{air} U_{air} D_{nozzle}}{\mu_{air}} \tag{4}$$

$$Re_{noz,oil} = \frac{\rho_{oil} U_{oilr} D_{nozzle}}{\mu_{oil}} \tag{5}$$

Where U is the superficial velocity, ρ is the density, and μ is the of the given fluid, air or oil. These values remained unchanged for the concept demonstration, laboratory, and development burners. The nozzle diameter, D_{nozzle}, changed between each geometry, but we observed very similar diameters between each measured case. As a result, the burner design was successfully scalable. The Reynolds number is a dimensionless ratio of the momentum to viscous forces for a particular flow system. For spray atomizers, the diameter-normalized droplet diameters typically decrease with increasing Reynolds number [40].

There are a number of design issues that need to be resolved. The primary issue with a larger burner is the greater heat transfer to the shroud: this caused the failure of the ignition plasma torches and presents a potential durability issue. The plasma torches used in this study produced intermittent hot plasma streams and were constructed of plastic, copper, and fiberglass. Clearly, a more durable, steady flow plasma torch needs to be constructed that can withstand the heat transfer from the burning plume while providing a steady hot plasma stream, so crucial to stabilize emulsified crude oils at or above 50% emulsion fractions. The optimization of the second stage combustor dilution area and the need for the third stage shroud still remain to resolved. Exhaust temperatures and, more importantly, emissions will determine the optimal shroud design.

Laboratory-Scale Experimental Results
We conducted a range of laboratory studies with the crude oil to understand how it behaved as it was emulsified with synthetic seawater, laboratory weathered, sprayed, ignited, and burned. These studies have revealed some basic physical and chemical behaviors and have given us insight into how the crude oil and emulsified crude oil burned in the combustor tests.

Table 7-Crude oil properties, including neat, weathered, and emulsified with synthetic seawater (SSW).

Crude Oil	Viscosity @ 25°C (cP)	Surface Tension (dyne/cm)	Measured API (°)	Measured Density @ 23°C (g/mL)	Assay API (°)	Assay Density @ 23°C (g/mL)	Refractive Index
Oriente	111.8 ± 1	27.92 ± 0.52	N/A	N/A	23.4	912	1.602 ± 0.01
ANS	10.40 ± 0.1	25.24 ± 0.33	33.0	859	29.7	876	1.502 ± 0.01
Weathered Oriente 72 hours	780 ± 10	30.56 ± 0.04	19.6	935	N/A	N/A	1.528 ± 0.01
Weathered ANS 72 hours	121 ± 10	30.41 ± 0.06	22.0	920	N/A	N/A	1.511 ± 0.01
Oriente w/ 25% SSW	335 ± 10	27.51 ± 0.01	19.0	939	N/A	N/A	1.471 ± 0.01
Oriente w/ 50% SSW	2039 ± 10	24.44 ± 0.09	18.0	945	N/A	N/A	1.468 ± 0.01
ANS w/ 25% SSW	16.06 ± 0.1	25.85 ± 0.2	19.0	939	N/A	N/A	1.502 ± 0.01
ANS w/ 50% SSW	17.25 ± 0.1	26.27 ± 0.1	19.0	939	N/A	N/A	1.497 ± 0.01

Table 7 shows the physical properties of the oils and mixtures we examined. Instead of discussing the property trends we observed, we will discuss them in the separate sections devoted to emulsification and weathering.

Basic Flame Behavior

The laboratory flame behavior changed widely with variations in co-flow fuel, fuel flow rates, and emulsification. Figure 49 shows spray flames anchored by a propane flat flame. We observed that the propane flat flame so effectively anchored the plume, that the flames would not lift except at very high plume velocities. This was not realistic, in comparison to the burner behavior, where the flame lifted and anchored within the first combustor stage. With a hydrogen flat flame, the stability mechanisms are more sensitive to the droplet diameters, evaporation behavior, fuel content, and heat transfer feedback mechanism that drive droplet evaporation. Pure crude oil, in general, will produce stable burning plume, though it may lift, as we will describe later in the Ignition Delay section. Emulsified crude oil, in contrast, will not consistently ignite and burn. For example, 25% emulsified mixtures, as shown in Fig. 50, will not always produce a stable, burning plume unless the droplet diameters are sufficiently small and the radiative heat transfer back to the plume is sufficient to evaporate enough hydrocarbons to enable combustion. In the cases shown in Fig. 50, the low velocity air produces slightly smaller droplets than the higher velocity air. Also, the radiative heat transfer from the higher oil flow rate case is much larger than that of the low oil flow rate, such that the droplets will evaporate into combustible fuel vapor more rapidly. The same poor flame stability was also observed with the emulsified ANS, which produced Sauter mean diameters similar to the 25% emulsified ORN at 2.9×10^{-4} kg/s of air, but produced a stable flame (Fig. 50b). In contrast, all of these conditions produced a stable burning flame in the sub-scale burner. This discrepancy suggests that radiative heat transfer plays a significant role in droplet evaporation and the release of flammable vapor.

(a)	(b)	(c)
Heptane	Oriente	Oriente detail
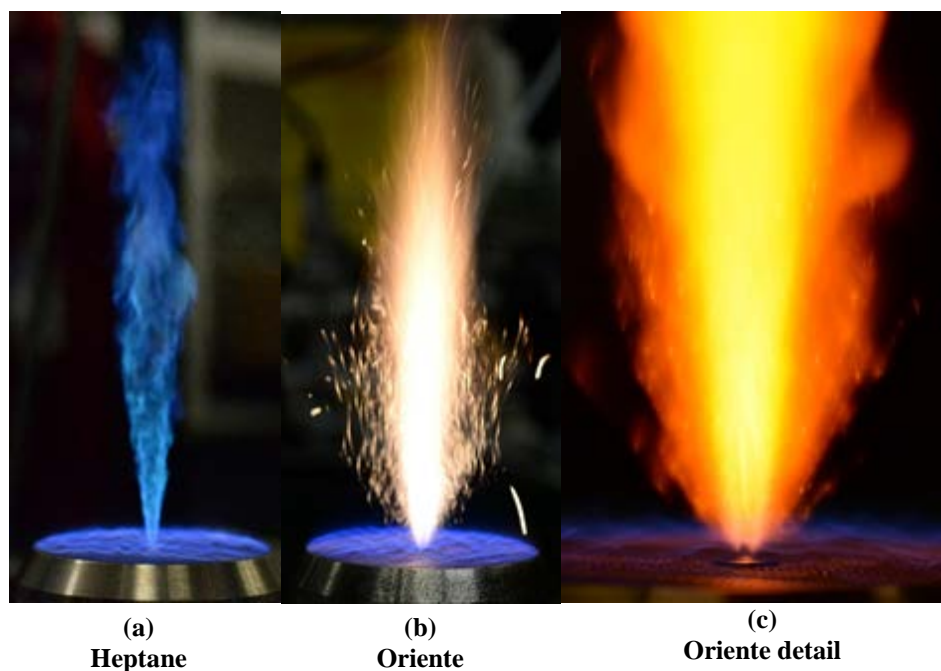
Fig. 49-Spray flames anchored by premixed propane-air flat flame, with $\phi = 069$ and an adiabatic flame temperature of 1860 K.

(a)
1.1x10⁻⁴ kg/s Air, ALR 0.5

(b)
2.9x10⁻⁴ kg/s Air, ALR 1.2
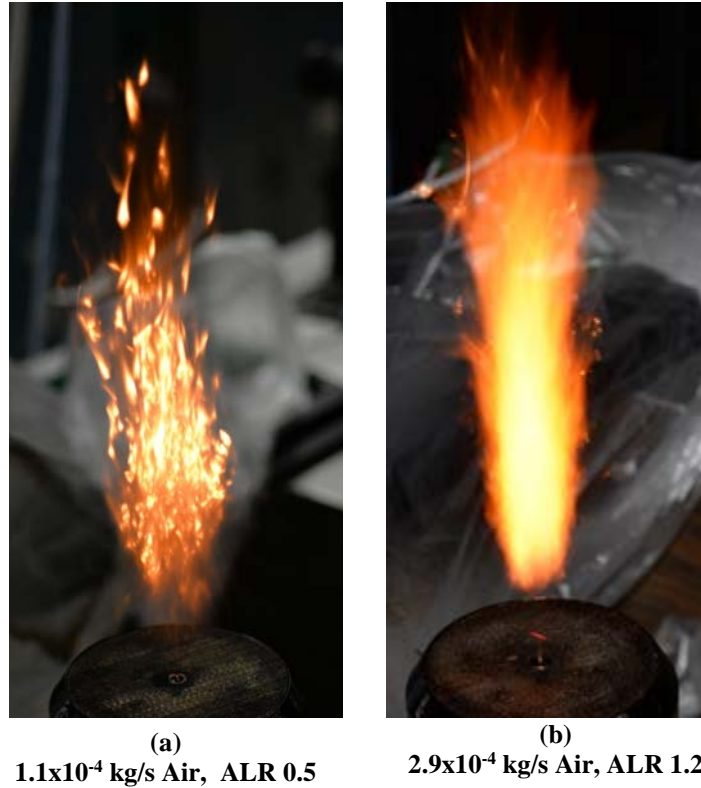
Fig. 50-Oriente, 25% emulsified crude oil spray flames anchored by premixed hydrogen-air flat flame, with $\phi = 0.30$ and an adiabatic flame temperature of 1190 K.

In the laboratory, we measured basic emissions for the 78% scaled full operation cases (see Table 3) using the NDIR gas-sampling rack.

Table 8-Measured emission gas concentrations from laboratory crude oil tests.

Oil	$\dot{m}_{Air}$ (kg/s)	$\dot{V}_{Oil}$ (mL/min)	CO_2 (%)	CO (ppm)	SO_2 (ppm)	O_2 (%)
ANS	2.9E-4	23.2	2.818	23.4	87	16.38

This provides a baseline, but the rack is currently being tuned and repaired in preparation for future engineering and full-scale testing.

Emulsification

Emulsifying the crude oil, prior to testing, allows us to examine the details of the associated spray combustion process. We found that for both the sub-scale and laboratory testing, emulsification is a crucial process. If we do not form a stable emulsion, then we do not have enough time to load and burn the emulsion before it separates. We have also observed that a stable emulsion is required for stable combustion.

Table 9-Emulsification mixture constituents and volumes for 500 mL.

Seawater		Crude Oil	Surfactant		60% Span® 85	40% Tween® 85
50%	250 mL	245 mL	1%	5.0 mL	3.0 mL	2.0 mL
50%	250 mL	245 mL	2%	10.0 mL	6.0 mL	4.0 mL
50%	250 mL	245 mL	3%	15.0 mL	9.0 mL	6.0 mL

During initial studies, we blended both the Oriente and the ANS crude oil with 50% synthetic seawater[41] and surfactant amounts shown in Table 9, with a high-speed laboratory blender, corresponding to the work done by Ocampo-Barrera *et al.*[30]. We observed that the Oriente oil with a 1% surfactant fraction remained emulsified for 24 hours, while the ANS separated immediately. We found that the high-speed blender worked best when used for 10-20 seconds. For longer periods, we observed that the mixing heated the fluid, through viscous dissipation, which increased the separation rate.

For the ANS, we continued to vary the mixing times and increased the surfactant concentration to 3%. We discovered that with a surfactant concentration of 3%, the ANS remained emulsified for about one hour. We discussed this problem with BSEE's Timothy Steffek and he reported that ANS will not normally emulsify in any practical manner. It will disperse, as has been observed by Belore *et al.* [42], but emulsification is more difficult.

Using a different, lower speed mixer, a Dispersator with a Duplex head, we tested and compared Corexit® 9500 and Span® 85. Both mixtures contained 25% synthetic seawater in Oriente crude oil. We mixed both emulsions with the motor at 25 VAC (120 VAC maximum) for 5 minutes. We observed that the Corexit® started to separate after an hour and forty minutes while the Span® 85 mixture did not start to separate until after two hours. In a separate study with the motor at 35 VAC, we observed that the Corexit® and Span® 85 mixtures remained emulsified for much longer. After three hours, neither mixture had separated. Overnight and sixteen hours later, the Corexit® mixture was found to have separated while the Span® 85 mixture remained unchanged. As a result, it appears that Span® 85 is a much better emulsifying agent and that increasing the sheer energy during the mixing process directly affects the emulsification and the length of time the crude oil and synthetic sea water remain mixed.

We can draw a number of conclusions from the literature, our emulsification efforts, and those of the investigators at Worcester Polytechnic Institute (WPI). First, freshwater and seawater emulsify differently than one another. The disparity between emulsification findings of WPI and NRL clearly assert this conclusion. Second, dispersion and emulsification are distinct process and surfactants mixtures and blends operate differently in mixtures. Third, the amount of shear strain on the fluid is a relevant parameter in the mixing process.

Corexit® is designed to behave as a dispersing agent, which is a distinct process different than simple emulsification. Dispersion is the process by which micelles, small droplets of crude oil surrounded by a monolayer of surfactant molecules, will mix into the seawater. Surfactants are molecules with polar (oleophobic, hydrophilic) heads at one end and non-polar (oleophilic) groups at the other. The design intent for a dispersant is that ocean surface shear, from wind or waves, form a droplet that is small enough that buoyant forces are much less than convective drag, allowing the local turbulence to convect the droplet into the water column and away from the oil slick at the water's surface [43,44].

Table 10-Corexit 9500 chemical constituents.

CAS #	Name	Common Day-to-Day Use Examples	Commercial Name	Action
1338-43-8	Sorbitan, mono-(9Z)-9-octadecenoate	Skin cream, body shampoo, emulsifier in juice	Span® 80	Non-Ionic surfactant
9005-65-6	Sorbitan, mono-(9Z)-9-octadecenoate, poly(oxy-1,2-ethanediyl) derivs.	Baby bath, mouth wash, face lotion, emulsifier in food	Tween® 80	Non-Ionic surfactant
9005-70-3	Sorbitan, tri-(9Z)-9-octadecenoate, poly(oxy-1,2-ethanediyl) derivs	Body/Face lotion, tanning lotions	Tween® 85	Non-Ionic surfactant
577-11-7	* Butanedioic acid, 2-sulfo-, 1,4-bis(2-ethylhexyl) ester, sodium salt (1:1)	Wetting agent in cosmetic products, gelatin, beverages	Docusate sodium	Ionic surfactant
29911-28-2	Propanol, 1-(2-butoxy-1-methylethoxy)	Household cleaning products	Di(propylene glycol) butyl ether, mixture of isomers	Non-ionic surfactant
64742-47-8	Distillates (petroleum), hydrotreated light	Air freshener, cleaner	TraceSELECT® ICP solvent (A reference Kerosene)	Hydrocarbon diluent
111-76-2	** Ethanol, 2-butoxy	Cleaners	Ethylene glycol butyl ether	Non-ionic surfactant

Nalco, the manufacturer of Corexit®, posts the constituent chemicals of Corexit® 9500 online at http://www.nalcoesllc.com/nes/1602.htm, per request of the EPA, as shown in Table 10. There are three classifications of chemicals in Corexit® 9500. The first is a non-ionic surfactant that forms a monolayer between the crude oil and the seawater. The second class is an ionic surfactant that has an ionic group that loses an ion (e.g., sodium) in water to leave an empty, polar branch that is highly oleophobic or hydrophilic. The third class is a hydrocarbon solvent that dissolves the crude oil to promote mixing between the crude oil, surfactants, and seawater.

In contrast to oil dispersion, in an emulsion, the oil/water droplets are in constant contact with one another so the surfactant must be resistant to breaking their monolayer interface while in contact with oil. This difference between a dispersion and an emulsion suggests why Span® 85 and Tween® 85 have successfully emulsified crude oil while Corexit® 9500 could not. Span® 85, or sorbitane trioleate, contains a sorbitane molecule attached to three oleates, one of which has a hydroxyl group (OH) that forms a fatty acid. The OH of the fatty acid and an O in the sorbitane ring are capable of forming hydrogen bonds with other sorbitane molecules. Tween® 85, or polyoxyethylenesorbitan trioleate has a similar structure, but with two additional oxyethylenes attached to the sorbitane ring, each with additional OH groups that have local polar charges and can also form hydrogen bonds with oxygen. Sorbitane has a polar charge, water's polarity attracts it. Simultaneously, the water constantly repels the trioleate group. The exact opposite process occurs as the sorbitane trioleate interacts with the non-polar hydrocarbons. These attractive and repulsive forces allow the formation of stable, persistent micelles that will mix amongst both crude oil and

seawater. The apparent difference in emulsion stability between the sorbitane trioleate and the blend within Corexit® is that the presence of the hydrocarbon diluent and the monooleate surfactants diminish the emulsifying effects, in comparison to the trioleats.

We should also consider the amount of shear strain imposed on the fluid during the mixing process and the fluid volume. The high-speed blender, paint mixer, drill press, and Dispersator Duplex mixer all exhibited a range of shear strains on the mixing process. The high-speed blender exerted enough shear to form a stable emulsion, but given enough mixing time, the shear work heated the mixture enough to accelerate the separation process. The hand drill-driven paint mixer, in contrast, could not impose enough shear energy into a large volume of oil-seawater to form an emulsion reliably. The drill press at 250 rpm had the same problem, though at 500 rpm, the drill press was successful for 25% emulsions but could not form long-lasting emulsions for 50% seawater mixtures. The Dispersator was able to impose consistent, high-shear mixing and was able to form a long lasting emulsion with the right surfactant.

From these different findings, we can conclude that a combination of Span® 85 and Tween® 85 surfactants and some sort of high shear mixer will form the most stable emulsion. We will still need to determine the amount of surfactant, mixing duration, and shear necessary for a given combination of seawater and crude oil. For some mixtures, we have determined the best combinations, shown in Table 11. There remains a number of emulsions that we have yet to mix and test.

Table 11-Known mixing and surfactant combinations that will produce emulsions lasting an hour or more.

Seawater Fraction	Oil	Mixing	Mixing Duration	Surfactant	Surfactant Fraction	Emulsion Lifetime
25%	Oriente	Dispersator at 35 VAC	5 minutes	Span® 85	1%	24+ hr
50%	Oriente	Blender	10 s	60%Span®85, 40% Tween®85	1%	24 hr
50%	ANS	Blender	10 s	60%Span®85, 40% Tween®85	3%	1 hr
25%	Oriente	Drill press, 500 rpm	2 hr	Corexit®	2%	2 hr

If we refer back to Table 7, there are some general trends in properties that emulsification produces. In general, emulsification increases the viscosity and density while it decreases surface tension and refractive index. These changes can be understood in terms of the microscale behavior: emulsification adds additional interfaces into the fluid between oleophobic and oleophillic fluids (water and oil, respectively) with large surfactant molecules at the interface. These interfaces increase the viscosity of the overall mixture by adding shear resistance. The increased density is due to the greater concentration of synthetic seawater, which has a higher density than either crude oil in our study. The increasing concentration of surfactants with emulsification decreases the surface tension, which allows the emulsion to persist. It also decreases the index of refraction, which is lower for synthetic seawater.

It is worth noting how inorganic salts influence combustion processes. There are a number of engineering studies describing how adding salts, such as NaCl, increases the effectiveness of fire suppression sprays [45-50]. Williams *et al.* [51] , while formerly part of this research group, examined the underlying chemical kinetics of this behavior, based on the work of a number of fundamental studies [52-57] describing the chemical reactions of alkali metals and combustion species. Williams *et al.* [51] predicted that alkali significantly decreased both flame temperature and flame speed, which will appreciably increase

ignition delay, decrease flame stability, and decrease burner stability. This implies that seawater will noticeably inhibit combustion as the emulsion fraction increases.

Laboratory Weathering

ANS and Oriente were aerated with nitrogen separately in an 8 L container for 72 hours. Due to its chemical composition, time can greatly alter the physical properties of a crude oil. Lighter hydrocarbons can evaporate over time altering the mass, density, viscosity, and surface tension of the crude oil. Knowing these physical properties is crucial to understanding droplet dynamics which are heavily driven by a liquids viscosity and surface tension. The mass of the crude oil was monitored over the 72 hours and is shown in Fig. 42 below from ANS and Oriente.
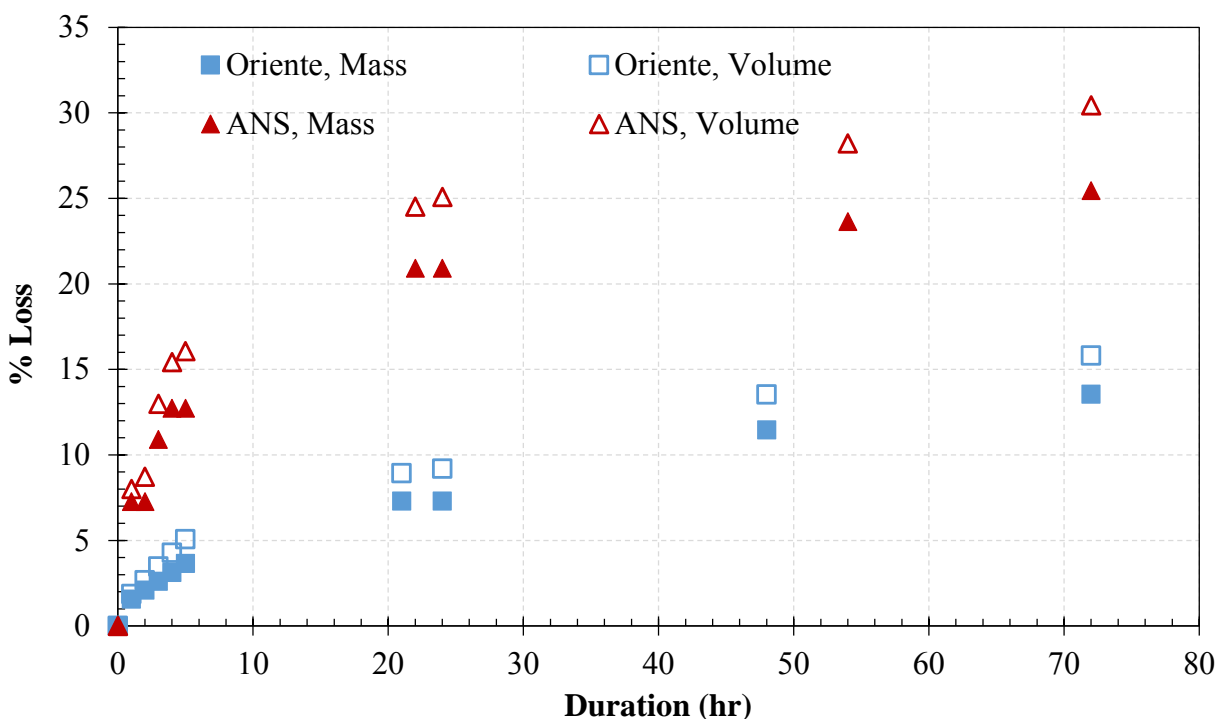
Fig. 51-Percent mass and volume losses for Oriente and ANS with duration of laboratory weathering.

Figure 51 shows the difference in mass loss between ANS and Oriente as it was aerated with nitrogen. Over a 72 hour period, Oriente lost roughly 14% of its mass while ANS lost 25%. The volume loss for each crude oil is also shown with Oriente losing 16% by volume and ANS losing 30% by volume. The differences between mass loss and volume loss directly relate to the differences in density between Oriente and ANS. Oriente has a higher density while ANS has a lower density, small changes in mass have a smaller effect on Oriente compared to ANS.

Over a 72 hour period, neither crude oil had reached a steady state mass loss. At the beginning of testing, we had assumed weathering would occur between 40-60% in a matter of hours and we would compare the two crude oils at varying percentages of mass loss. However, early attempts at weathering Oriente showed a much smaller mass loss than anticipated over a much longer time frame. After examining Oriente, it was decided to compare the oils based on time weathered instead of percent mass loss. Therefore,

59

both crude oils were examined up to 72 hours, then compared for changes in physical properties and burn behavior.

Comparing the viscosities of the pure and weathered crude oils showed an increase in viscosity by a factor of 7 for Oriente and by a factor of 12 for ANS. The refractive index also appeared to decrease for weathered Oriente, but remained the same for weathered ANS compared to the pure counterparts. The emulsifications with the weathered Oriente also decreased in refractive index as seawater was added which was expected as the refractive index of seawater (clear) is much lower than that of crude oil (opaque).

Interesting comparisons arose when examining surface tension and density. Weathered Oriente and ANS had higher surface tensions than those of pure crude oil. Because of the varying composition of crude oil, hydrocarbons exist in short and long chains with short chains having lower vapor pressures, but also lower surface tensions. As they evaporate out of the crude due to weathering, long chain hydrocarbons, with larger surface tensions, are still present, increasing the overall surface tension. The loss of short chained hydrocarbons also explain the changes in density seen between weathered and pure crude oils with weathered oils having a higher density than pure crude oil for both Oriente and ANS. Along with lower vapor pressures and lower surface tensions, short chain hydrocarbons are less dense. As they are evaporated from a solution, the longer chained hydrocarbons are more concentration and contribute more to the average density. Mass spectroscopic measurements of the weathered samples compared to the pure samples confirm the decrease in short chained hydrocarbons through weathering and will be presented later in this report.

Non-intuitively, the emulsions of seawater and crude oil produce lower surface tensions than those of pure crude oil. Water has a surface tension of 72 mN/m at 23°C. A guess at the surface tension of the mixture would have been between 30 and 72 mN/m. However, the presence of surfactants in the emulsifications may be effecting the surface tension. Surfactants allow oil and water to mix by lowering the surface tension of water which is normally so large (72 mN/m) that oils cannot overcome the barrier to mix. Solutions of surfactants and water can alter the surface tension of water from 72 to 20 mN/m. The presence of the surfactant may be altering the emulsion in this way. Although the droplet size through the FBA is dependent on viscosity and surface tension, details later in this report show that changes in surface tension have little effect on droplet size through the FBA.

Ignition Delay

The flame anchor height is a simple measurement of the ignition delay. Mathematically, the ignition delay time scale can be expressed as:

$$\tau_{ign} = \int_0^h \frac{1}{V(y)} dy \tag{6}$$

Where V is the vertical velocity of the plume and y is the vertical coordinate. In this case, the ignition time scale includes the droplet evaporation, mixing, and chemical kinetic timescales. In this geometry, we cannot measure the velocity so close to the nozzle with phase Doppler anemometry because the droplets are not completely spherical nor and it cannot be measured using particle image velocimetry because the droplet scatter will dominate any other added particle. Therefore, the comparative flame anchor height will provide us with an understanding of the behavior.
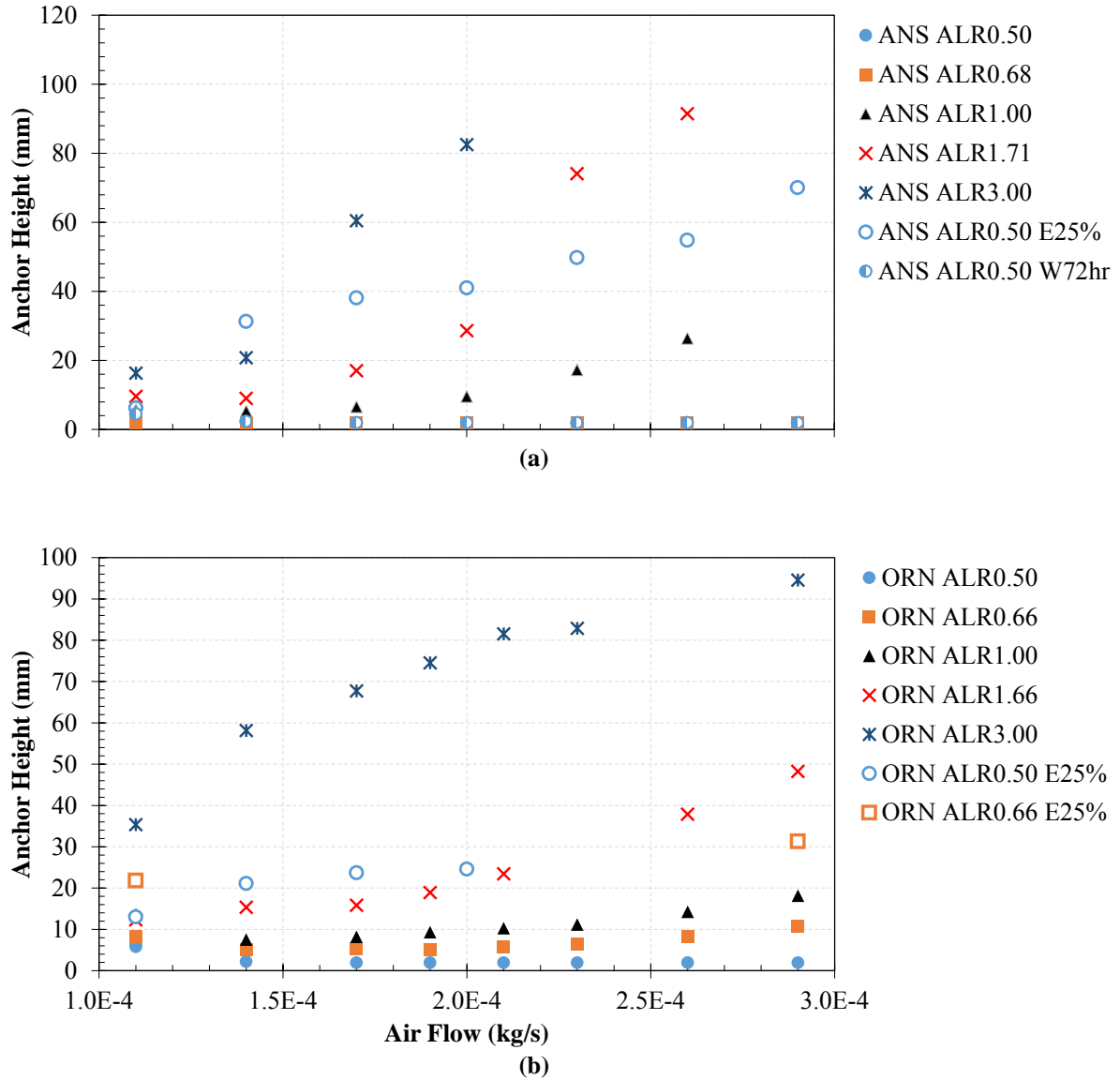
Fig. 52-Flame lift off heights for (a) ANS (a) and (b) Oriente as a function of air flow rate and ALR. Plots include data for emulsified and weathered oil.

If we look at the flame anchor heights in Fig. 52, we notice that generally, the anchor height increases with ALR and airflow. Low ALR, or more fuel flow, corresponds to more available fuel vapor at the base of the flame, allowing more robust ignition. Increasing the air flow increases the velocity of the flow, which increases the aerodynamic strain rate on the flame at a given location. If the flame strain is above the extinction strain rate at a particular location, the flame will extinguish instead of burn [29]. Thus, increasing the airflow, even if the ALR is constant, increases the strain toward or past extinction, lifting the flame anchoring region. Additional air flow not only increases the aerodynamic flame strain, but it also increases mixing between the fuel plume and the outside air, which effectively lowers the fuel concentrations.

The data in Fig. 52 present some counterintuitive results from assumptions we might make based on oil behavior. We could assume that the flame anchor height increases with increasing crude oil weight; the

heavier weight molecules in the heavier crude oil have higher boiling temperatures, which we would expect to delay evaporation ignition, comparatively. Furthermore, the heavier oil is more viscous, which will produce larger droplets with longer evaporation time scales. If we compare the flame lifting heights from Oriente, we see that they are clearly smaller for ALR of 3.00, 1.66/1.77, and 1.00. If we examine the corresponding droplet behavior in the Phase Doppler Anemometry, Crude Oil Measurements sections, we see that the droplet diameters are indeed larger for all of the Oriente mixtures. Clearly, oil temperature and droplet diameter are not players in the flame height comparison. Though larger droplets evaporate more slowly, the laboratory-weathered crude will have more asphaltenes, and thus a greater radiative heat absorption cross section. Thus, the shorter ignition delay may be due to the greater asphaltene concentration. As discussed in the introduction, Bartle *et al.* [15] reported that increasing asphaltene content reduces ignition delay by emitting lighter-weight, more reactive alkanes during devolatilization, which occurs when the large asphaltene molecules are heated and start to break apart into smaller molecules.

There is also a noticeable aberration from the general trend of increasing flame anchor height with air flow at the lowest air flow rate. We observed this for all but a few cases. We suspected that this was caused by larger droplet diameters at the lowest air flow rate.

In the process of the flame anchor studies, we observed that the visible flame radiation appeared to be proportional to the fuel flow rate. To confirm this, we measured the flame radiation using a radiative heat flux sensor, or Gardon gage, as shown in Fig. 53. These gages are water cooled and have a guard air flow across the face of the sensor windows. Infrared radiation from the flame travels through the sapphire windows and is absorbed at the center of a thin foil sensor that is cooled at its periphery. The temperature difference between the center and edge of the foil, measured by thermocouple junctions, is used to measure the radiative heat transfer.

(a)
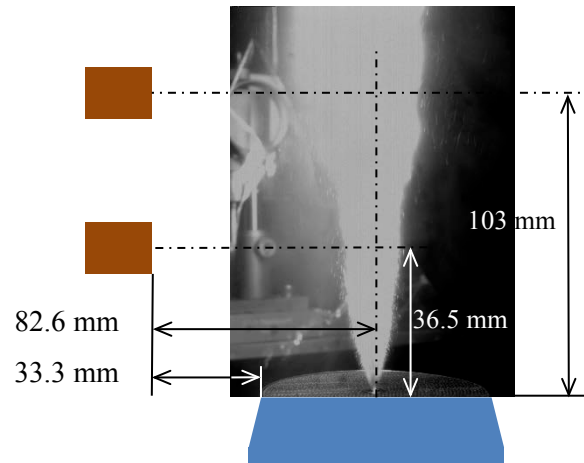
(b)

Fig. 53-Flame radiative heat transfer sensor arrangement and dimensions.

We gathered measurements with the ANS crude oil and plotted the results for the two sensors in Figures 53 through 55. We also gathered limited radiative heat flux measurements with the more viscous Oriente, but the side splatter from the atomizer obscured the windows of the heat flux gages, making the measurements unreliable. From Figures 54a and 55, we observe that for a fixed value of ALR, there is little difference in radiative heat transfer until the increasing air flow lifts the flame anchor height. At lower air flows, there is a gradual decrease, but not as significant as that caused by decreasing the ALR. If we consider the influence of the oil flow rate, with constant air flow, we see that the radiative heat flux is almost linearly related to the oil flow rate.
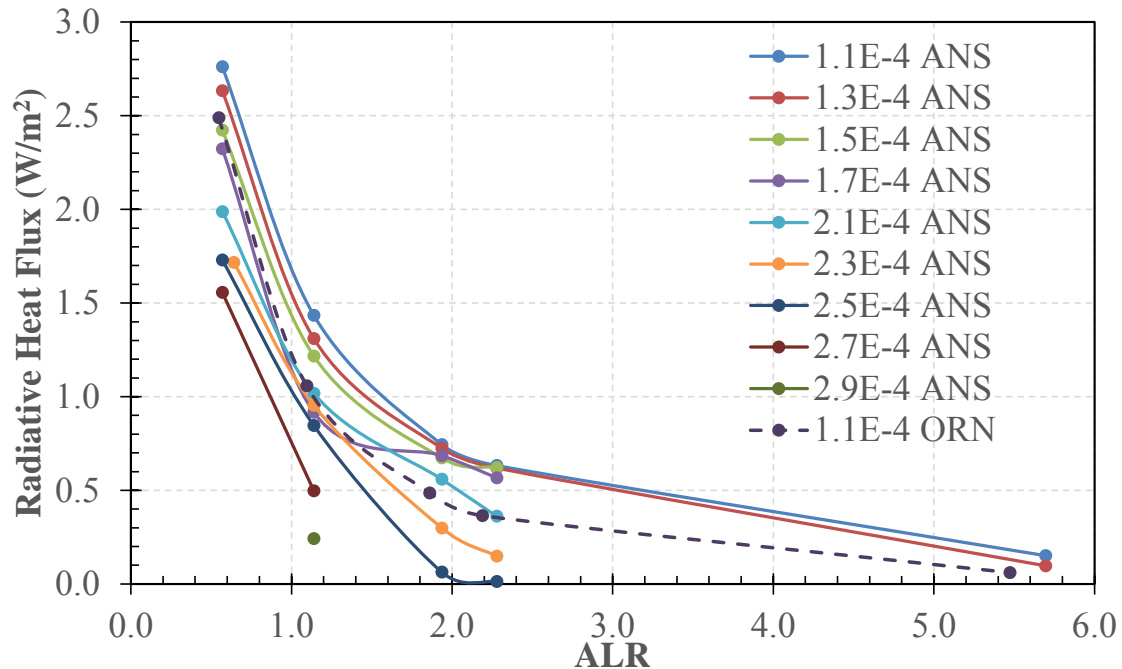
(a)
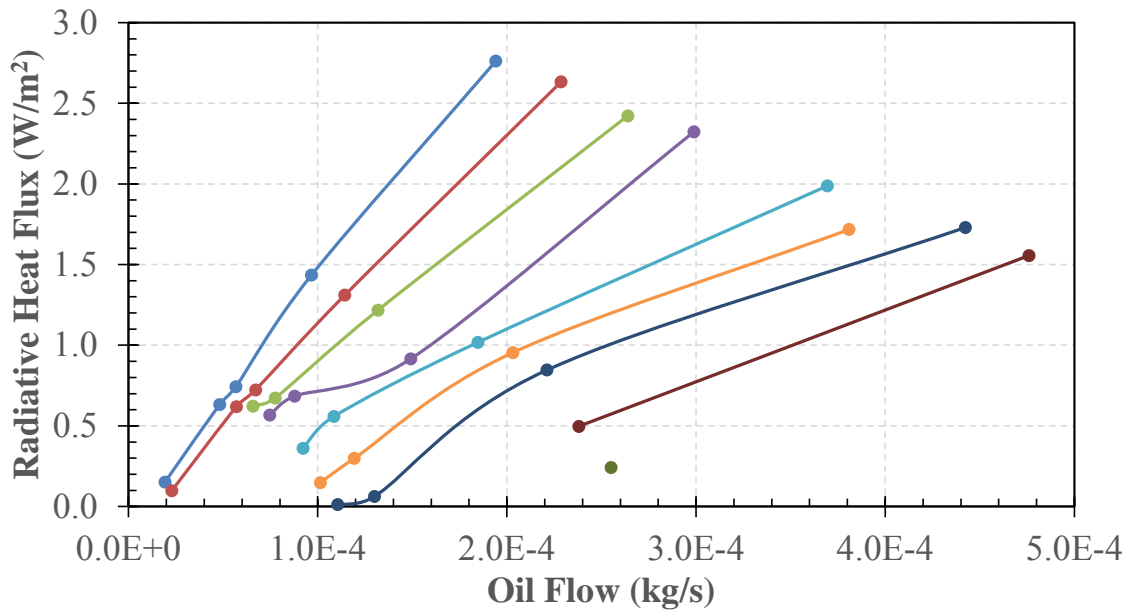
(b)

Fig. 54-Radiative heat transfer from the lower heat flux gauge, plotted against (a) ALR and (b) oil flow rate, for different air flow rates.

If we apply the flame anchoring and radiative heat transfer observations to the operation of the actual burner, we can make some critical operability conclusions. First, we can conclude that reliable ignition will best be performed at low ALR: the flame will lift less with more available fuel vapor and the radiative heat transfer from the burning plume will heat the burner shroud more, which then aids in flame stability as the

oil and air flow are increased. Second, there is an airflow, even for a modest ALR, beyond which the flame will lift and potentially become unstable, if there is insufficient recirculation of hot products upstream and heat transfer from the burner shroud to the entrained air.
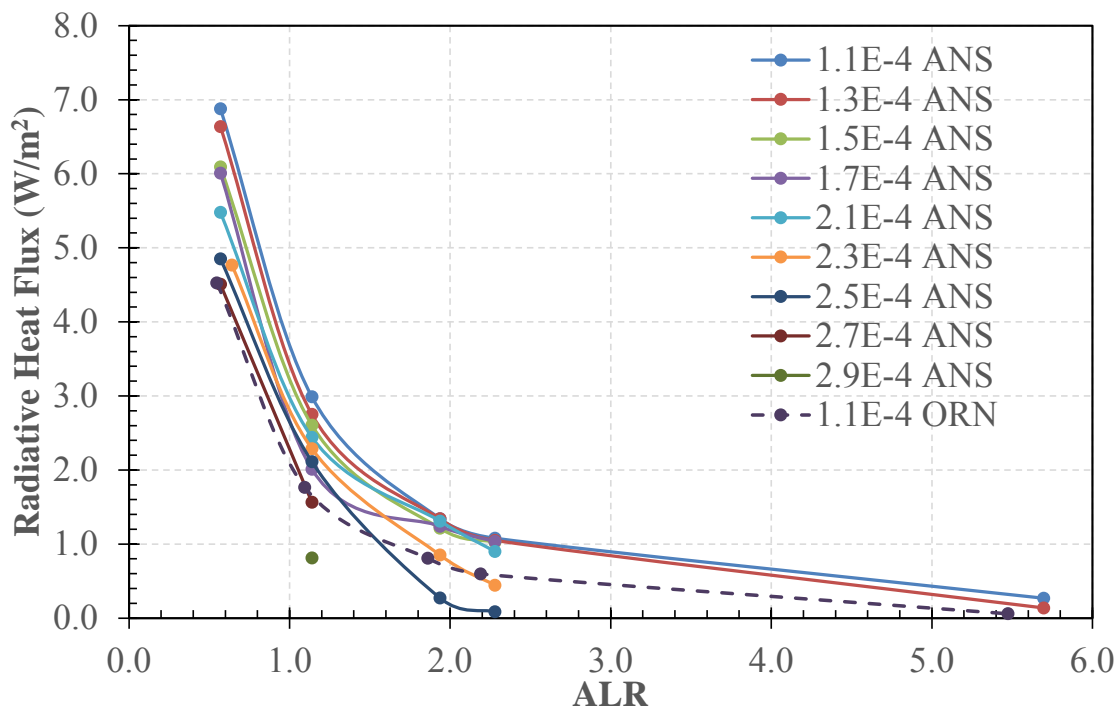
Fig. 55-Radiative heat transfer from the upper heat flux gauge, plotted against ALR.

The radiative heat flux from the upper heat flux gauge was very similar to that of the lower heat flux gauge, except that it was 2-3x greater. Surprisingly, the order from least to greatest was also nearly the same. We should note that the highest radiative heat fluxes correspond with the lowest anchoring flames. This is unsurprising since radiative heat flux is the only mechanism available for heat transfer upstream: there is not convective recirculation as in the actual burner.

To determine if emulsified flames, which had greater difficulty burning in the lab, could be ignited with additional heat transfer, we placed a propane torch in the stream of the poorly burning spray plume, as shown in Fig. 56. Clearly, the influence of heat transfer has greater influence than the combustibility of the spray mixture. Once there is sufficient heat release and associated upstream radiative and downstream convective heat transfer, the plume will ignite and propagate in a stable manner.

<div align="center">(a)   (b)</div>
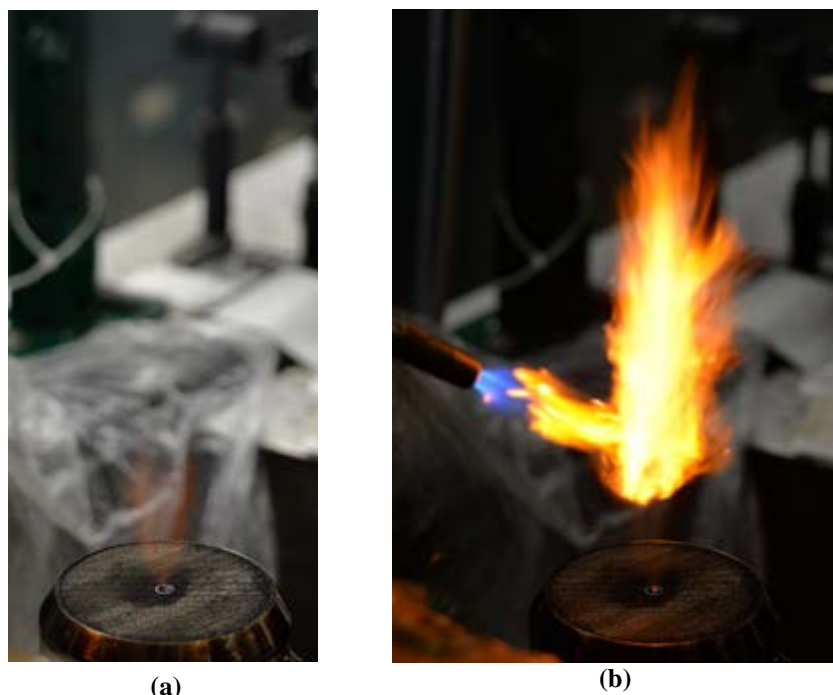
Fig. 56-Spray flame of ANS, 10.9 mL/min 25% synthetic seawater emusion, 1.1×10^{-4} kg/s air with (a) hydrogen-air flame and (b) propane torch and hydrogen-air flame.

Phase Doppler Anemometry

We conducted two droplet measurement investigations. The fundamental measurement investigation focused on how the droplet diameters and velocities, produced by the FBA, changed as liquid physical properties alone varied, without combustion. The crude oil investigation measured the combusting spray behavior of the Oriente and Alaska North Slope oils in neat, emulsified, and/or weathered states. This allowed us to compare the droplet and combustion behavior of different oil mixtures.

Fundamental Measurements

In a parallel effort that used the same laboratory platform as other aspects of this study, we examined how viscosity and surface tension influenced the atomization behavior. We have performed a number of detailed studies of droplet behavior. All of our measurements were performed with a mass-based, Air-Liquid Ratio (ALR) of 3, with nearly the same liquid and air flow rates, since each of the fluids have nearly the same density. We initially used water as a baseline fluid, as we did in the concept demonstration study [1]. We then used mixtures of water and additives to alter the fluid properties of interest.

Table 12- Properties of fluids used in fundamental FBA experiments. All quantities were measured at the indicated temperatures.

	Temp. (°C)	Density (g/cm³)	Refr. index[a]	Surf. tens.[b,c] (mN/m)	Viscosity[b,d] (cP)[e]
Water	22	1.00	1.334	71.4 ± 0.5	1.13 ± 0.001
99.9/0.1[f] Water/Forafac	23	1.00	1.334	15.6 ± 0.1	1.22 ± 0.01
50/50[g] Water/Glycerol	23	1.14	1.399	55.3 ± 2.0	8.4 ± 0.6
Glycerol	25	1.25	1.472	62.8 ± 0.3	838 ± 9

(a)
Profiles of the Sauter mean diameter (D_{32}) as a function of radius and height.

(b)
Profiles of the droplet number density as a function of radius and height.
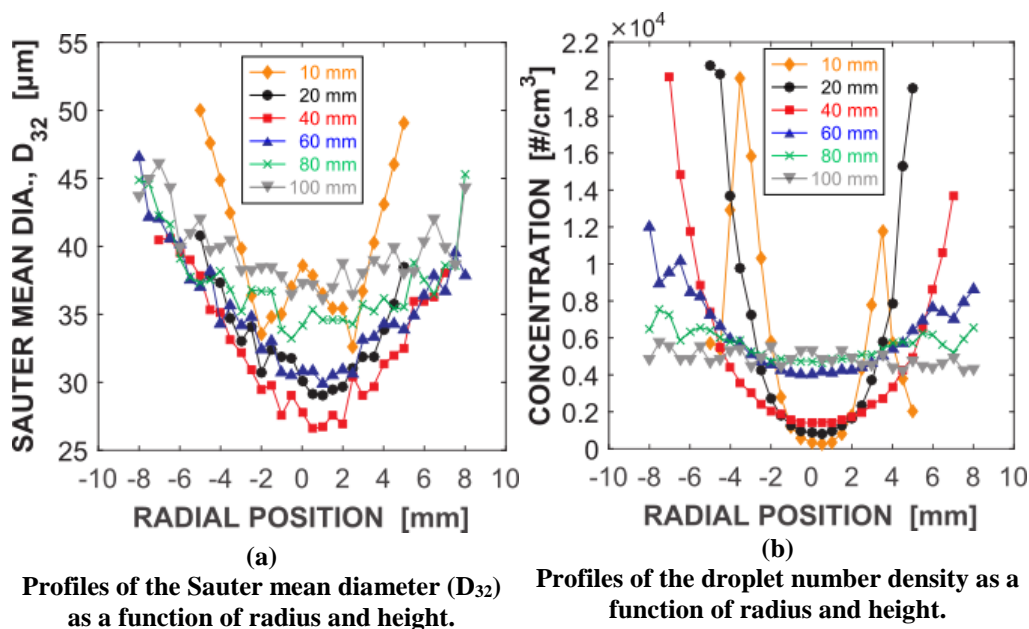
Fig. 57-Radial profiles of measured (a) water droplet diameters (D_{32}) and (b) density at several heights above the atomizer exit [58].

Table 12 shows the various additives, the mixtures, and their respective properties. Forafac® 1157N is a perfluorinated surfactant designed to lower the surface tension of aqueous solutions, such as firefighting foams. We altered the viscosity using glycerol, which is used widely in the food and pharmaceutical industries and is a byproduct of the transesterification process used to create biodiesel fuels from raw fatty acids. Glycerol itself has been investigated as a combustion fuel, and because it has extremely high viscosity, much like many heavier crude oils, we also characterized its spray behavior in this study.

We first examined the spray behavior of water, as shown in Fig. 57. The profile plots of the Sauter mean diameter (D_{32}) in Fig. 57a show that the spray plume changed with height, or distance downstream. For all radii, the larger droplet diameters were located closer to the atomizer (10 mm) and then rapidly decreased until a height of 40 mm above the atomizer, indicating that the jet was still breaking apart and the droplets were still forming. Above 40 mm, the D_{32} increased as droplets collided and coalesced. If we examine the concentration profiles in Fig. 57b, we see that the plume formed a nearly hollow cone between 10 mm and 40 mm above the atomizer, surrounded by the bulk of the spray droplets. Above 40 mm,

turbulent mixing merges the annular droplet flow into a solid plume, with almost radially uniform droplet concentrations and only moderate droplet size variation.

(a)
Profiles of D_{32} as a function of radius and at two heights for the three lowest viscosity fluids

(b)
Profiles of D_{32} as a function of radius and at two heights for water and glycerol, which have the greatest difference in viscosity.
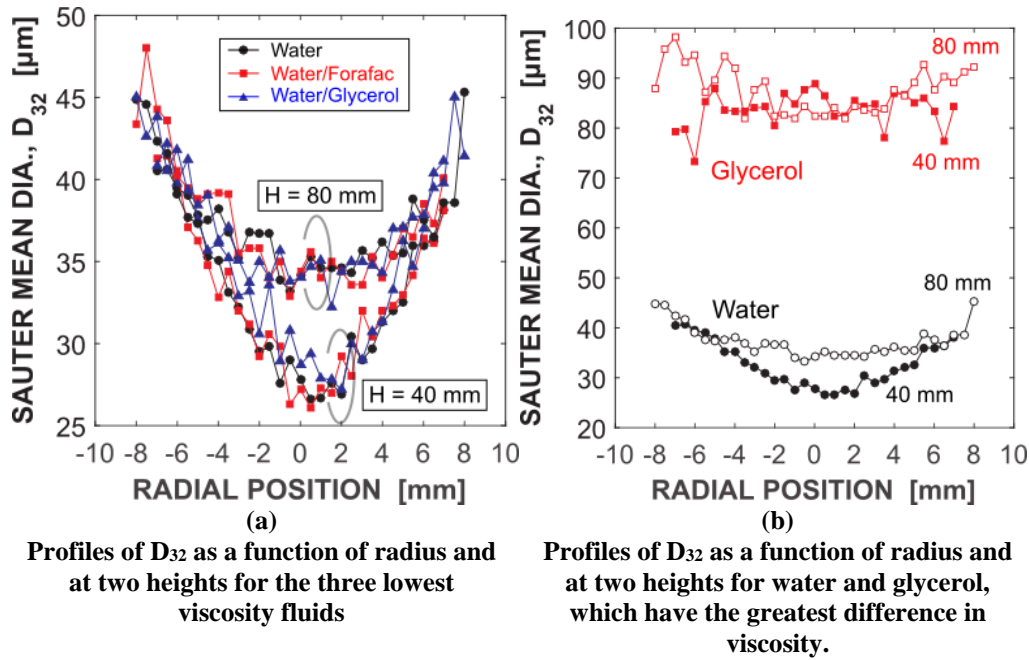
Fig. 58-Radial profiles of D32 showing the influence of viscosity [58].

Figure 58 highlights the difference in the spray behavior as influenced by the viscosity and surface tension alone. Fig. 58a shows the influence of a 4.5x reduction in surface tension and a 7x increase in viscosity. The corresponding profiles in Fig. 58a show nearly identical profiles, given the scatter in the plots. This demonstrates that for small changes in viscosity and surface tension, there was negligible difference in the spray droplet diameters. If we recall the droplet profile measurements from the concept demonstration phase of this program, the ALR had a much greater influence on the droplet diameter. Fig. 58b reveals that a 750x increase in viscosity changed the droplet diameter approximately 3x, indicating that viscosity had only a moderate influence.

(a)	**(b)**
Probability distributions of droplet diameter at two heights on the centerline for water and glycerol.	**Spherical validation profiles for water, water/glycerol, and glycerol.**
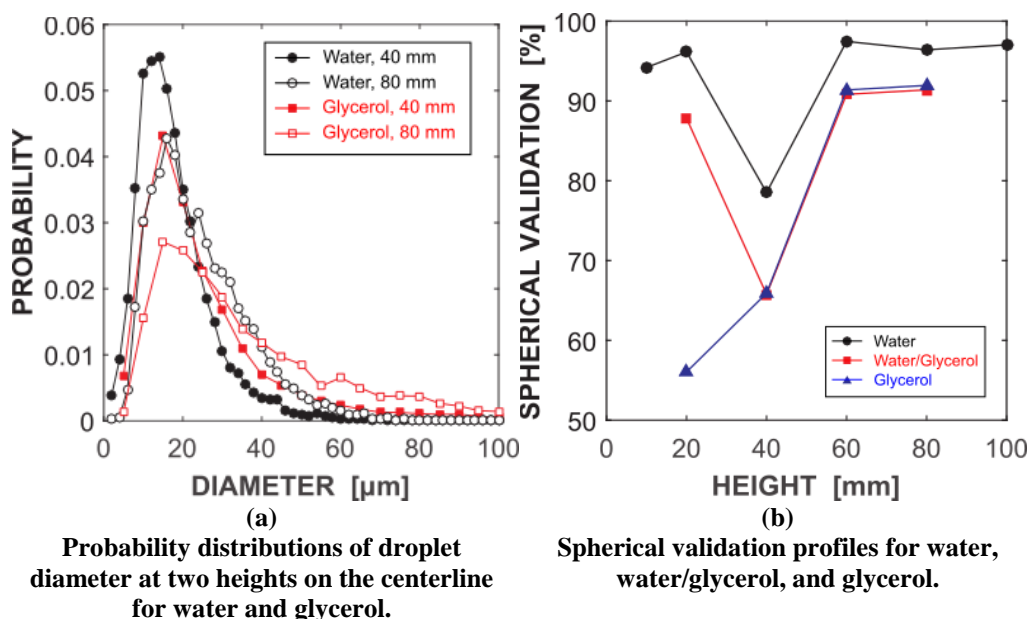
Fig. 59-Probability distributions and spherical validation profiles as influence by viscosity [58].

Figure 59a shows the polydispersive droplet diameter spread and the spherical validation of the spray droplets, as influenced by height and viscosity. For both water and glycerol, we observe a general broadening and shift to larger diameters with increasing height as droplets collided and coalesced. This is in agreement with our interpretation of the droplet profiles in Fig. 57a. We also observe that the probability distributions for the more viscous glycerol included greater probability on larger diameters, which we expect from Fig. 58b.

Figure 59b shows the spherical validation, averaged across the entire radial profile at each height, for the combinations of the water and glycerol that we examined. Spherical validation indicates the percentage of droplets detected by the PDA instrument and processing software that had an acceptably similar diameter (within 5%), as indicated by similar phase differences between detectors 1 and 2 and detectors 2 and 3. We see there is a general trend of decreasing validation with increasing viscosity. This indicates that the more viscous spray plumes required more time for the ejected ligaments to break apart and for the surface tension to force those fragments into spheres.

Though these measurements are not of crude oil, they reveal the general behavior of the atomizer as fluid properties change. Given the wide range of viscosities and densities found in the various crude oils around the world, it is important that we characterize the atomizer behavior and its performance as fluid properties are varied.

Crude Oil Measurements
The crude oil PDA was performed with the annular co-flow burning hydrogen and air to mimic the reacting conditions of the burner and to minimize unburned crude oil from accumulating within the exhaust duct. In general, the spray droplets behaved in agreement with the trends from the fundamental study measurements and our previous work [1]: increasing liquid viscosity increases droplet diameter and increasing atomizer velocity and ALR decreases droplet diameter. With the addition of combustion, the heat further altered the profiles.
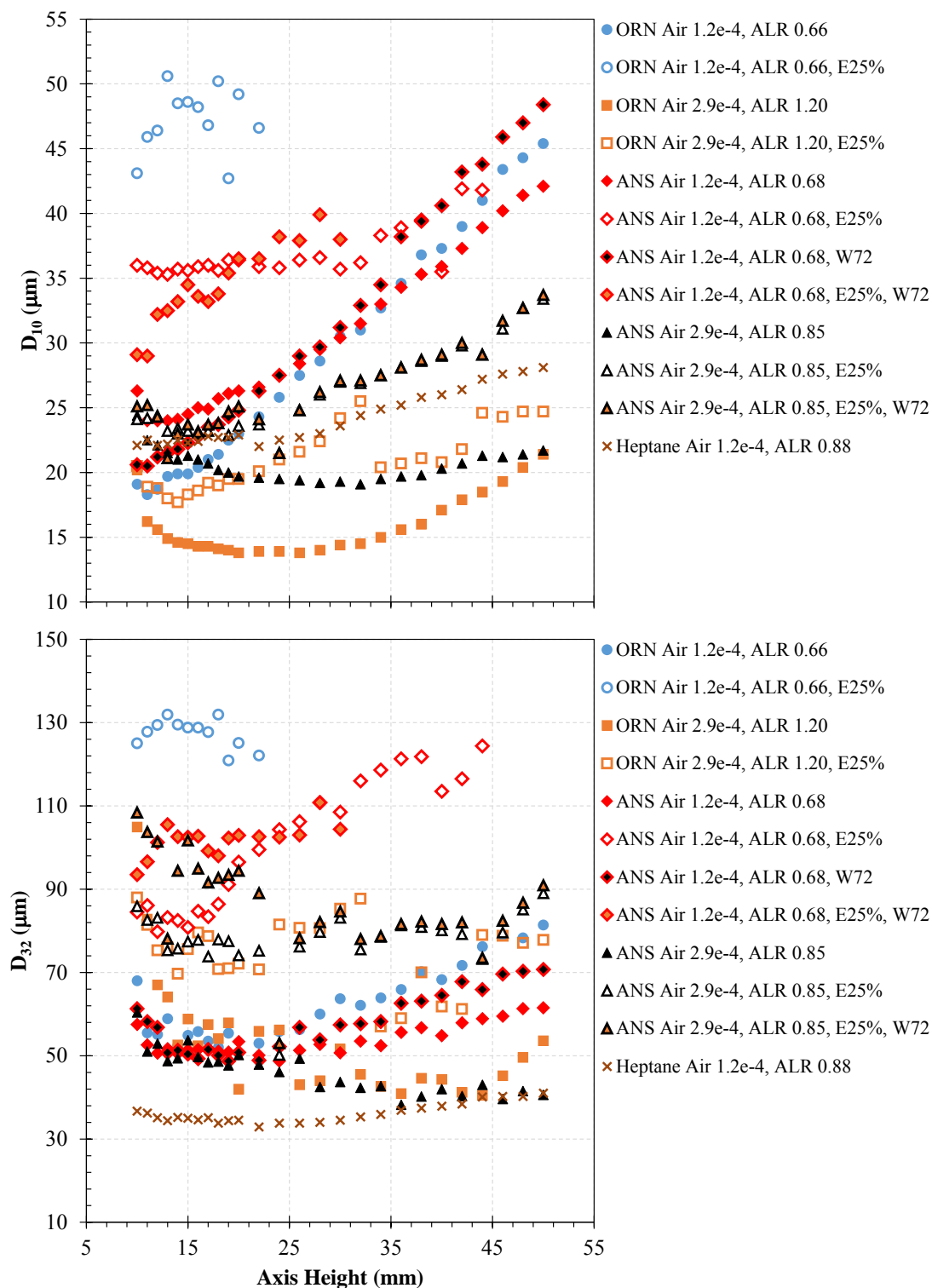
Fig. 60-Droplet measurements along the center axis of the plume. The top plot shows the mean diameters and the bottom plot shows the Sauter mean diameters. The heptane droplet measurements provide a benchmark comparison.

(a)

(b)
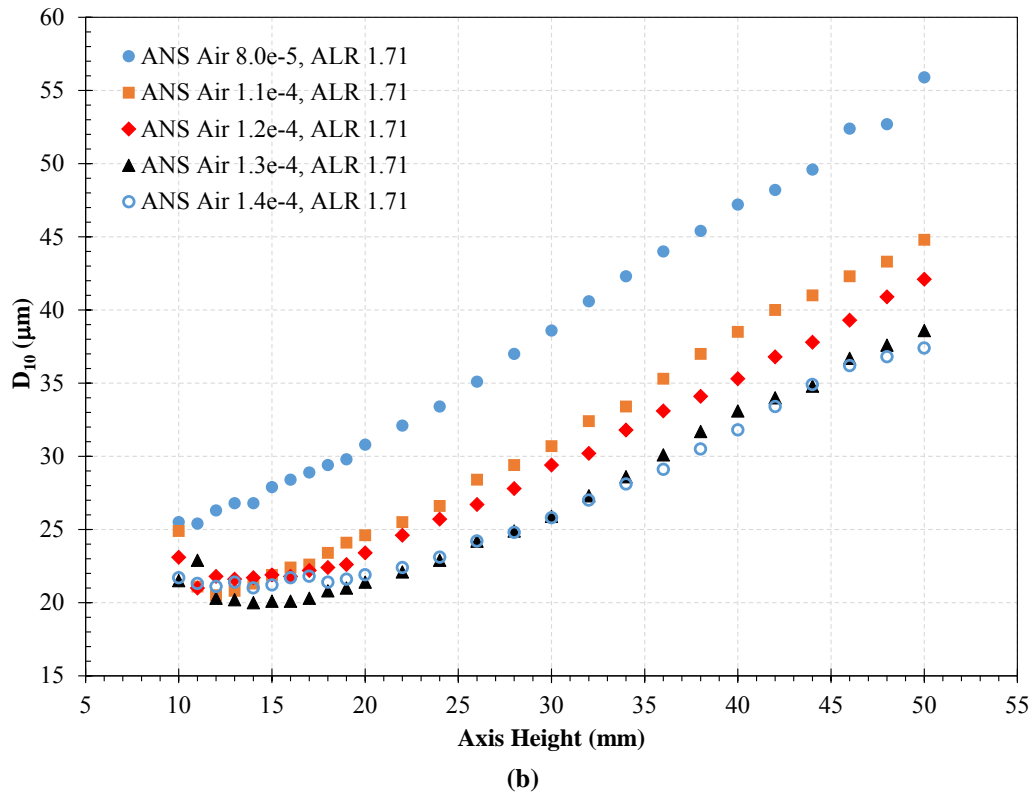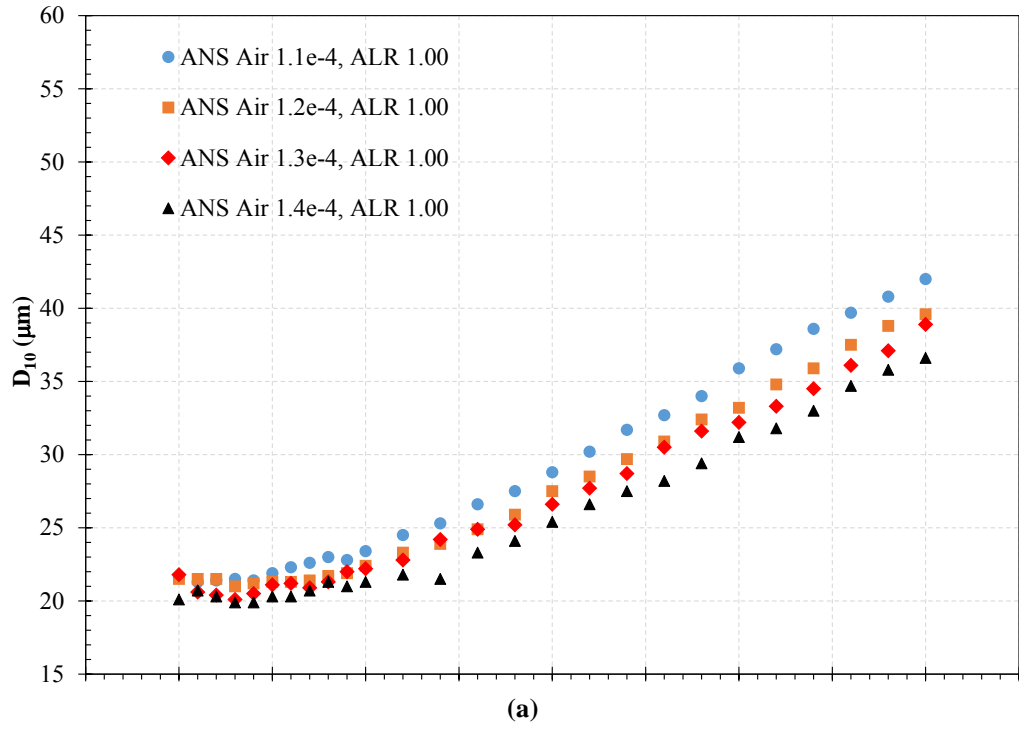
Fig. 61-Droplet measurements along the center axis of the plume for ANS at (a) ALR = 1.00 and at (b) ALR = 1.71 at low air flow rates.

For crude oil, the droplet diameter profiles reveal how the droplets are evaporating and burning along the length of the plume. There appears to be considerably more noise among Sauter mean diameter (SMD) profiles; this is common for higher moment statistics – their calculation reveals the statistical noise in a population. We observe that the heptane SMD profile is much cleaner than many of the crude oil profiles. We suspect that the heptane transparency aids in producing a much cleaner measurement, but such a hypothesis is outside the scope of this study.

If we examine the plots, we can see the general trends we observed with the fundamental measurements: droplet diameters decreased with lower viscosity, higher ALR, and higher air flow rates. For some mixtures, there were considerable measurement problems. The Oriente, 25% emulsified mixtures at the low flow rates produced very large droplets and noisy signals. The Oriente, 50% emulsified mixtures were so viscous that the droplet diameters were greater than the measurement capability of the PDA system.

If we examine the droplet measurements in light of the flame heights, we can see that for most mixtures, as the jet velocity increased, the droplet diameters decreased and the flame anchor height increased. Clearly, the jet velocity influenced ignition delay, with the related mixing and strain, more than the evaporation delay from larger droplet diameters. The exception was at the lowest examined flow rates and ALR values. The higher flame lift heights suggest that the larger droplet diameters delayed the evaporation and subsequent ignition process at the lowest jet velocities.

To address this transitional region in flame height, we gathered droplet measurements with ANS at two different ALR values, for air flows ranging from $0.8\text{-}1.4 \times 10^{-4}$ kg/s, shown in Fig. 61. If we examine the mean droplet diameters at heights above 17 mm, the trend with velocity corresponds with the observed variation in flame height. Below 17 mm, the diameter profiles are so close to suggest that there is very little difference in droplet profiles among the velocities we examined. This is especially relevant since the flames anchor at heights less than 17 mm. This strongly suggests that there are other physical processes influencing the flame anchoring behavior, other than droplet diameter. If we refer to the heat flux measurements in Fig. 54, the higher heat fluxes at lower flow rates suggest that flame radiative heat transfer significant influences the flame anchoring process.

Coherent Anti-Stoke Raman Spectroscopy

There have been a number of unpredictable and significant challenges throughout the period of assembly of optical instruments for the CARS experiment. Fortunately, the laser returned back online a few weeks ago. In a short time, we have been able to generate, collect, and fit CARS spectra to theoretical spectra at ambient temperature and at an elevated temperature. We created by directing heated air at the probe volume. The probe volume is estimated to be a cylinder of 60 microns in diameter and 3 mm in length.
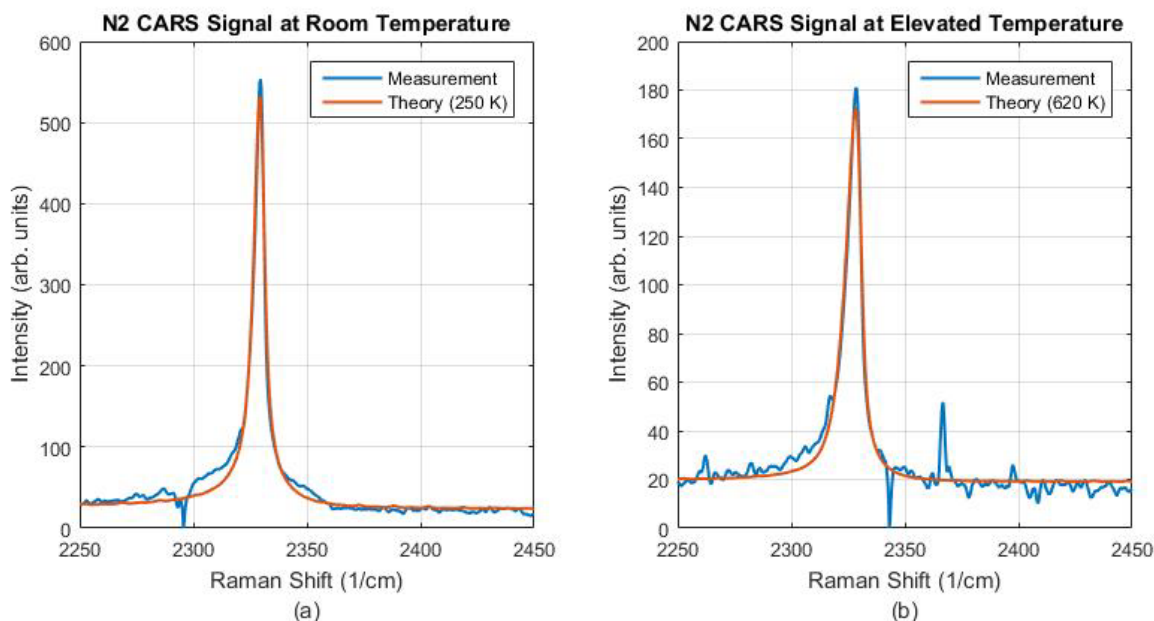
Fig. 62-Nitrogen spectra (a) at room temperature and (b) at an elevated temperature, from heat gun.

Figure 62 illustrates the spectral change in the nitrogen CARS signal as temperature increases. The intensity of the signal decreases and its shape changes as higher transitions are excited with temperature. The theoretical model used to fit the CARS measurements is called CARSFT and was provided by Sandia National Labs. The code utilizes a least-square fitting routine. At relatively low temperatures, the error in these measurements is higher because of the lack of unique spectral features in the CARS signal. At higher temperatures, near 1000 K, additional spectral features appear due to the second vibrational band that is excited which makes this technique suitable for thermometry at combustion temperatures. The fitting routine has resulted in a temperature of approximately 250 K for the room temperature measurement and 620 K for the elevated temperature measurement. The experimental error in these measurements is approximately ±50 K. Although the room temperature was underestimated, the result remains within error. The elevated temperature from the heat gun was confirmed by using a K-type thermocouple and also is within error. Though CARS was not able to provide in situ temperature measurements, it will be used in the wellhead burning study.

Analytical Chemistry Results

A range of analytical measurements were made with the neat (unaltered) crude oils and with the modified crude oils after emulsification, weathering, and burning to understand how these processes changed the chemistry and hydrocarbon distribution. It is helpful that we consider each crude oil, and the subsequent products, as a distribution of many hundred different chemical compounds, each with its own molecular weight and other physical and chemical characteristics. The bulk properties and behavior of the crude oil as it undergoes different processes is due to the combined behavior of all of the many constituents. Therefore, we need to examine the statistical distributions of the compounds, in particular their weight, and how these change as the neat crude oil undergoes the different processes relevant to an oil spill including weathering, emulsification, and combustion.

Baseline Spectra

Spectra from gas chromatography and mass spectroscopy were gathered from the unmixed and unreacted oils to provide baseline comparisons of the molecular weights.
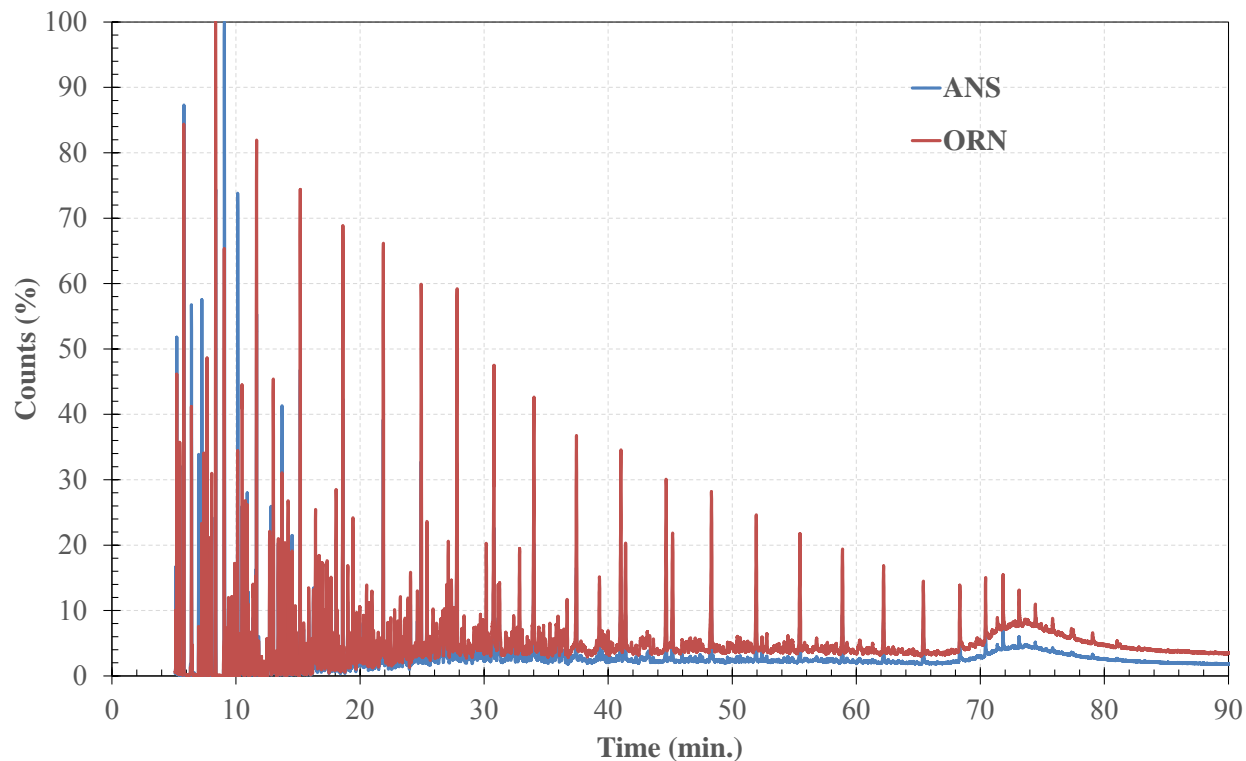
Fig. 63-Comparison of the gas chromatograph of the neat crude oils.

Figure 63 shows the gas chromatographs of the two neat oils, prior to emulsification, weathering, or combustion. Comparing the two oils, we observe that the ANS contains greater lightweight hydrocarbon concentrations, while the Oriente contains greater heavy weight hydrocarbon content. This is consistent with the different density, viscosity, and weight of the oil.

The molecular weight distributions (MWD) were determined for two crude oil samples; Alaska North Slope and Oriente crude oil samples for comparison with soot and exhaust measurements. The signal averaged spectra for the entire 15 min temperature ramp is found in Figures 64 through 66. To highlight the high molecular weight differences between samples, mass spectra were signal averaged over the last five minutes of the temperature ramp representing volatilization temperatures approximately 425 °C to 600 °C and are represented in Fig. 67. The two different sources of crude can be distinguished by their MWD profile. Masses below 150 m/z (~C_{11} in molecular weight) were not collected due to the high abundance of ion fragments that can obscure more important higher molecular weight information. It is likely that the crude oil samples contain material lighter than 150 m/z, however it is not relevant to this study as the light end hydrocarbons will rapidly evaporate and burn in the spray plume. The MWD for Alaska North Slope crude oil sample is between 150 – 975 m/z. The MWD for Oriente crude oil sample is between 150 – 1150 m/z.

Fig. 64-ASAP mass spectra of Oriente Crude Oil averaged over 15 min.
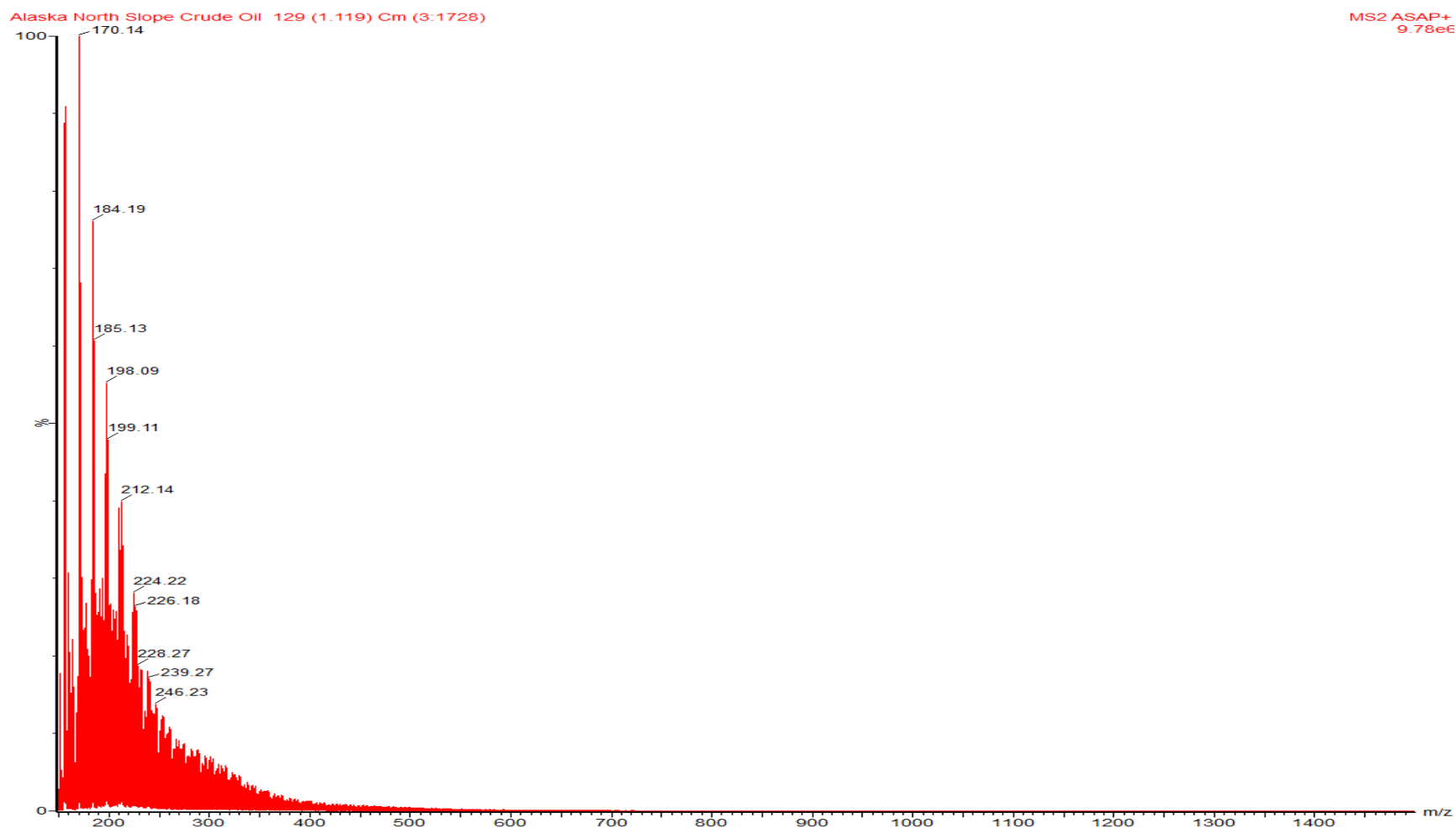
Fig. 65-ASAP mass spectra of Alaska North Slope Crude Oil averaged over 15 min.

(a) Alaska North Slope (b) Oriente
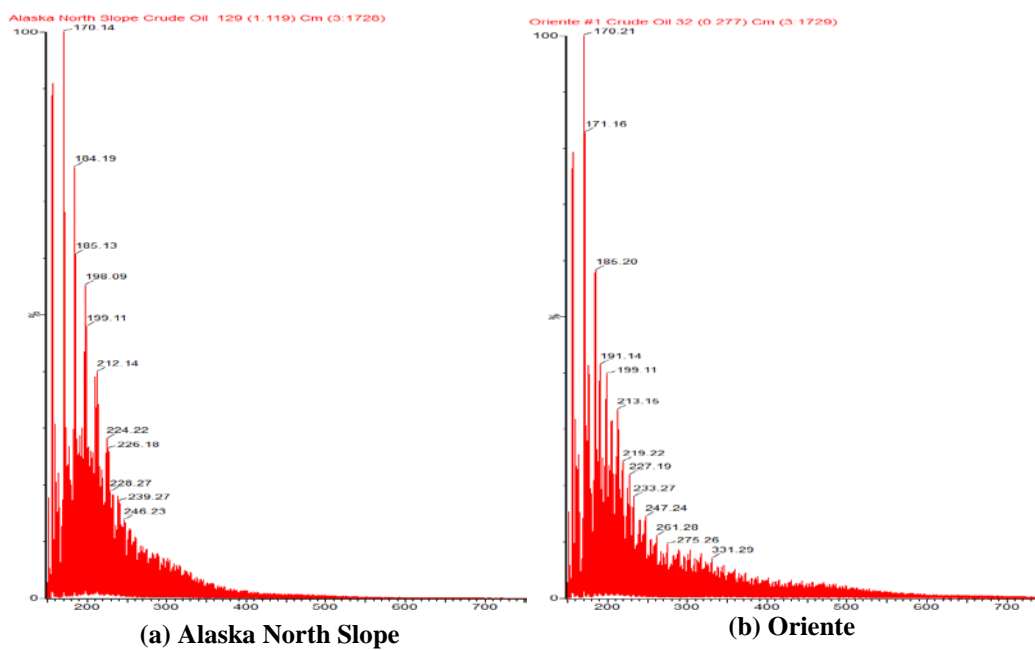
Fig. 66-Comparative ASAP mass spectra of Alaska North Slope and Oriente crude oils averaged over 15 min.

(a) Alaska North Slope   **(b) Oriente**
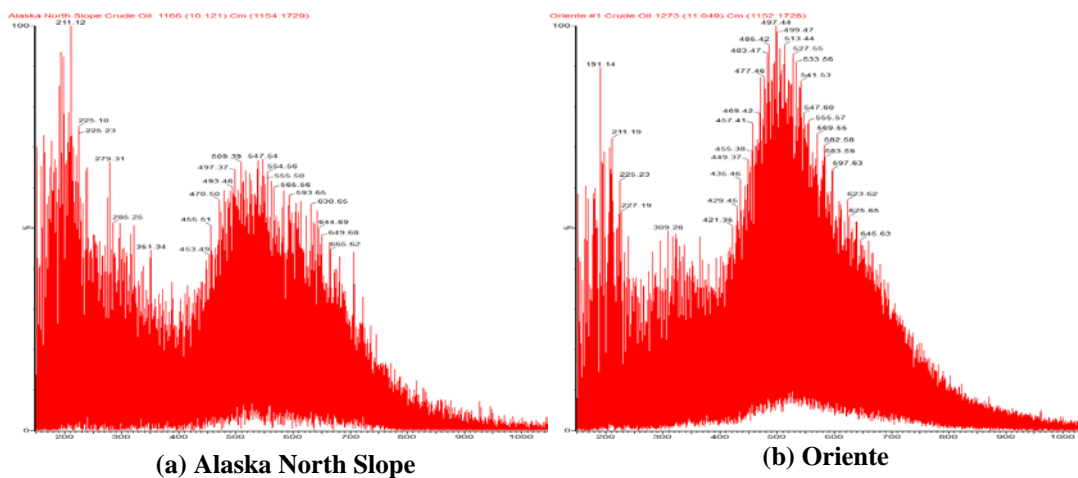
Fig. 67-Comparative ASAP mass spectra of Alaska North Slope and Oriente Crude Oil averaged between 10 and 15 min.

Mass Spectra from Soot Measurements

Soot samples were collected on 47 mm, glass fiber, membrane filters. Analysis was accomplished using the Waters Xevo ASAP system with the same instrumental conditions used in collecting the crude oil mass spectra. The glass capillary tube was wetted with ACS-grade carbon disulfide then rubbed on the soot-coated filter membrane. We used this method to dissolve and coat the glass capillary with sample soot. We show in the following figures the nine filter samples with full range MS from 100 to 1500 m/z and zoomed in spectra from 300 to 1500 m/z to highlight the lower abundance, higher mass ions.

(a) 300-1500 m/z

(a) 100-1500 m/z
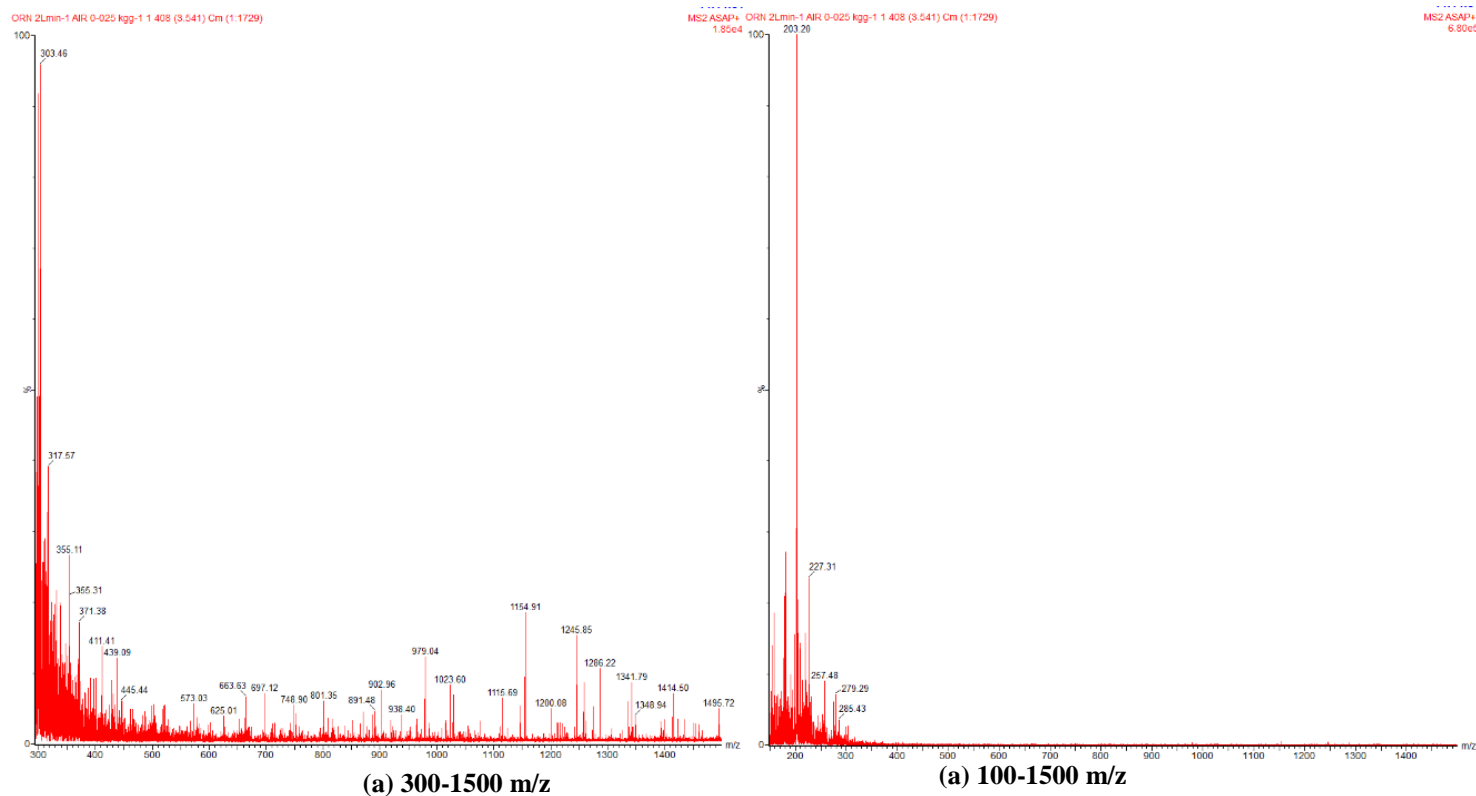
Fig. 68-Mass spectra measured from Oriente crude with a flow rate of 2 L/min, and air flow rate 2.5×10^{-2} kg/s. Test 1 from Table 5.

Although this method is not quantitative, for both crude stocks as crude flow rate increased, the proportion of lower molecular weight constituents decreased. This lower molecular weight material (~200-350 m/z) was in the range of kerosene and diesel crude fractions.

If we compare the spectra in Fig. 68b with Fig. 66b, we find a comparable decrease in higher molecular-weight molecules with an increase in the lower molecular-weight molecules. This shift suggested the combustion and pyrolysis of the higher molecular weight compounds, which is to be expected. We should also note that the remaining molecules were in the range of diesel and kerosene ($C_8 - C_{16}$). This suggests, in addition to our assessment of the burner plume and second stage interaction, that additional air entrainment was necessary to increase the burn efficiency. We should

note the absence of a strong representation from the molecules in the range of 400 m/z and above, where we would expect asphaltene molecules, which suggests that the asphaltenes were pyrolyzing and fragmenting to form lighter molecules[15] or were forming graphitic soot compounds.


(a) 300-1500 m/z

(a) 100-1500 m/z
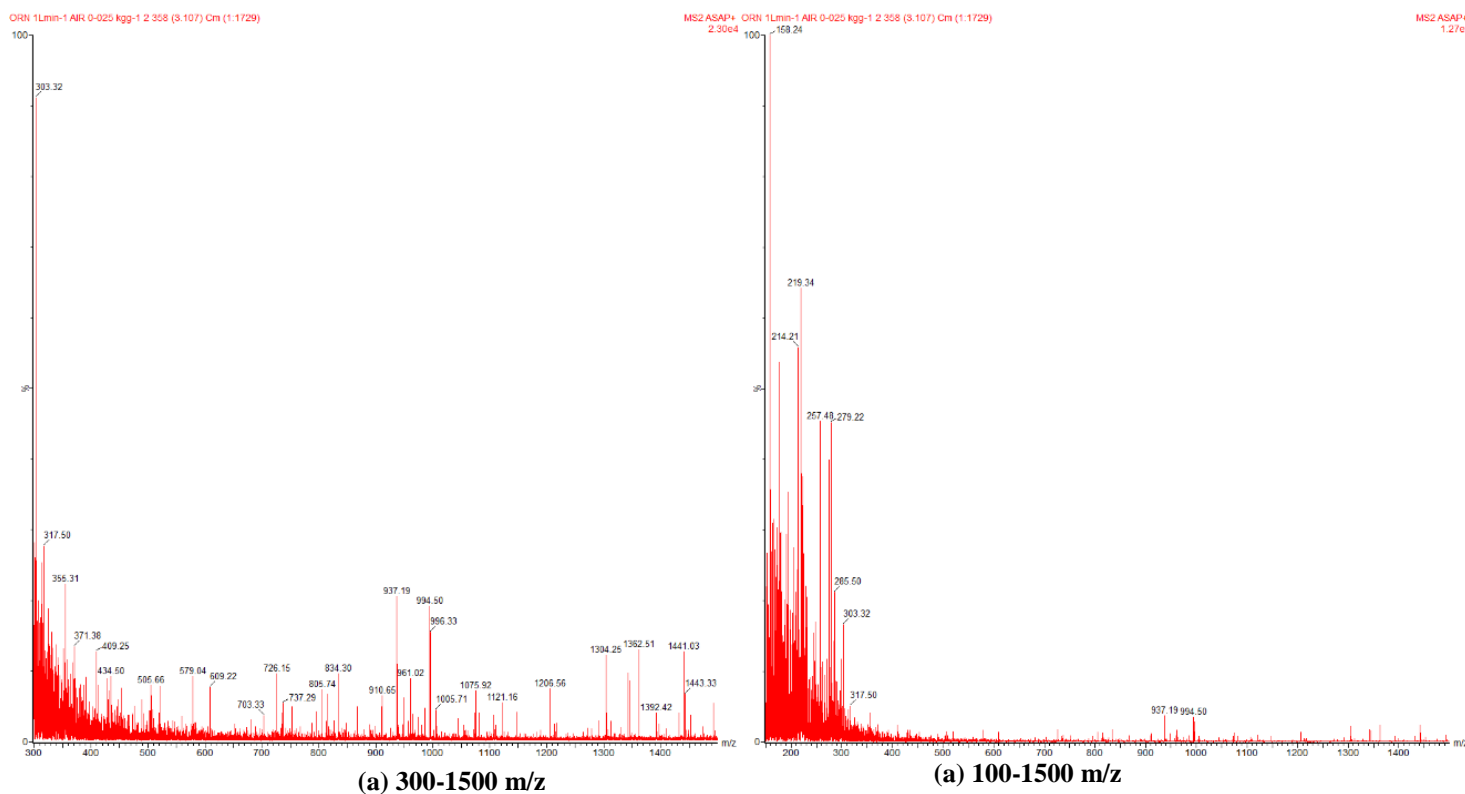
Fig. 69-Mass spectra measured from Oriente crude with a flow rate of 1 L/min, and air flow rate 2.5×10^{-2} kg/s. Test 2 from Table 5.

(a) 300-1500 m/z

(a) 100-1500 m/z
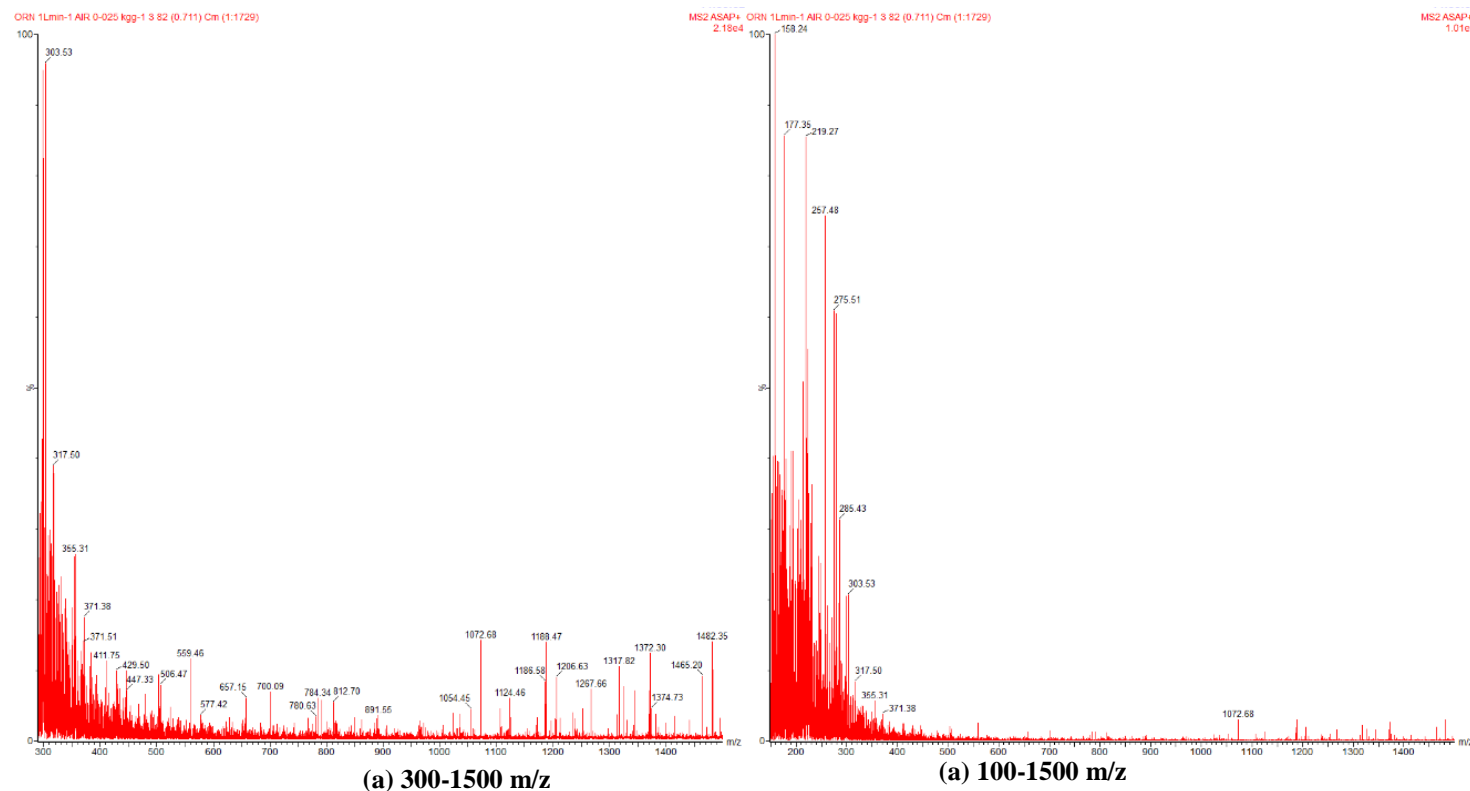
Fig. 70-Mass spectra measured from Oriente crude with a flow rate of 1 L/min, and air flow rate 2.5×10^{-2} kg/s. Test 3 from Table 5.

Figures 69 and 70 are from similar conditions, and show nearly the same results. In comparison to Fig. 68, the oil flow is half, but we observe more low-weight molecules. Again, this corresponds with unburned hydrocarbons. For the sake of comprehensiveness, we have included all of the ASAP spectra from the collected samples in Table 5. What we find is that all of the results from Oriente crude appear similar with one another, while those from ANS appear similar with one another. However, the Oriente and ANS results are distict.
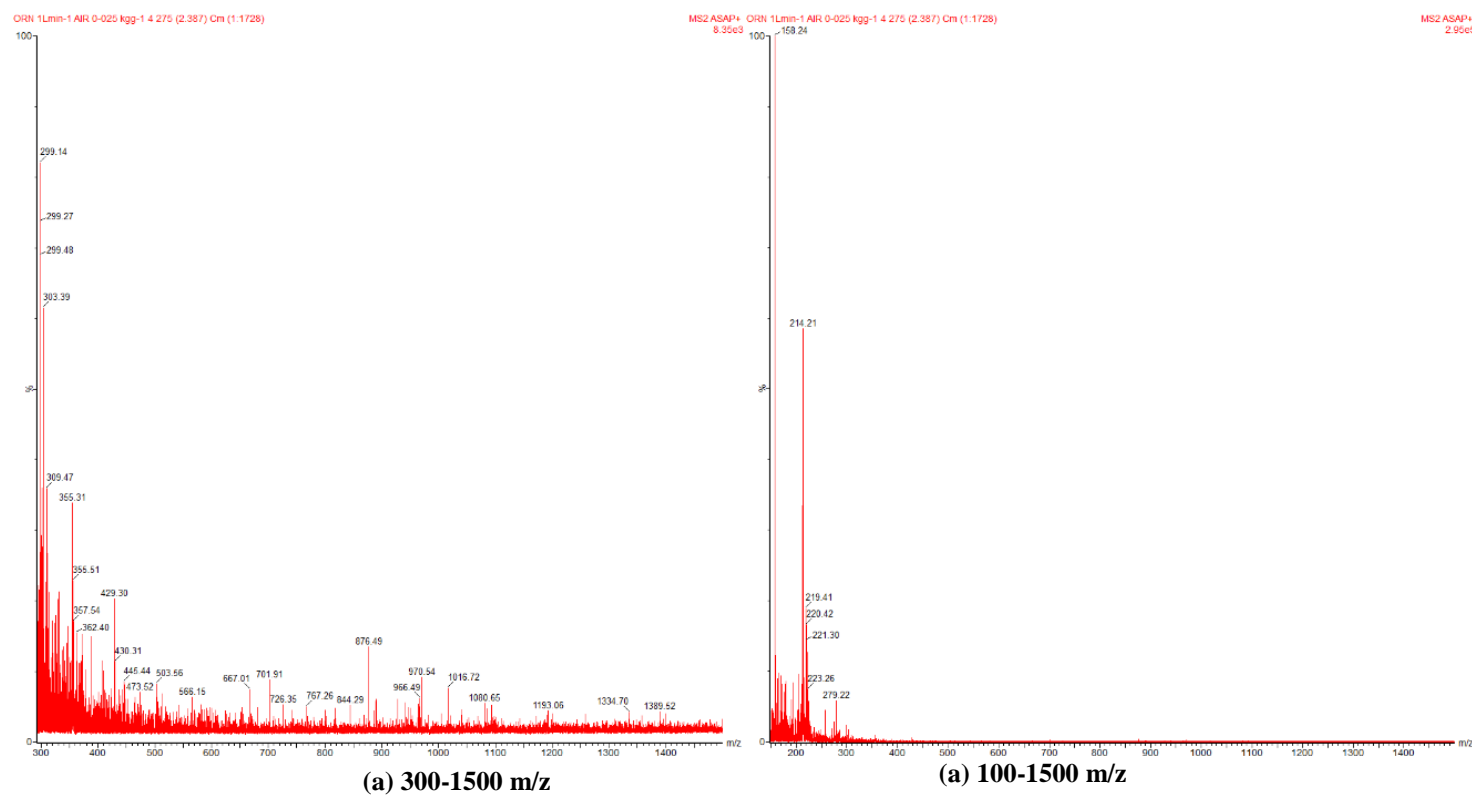
Fig. 71-Mass spectra measured from Oriente crude with a flow rate of 1 L/min, and air flow rate 2.5×10^{-2} kg/s. Test 4 from Table 5.
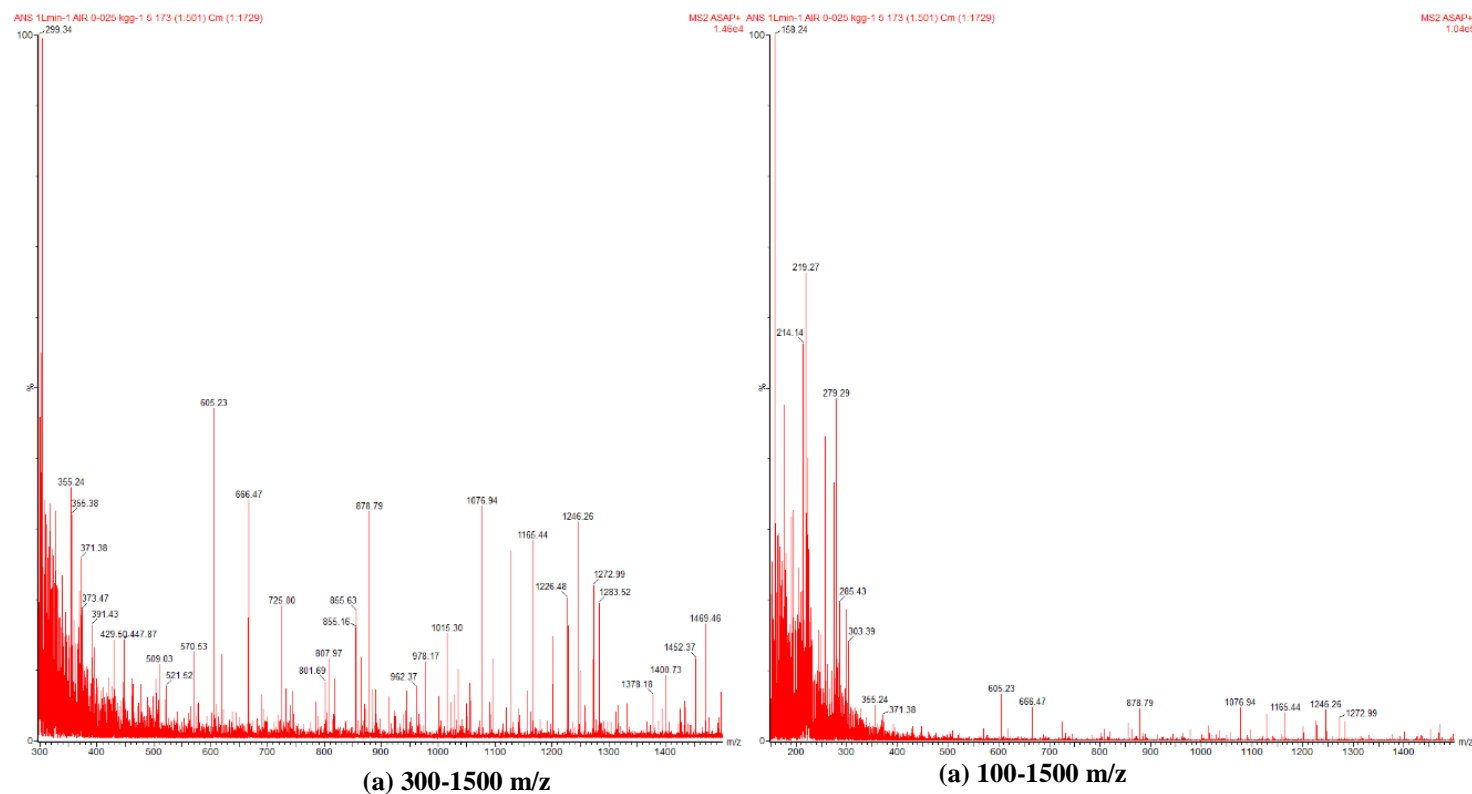
Fig. 72-Mass spectra measured from ANS crude with a flow rate of 1 L/min, and air flow rate 2.5×10^{-2} kg/s. Test 5 from Table 5.
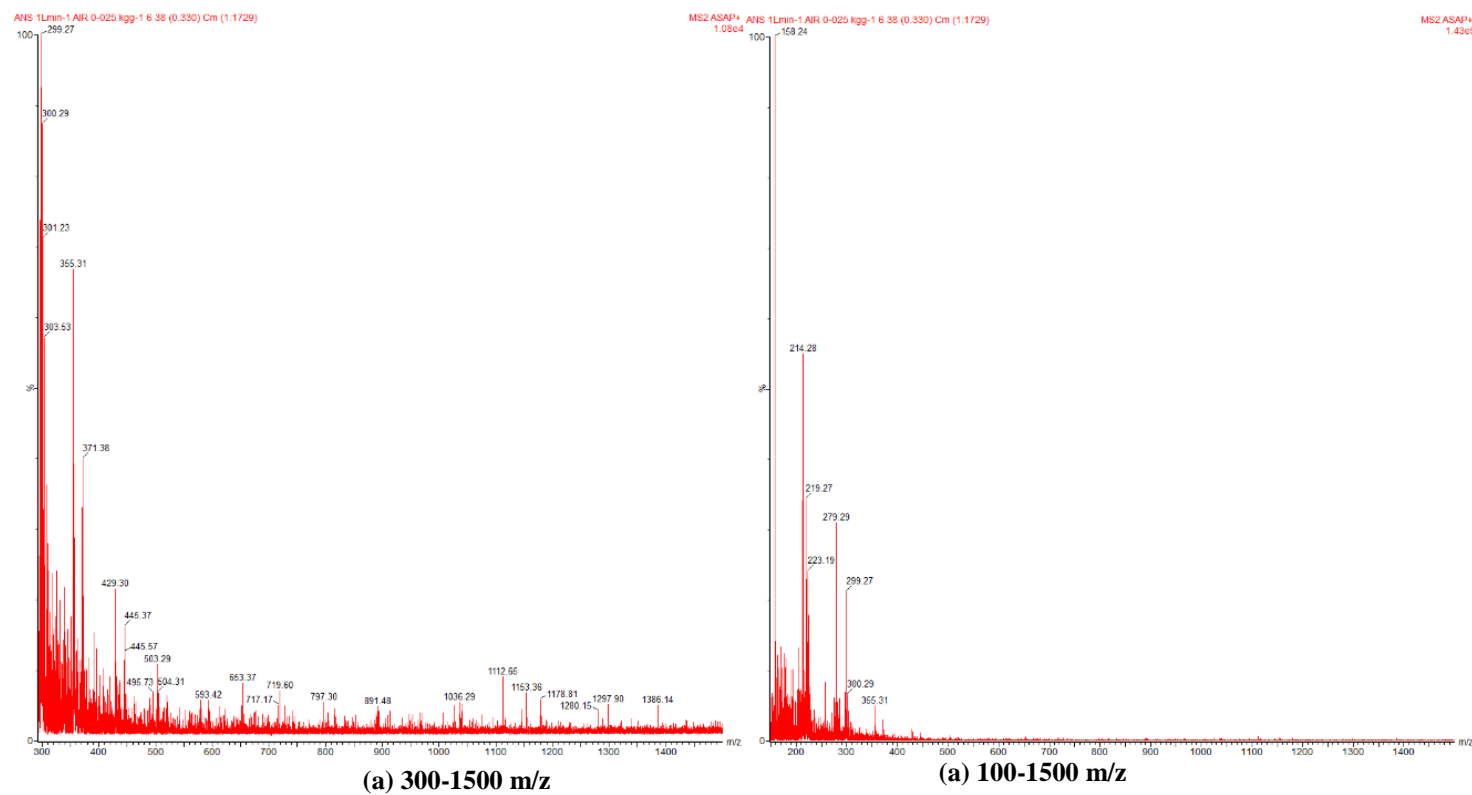
Fig. 73-Mass spectra measured from ANS crude with a flow rate of 1 L/min, and air flow rate 2.5×10^{-2} kg/s. Test 6 from Table 5.
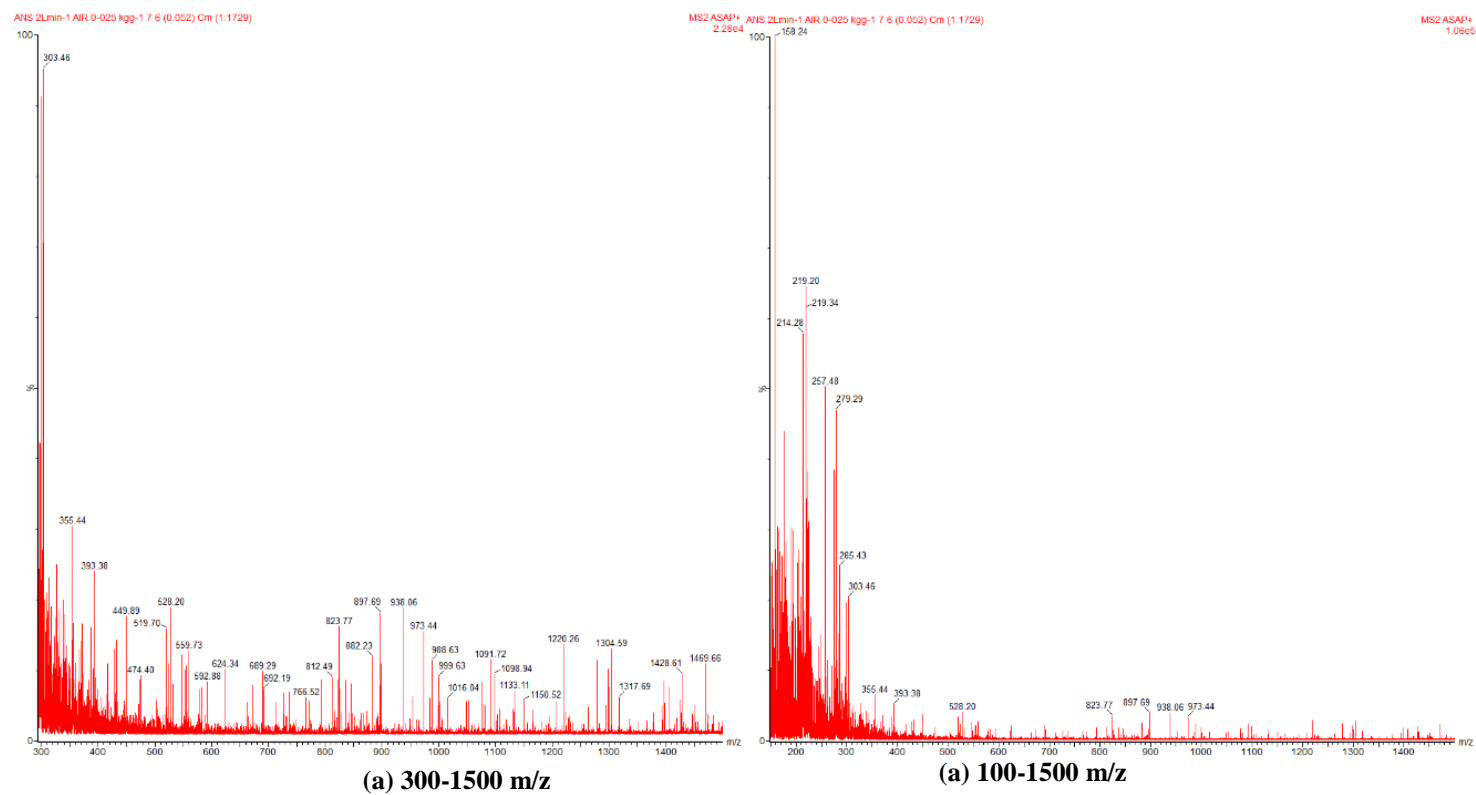
Fig. 74-Mass spectra measured from ANS crude with a flow rate of 2 L/min, and air flow rate 2.5×10^{-2} kg/s. Test 7 from Table 5.
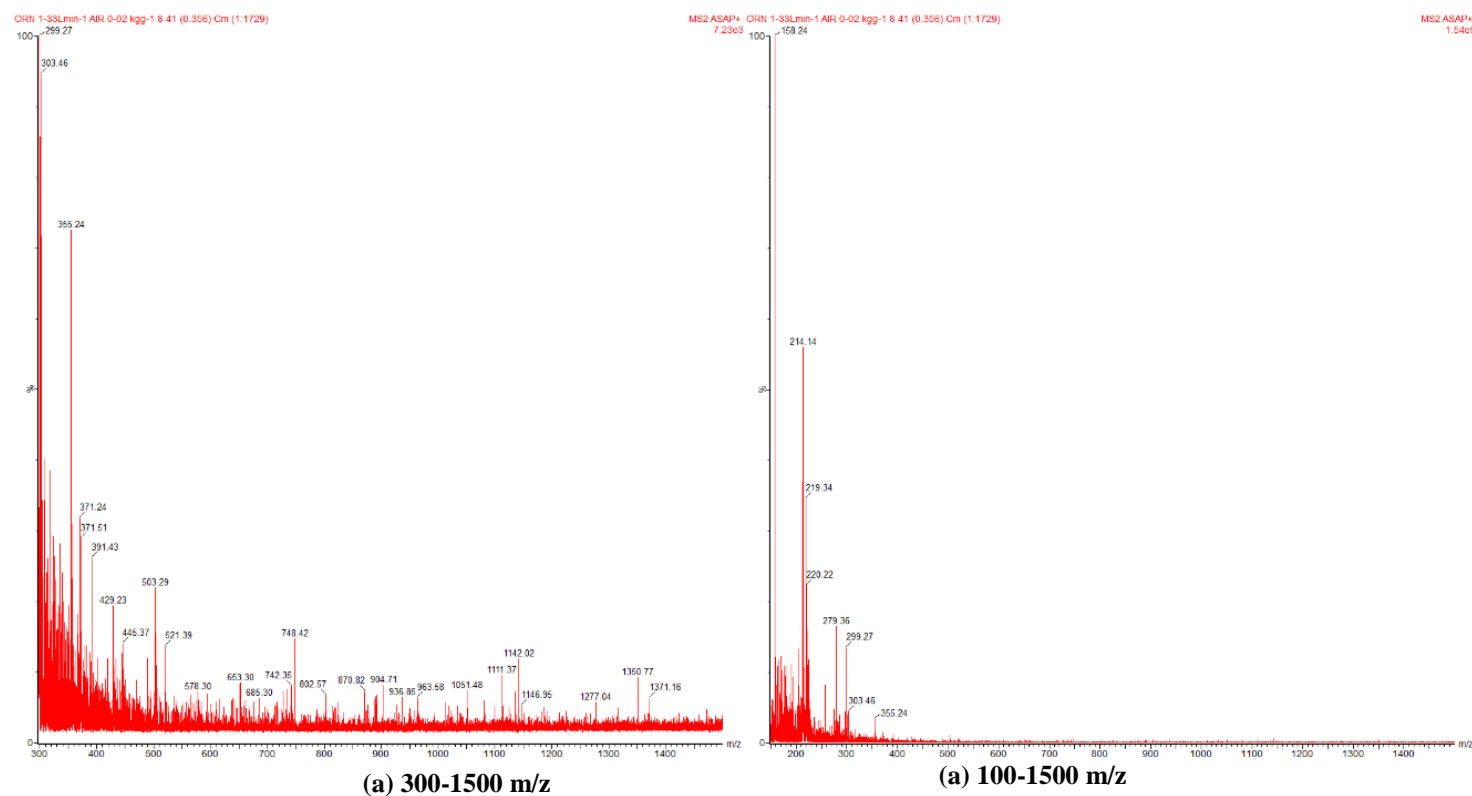
Fig. 75-Mass spectra measured from Oriente crude, 25% emulsified, with a flow rate of 1.33 L/min, and air flow rate 2.0×10^{-2} kg/s. Test 8 from Table 5.

(a) 300-1500 m/z

(a) 100-1500 m/z
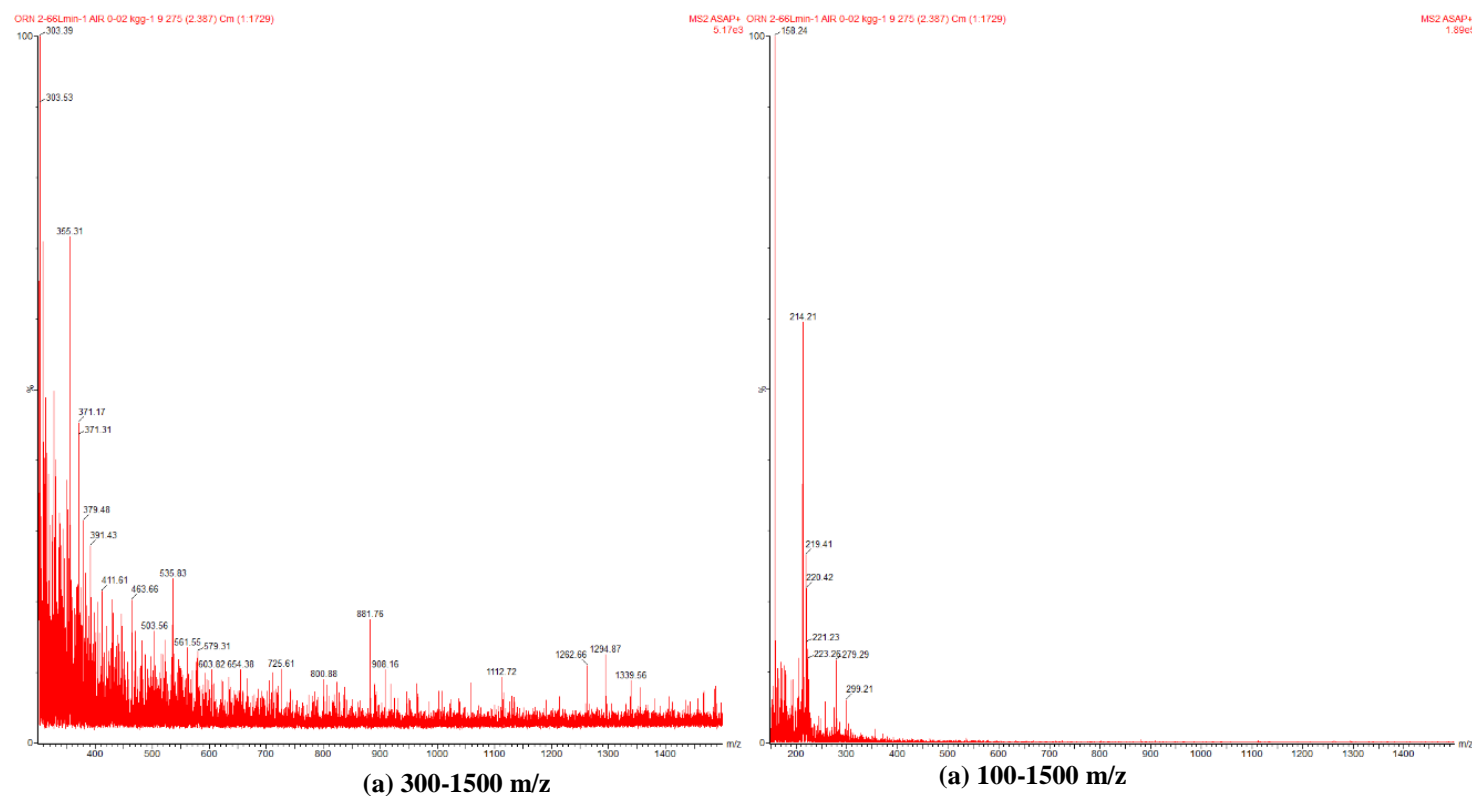
Fig. 76-Mass spectra measured from Oriente, 25% emulsified, crude with a flow rate of 2.66 L/min, and air flow rate 2.0×10^{-2} kg/s. Test 9 from Table 5.

We should note that in Figures 75 and 76, which were both collected from the burning of 25 % emulsions, that there is no significant difference in the distributions in comparison to those collected with pure Oriente.

Gas Chromatograph of Weathered Oil
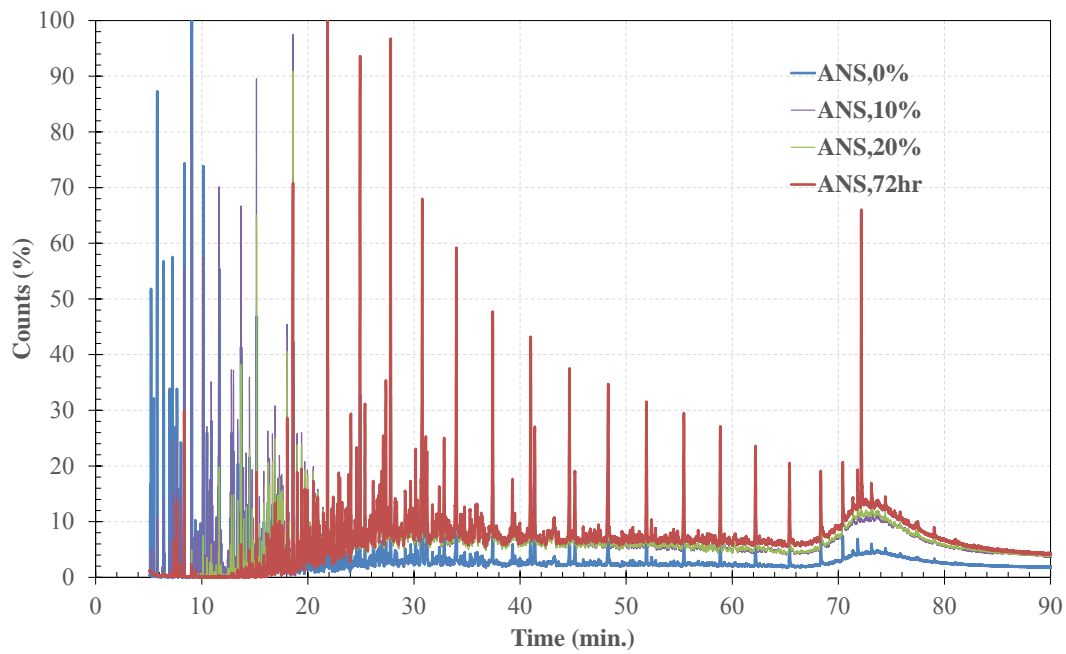
(a)
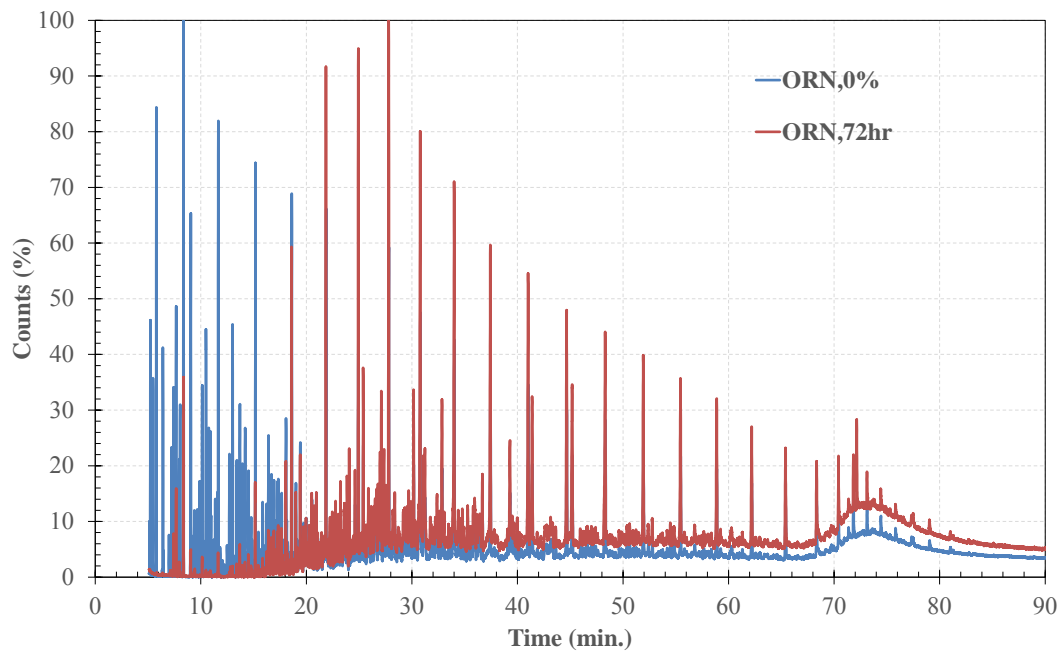
(b)

Fig. 77-Comparison of the gas chromatograph of the neat crude oils with their weathered counterparts. (a) Alaska North Slope and (b) Oriente. The decrease in lighter hydrocarbons and the increase in heavier hydrocarbons with weathering is apparent for both crude oils.

Chromatography measurements of the crude oil were measured from samples at different times in the laboratory weathering to determine how the hydrocarbon distribution was altered over time as the crude oil was aerated with dry nitrogen.

Spectra from Exhaust Measurements
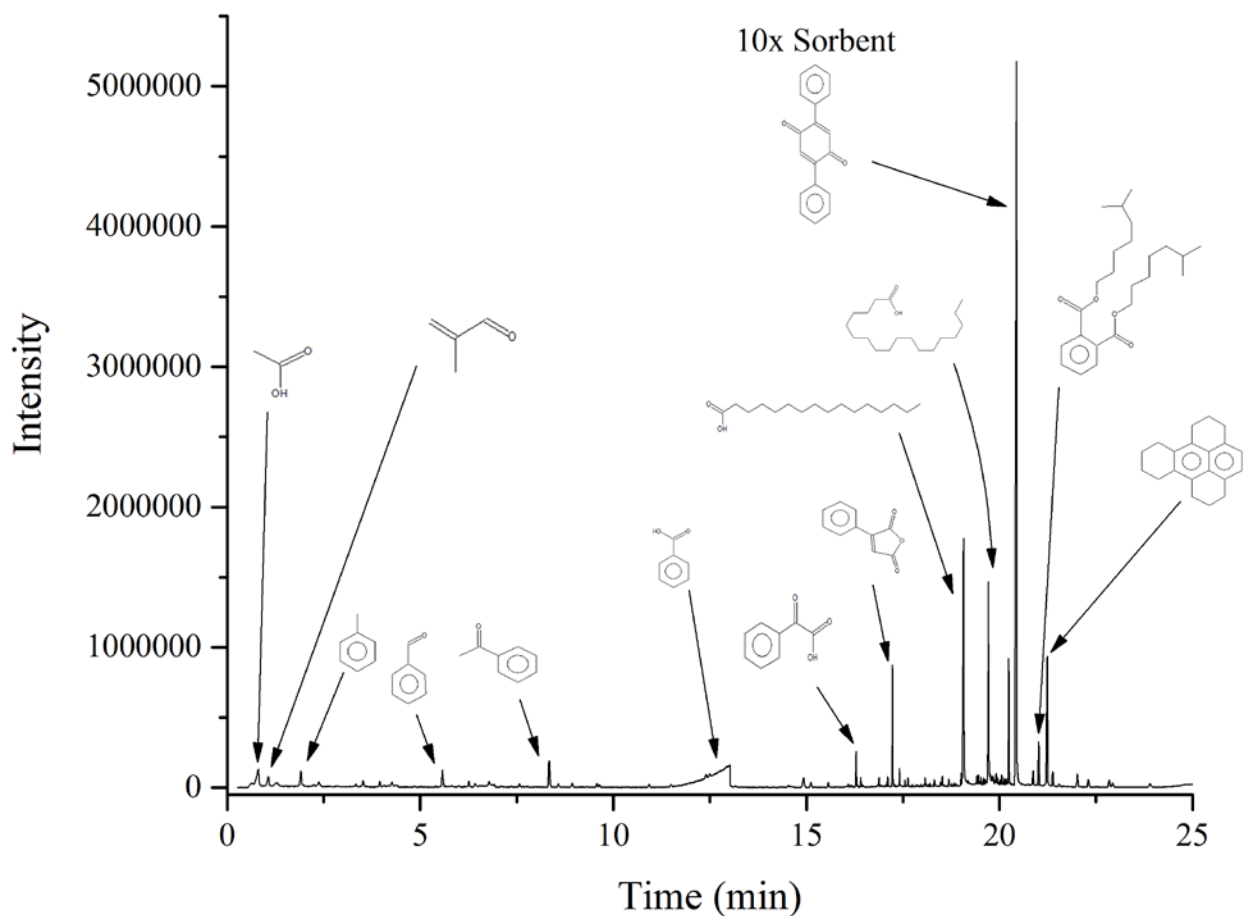
Fig. 78-Baseline spectra from exhaust samples gathered in a sorbent tube for neat ANS burned in a laboratory spray plume with $\dot{m}_{Air} = 2.9 \times 10^{-4}$ kg/s, $\dot{V}_{Oil} = 23.2$ mL/min (see Table 3).
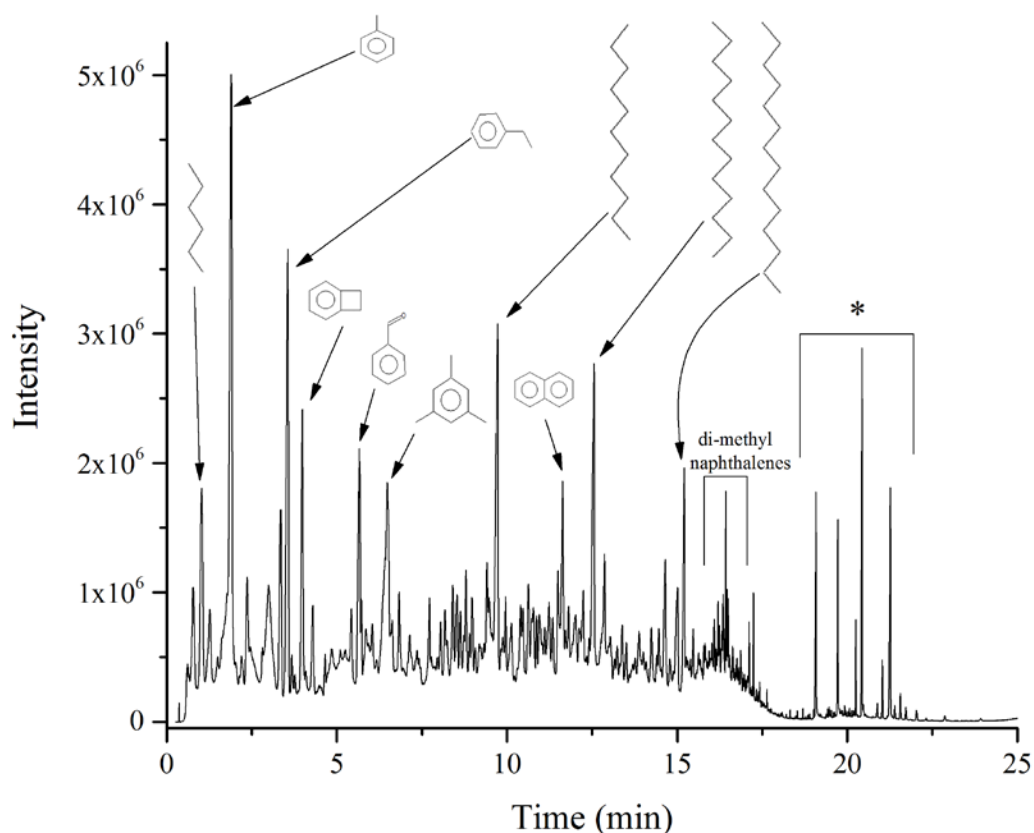
Fig. 79- Spectra from exhaust samples gathered in a sorbent tube for 25% emulsified ANS burned in a laboratory spray plume with $\dot{m}_{Air} = 2.9x10^{-4}$ kg/s, $\dot{V}_{Oil} = 23.2$ mL/min (see Table 3). * denotes major peaks identified in Fig. 78 from the baseline neat ANS crude

Figures 78 and 79 show the mass spectra of neat ANS and emulsified ANS (25% synthetic seawater), burned at an airflow rate of $2.9x10^{-4}$ kg/s and a liquid flow rate of 23.2 mL/min (see Table 3). For the neat ANS, combustion was steady and stable. For the 25% emulsified mixture, combustion was unstable and poor. We should note that in the actual burner, the combustion of the emulsified crude at 25% is stable and appears complete. For both samples, there were large numbers of polycyclic aromatic hydrocarbon (PAH) compounds at around 20 minutes in the spectra. These molecules are precursors to larger soot agglomerations and are common in most hydrocarbon flames.

There are clear differences in the total ion chromatographs (TIC) between the baseline and emulsified ANS exhaust composition. Large peaks in both figures are identified with their respective structure. The emulsified samples show clear evidence of incomplete combustion, in comparison to the baseline measurement, with almost four times the number of components detected. The large peak at approximately 21 min is from the sorbent itself. The emulsified crude oil combustion products contain a wider variety of oxygen bound material in the form of alcohols, aldehydes, and ketones (not shown in the Fig. 78). Additionally, trace amounts of aliphatic sulphonic acids were detected. No obvious signs of chlorinated hydrocarbons were detected. If present, they would be below the detection limit of this method which, including the pre-concentration from the TDS sorbent tube, would be in the low ppb to ppt range. The large increase in low molecular weight hydrocarbons could be caused by the absorption of heat energy within the plume by the water within the emulsion.

90

Though we were concerned about the presence of chlorinated hydrocarbon (CHC) compounds in the exhaust, particularly those bound to aromatics, their formation from the salts found in seawater is not a favorable reaction pathway in a combustion environment. Chlorine addition reactions typically occur through nucleophilic addition chemistry over a carbon-carbon double bond in solution; an example is the reactions that occur in paper pulp chlorine bleaching. In polar protic solvents, like water, hydrogen bonding will hinder the nucleophile through solvation, preventing or heavily limiting the addition of chlorine. In short, this chlorine addition is typically a solution-based reaction and is not known to produce chlorinated hydrocarbons in a plasma.

This observation is consistent with coal combustion pollutants. Though untreated coal combustion emissions contain sulphur oxides, nitrogen oxides, inorganic salts, and metal compounds, they typically do not contain appreciable CHCs [59]. Low-emission coal burning technology does not produce appreciable chlorinate hydrocarbon compounds because CHCs form in combustion in the process of incomplete, or inefficient combustion [60]. Efficient combustion processes will create conditions for these compounds to react to form CO_2, H_2O, and the very reactive hydrochloric acid (HCl), which then reacts with and is trapped by exhaust scrubbing systems. In contrast, municipal waste burning, which contains chlorinated hydrocarbons such as polyvinyl chloride (PVC), produces additional chlorinated hydrocarbons during combustion [61].

Summary

A wide range of laboratory activities were carried out to examine fundamental crude oil spray combustion behavior and how it was influenced by emulsification, weathering, and atomizer operation. Basic flame geometry, ignition, flame radiation, and spray droplet distribution were documented and examined. Laboratory practices for the emulsification and laboratory weathering of crude oil were developed and established, as well as measurement practices to determine the density, surface tension, viscosity, and index of refraction of neat and blended crude oil. A laser system for nitrogen thermometry was developed to measure gas-phase temperature within the spray plume using coherent anti-Stokes Raman spectroscopy.

There were a range of significant discoveries made in the laboratory that both revealed new science and aided the design and performance of the sub-scale and engineering-scale burner. Flame anchoring studies revealed low velocity and ALR ranges, with minimal ignition delays, that we then used to determine what burner flow rates would ignite reliably.

Analytical chemistry methods revealed the baseline hydrocarbon constituent distribution of the neat, weathered, and reaction residuals. Mass spectroscopy revealed that poor combustion stability in emulsified mixtures produces a wide range of oxygenated hydrocarbons, which provides a potential pathway in developing chemical or spectroscopic sensors for detecting combustion lean blow off.

During these studies, we discovered a number of important insights into the flame anchoring behavior of crude oil spray plumes and the interactions of droplet behavior, flame radiation, and jet velocity. First, we discovered the strong influence heat transfer has on the droplet ignition. When anchored with propane flames ($\phi = 0.69$, $T_{ad} \approx 1860$ K), even the highly emulsified flames exhibited negligible ignition delay and stable combustion. But, this high temperature did not correspond with the recirculation zone temperature and ignition delay behavior observed in the actual burner, so we used a hydrogen-air flat flame with $\phi = 0.30$ and an adiabatic flame temperature of 1190 K, which exhibited much greater ignition delay. The cooler flat flame transferred heat to the flame largely through convection. By observing the flame structure and spray behavior in tandem, we discovered that the droplet behavior did not vary significantly with the flow rates we examined, but the flame behavior varied a great deal. When measuring the flame lift off and flame radiation, we observed that the flame height decreased and the flame stability improved as the radiant heat transfer increased from the combustion plume. Since convective heat transfer to the droplet occurs largely

from the mixture of the hot co-flow from the flat flame and the atomizing air, there is negligible convective heat transfer from the burning plume to the upstream of the plume. The principle heat transfer mechanism of heat transfer from the burning plume to the upstream spray is radiation. Once a sufficient radiative heat transfer is established, the rest of the plume will ignite because the droplets will evaporate.

APPLICATION & COMPARISON

Before concluding, we think it relevant that we discuss how the combustor we developed might integrate with current oil spill remediation systems and how it compares with burners already in development. The current oil spill systems range in application scale. We anticipate that this burner will be used where *in situ* burning (ISB) methods cannot be applied: inland waters, small vessels, and emulsified crudes all present challenges to current ISB capabilities. Though a range of burners have been studied in the past, the most recent is that being developed by S.L. Ross. It is a simple design that requires a small infrastructure footprint. In the case of both this burner and that of the S.L. Ross, the ideal application is to place the burner on a small, towed barge behind a skimming vessel [62]. This concept fits well with the current methods and technology used in the US and fielded by government and corporate entities.

Current Oil Spill Remediation Systems
In this section, we briefly describe the current systems that the Navy's SupSalv (SEA 00C, Office of the Director of Ocean Engineering, Supervisor of Salvage and Diving) employs for oil spill cleanup. In particular, we describe the MARCO SK0711 Class V standalone vessel and the Vessel of Opportunity Skimming System (VOSS). This is not a thorough review, but this discussion provides a perspective of where the burner we are developing will fit into existing systems.

We begin with a brief description of oil skimmers, followed by more detailed descriptions. Oil skimmers all operate using the same process: they gather fluid, separate the oil from that fluid, and then pump the oil to some reservoir. Encountering, gathering, separating, and pumping may each limit the processing rate of a particular system. Furthermore, for some systems, such as weirs, there is a great deal of liquid water that is gathered, in addition to any pure or emulsified crude oil that may be gathered. In such cases, a vessel may either have to store both the seawater and oil, or if allowed, it may decant what has been gathered into a reservoir. Manufacturers typically report an ideal, effective daily recovery capacity (EDRC), typically referred to as the "Name Plate Capacity" that needs to be verified by ASTM F2709-08 [63]. These values are adjusted to assume 12 hours of daylight and a BSEE, Coast Guard and/or Navy-certified reduction in capacity to reflect real conditions, such as waves, wind, thin oil slick, and so forth. A nominal rating reduction is by 80%.

Table 13-Performance comparisons for skimmers in the U.S. Navy's SupSalv inventory.

| Skimmer	Form	bbls/day	L/min
MARCO Class V [2]	Belt	4320	397
Class V Skimmer with Moyno Progressive Cavity Pump [64]		1234	114
Class V Skimmer with DS 210 [64]		1371	126
Destroil with DS 150 pump [64]		603	55
Destroil Skimmer w/DS 210 pump [64]		1371	126
Desmi Termite [64]	Weir	1509	139
Desmi Terminator [64]	Weir	3017	278
Class XI with DS 210 pump [65]	Belt	1371	126
Desmi Mini-Max 24" Diameter [66]	Weir	1509	139
Lamor LWS-50 [65]	Weir	1440	132
Lamor Minimax 12 Skimmer [65]	Brush	362	33
Douglas Skim-Pak 4200 [65]	Weir	466	43
Douglas Skim-Pak 2200 [66]	Weir	261	24
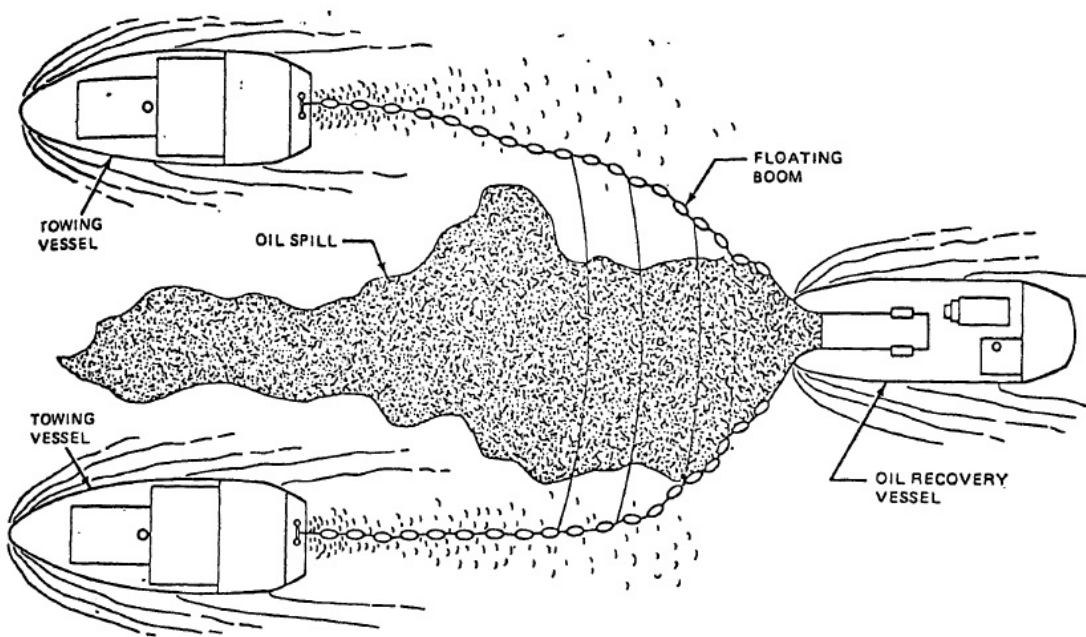
Fig. 80-MARCO Oil Recovery Schematic [2].
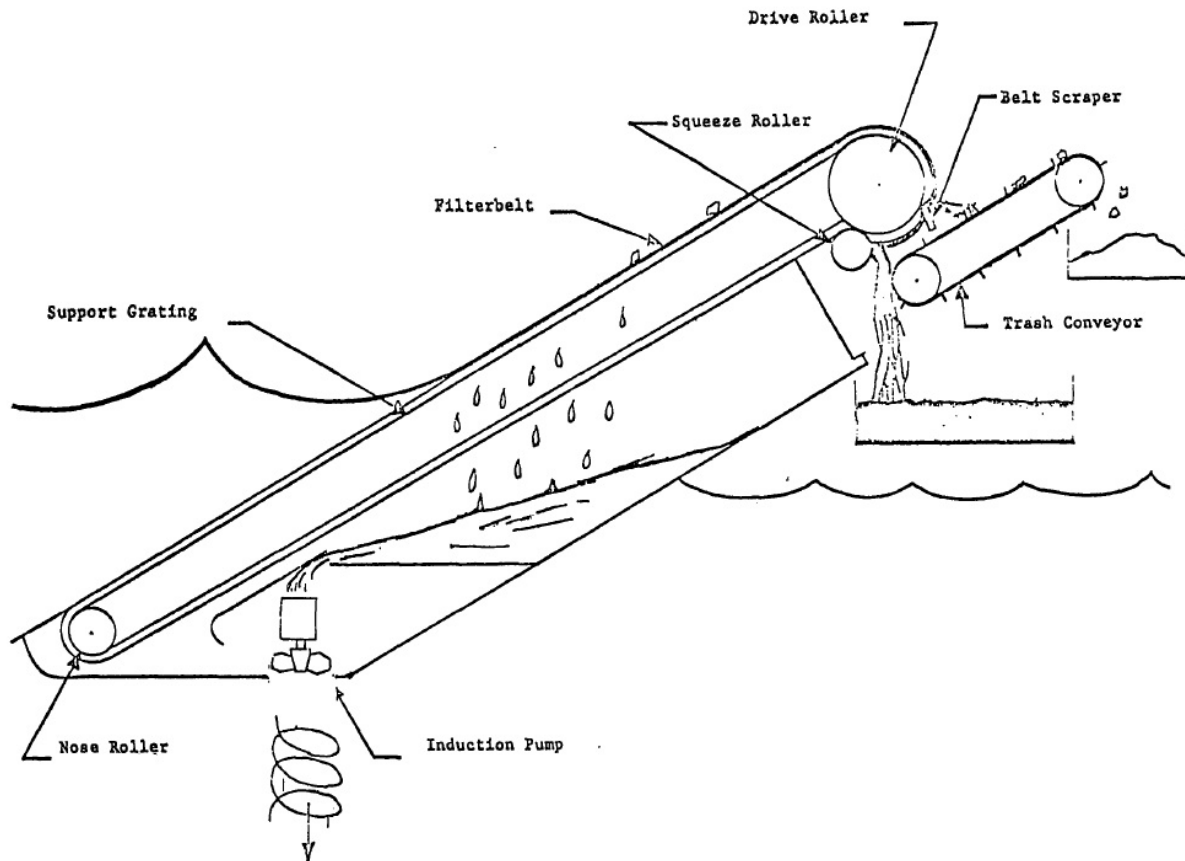
Fig. 81-Operations of Class XI System Sorbent Belt Oil Skimmer SK0924 as deployed in free floating model or on Marco Class V Vessel [2].

MARCO Class V Vessel

The MARCO Class V vessel is at the center of a three-vessel oil spill response system [2]. It skims oil at a flowrate nearly 3 times greater than its closest competitor. This belt skimmer was first introduced to the fleet in the late 1970's. The skimmer is dragged along the water at the apex of a V formation, the towing vessels are connected to the skimmer by steel chain-reinforced inflatable booms dragged by the towing vessels. This arrangement is depicted in Fig. 80. The two towing vessels are set about 65' apart corralling oil from a large surface to the skimmer where it can be picked up.

While in tow, the MARCO vessel faces forward and the bow points into the waves, but while collecting oil the boat is dragged along stern first. The belt skimmer housed in the stern points down into the oil spill. A detailed schematic is shown above in Fig. 81; all belts spin clockwise. This skimmer is attached by inflatable booms, reinforced with steel chain, to two towing vessels. As the skimmer is dragged through the water oil collects in front of the belt. The skimmer's belt is long to handle changing water level due to waves and the lowering of the ship in the water as the tank fills up. The oil slick sticks to the belt's oleophilic surface. As the belt spins, the oil is carried out of the water, the skimmer then separates water from oil and debris. Then the debris is scraped off and the oil is wrung out of the belt by a roller, as seen in Fig. 81. Oil is collected first in an internal storage tank. When the 1 Kgal sump is filled the oil is pumped into a storage bladder towed behind the vessel. These bladders come in 3 sizes: 21, 26, and 50 Kgal.

94

We should also consider how many bladders can be filled on one sortee. The vessel has a 75 gallon fuel tank and consumes fuel at 6 gal/ hour. This yields an operating time of about 12 hours. At a recovery rate of 105 gal/min for 12 hours, the MARCO V can recover nearly 76 Kgal of oil, which is equal to the capacity of the two large bladders. The third bladder is most likely kept on board for choppy waters and stormy weather, which mixes more seawater with the oil, reducing the net oil collection rate while requiring more volume to contain the same amount of crude oil.

Vessel of Opportunity Skimming System (VOSS)

While the MARCO V cleanup system is effective, it cannot be moved easily. Some of the vessels variants require a wide load permit to move by truck. The belt skimmer itself weighs 4300lbs, and the whole vessel is over 10 tons. If the MARCO V cannot arrive in time or more help is needed to clean up the spill in a timely manner, additional water craft can be hired to aid in the cleanup effort. These craft are referred to as Vessels of Opportunity. Usually fishing or shipping boats, these vessels are outfitted with oil spill cleanup equipment. The specially outfitted Vessels of Opportunity make up the VOSS. The beauty of this system is its versatility; however, this can make listing specific technical specifications difficult. The VOSS can be used with virtually any vessel large enough and comes with a variety of different oil skimmers to be deployed depending on conditions. A few common skimmers are detailed in this report.
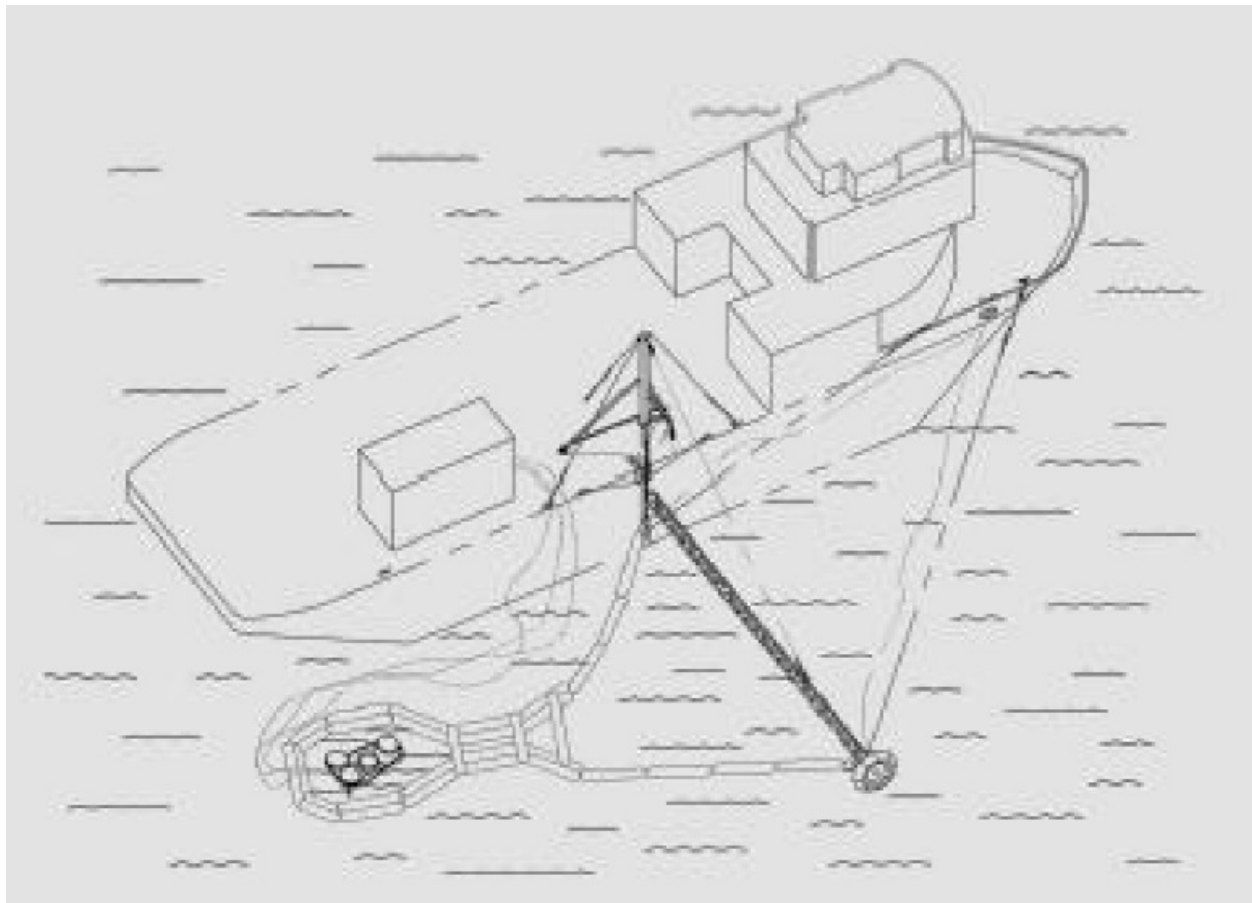

Fig. 82-Vessel of Opportunity Skimming System (VOSS) Basic Layout. Special oil spill outfitting shown on starboard side, 65' outrigger pictured with containment booms and generic standalone skimmers are depicted in the boom's pocket [67].

The VOSS outfitting includes a 65' outrigger, which is one length of inflatable containment boom with a built in skimming pocket, an inflatable support for the outrigger, various free-floating skimmers (depending on which system is shipped), and enough line to secure the outrigger to the ship. As seen in the drawing (Fig. 82), the outrigger is secured to one side of the vessel. It is supported by a tower and fastenings to the bow. This allows the VOSS to use only one vessel rather than the three required to use the MARCO skimmer.

As the ship moves forward at around 1 or 2 knots, oil is collected on the surface and channeled back towards the pocket housing the skimmers. In the diagram the skimmers are shown using generic circles though virtually any free-floating skimmer can be deployed there. Though the mechanics of oil skimming vary depending on which type of skimmer is used, all of them feature a tube that pumps skimmed oil and some free water into a holding tank in the vessel. Sometimes this holding tank has an overflow bladder towed behind the boat.

Although virtually any free-floating skimmer can be deployed with this system, representative skimmers from three of the most common form factors of skimmers have been selected to be profiled.

Lamor MiniMax 12 Brush Pump Skimmer (SK0055)

Fig. 83-Lamor MiniMax 12 Brush Pump Skimmer. Photographed in Warehouse [65].

Brush Pump Skimmers are widely used to pick up oils of medium viscosity. Two rows of oleophilic bristles turn through the surface and pick up the oil, the bristles are then scraped off as oil is pumped to a storage tank. Brush pump skimmers typically perform at recovery rates around 8 gal/min.

Lamor LWS-50 Weir Skimmer (SK0056)

Fig. 84-Lamor LWS-50 Wier Skimmer. Photographed just before use. [65]

Weir skimmers can collect any oil lighter than water. They work by collecting only the top layer, the first one or two millimeters depending on the way the skimmer is calibrated. Since oil is less dense than water, it floats on top of the water. If the oil spill is well contained, then the top two millimeters of fluid inside the spill area will be mostly oil. Debris is handled by a rotating blade near the pump inlet. After whatever fluid is picked up passes through that blade, it is pumped into a storage tank. Weir skimmers are by far the fastest of the free-floating oil skimmers and typically recover oil at approximately 35 gal/min

Action Petroleum Spill Recovery Inc. Model-24 Drum Skimmer (SK0825)

Fig. 85-Action Petroleum Spill Recovery Inc. Model 24 Drum Skimmer. Photographed with power unit on storage cart [66].

Drum skimmers can be used in a wide variety of applications. They work with an oleophilic drum that rotates through the water's surface. The drum picks up oil and allows water to slide off, then a scraper separates the oil from the drum and funnels the skimmed oil into a pump that sends the oil to a storage tank. These skimmers can separate oil and water better than any design on the market currently. Drum skimmers typically pickup around 10 gal/min. This particular skimmer is rated to yield oil with less than 1% free water.

Preliminary Conclusions

Actual implementation of an NRL burner in an oil spill collection and disposal system needs to consider the actual collection rates of the system. The oil recovery rate on the MARCO Class V vessel is too high to implement a burning apparatus with current technology. However, the VOSS is a potential candidate for the implementation of burners. With the installation of burners on a towed float or on outriggers of these vessels, the need for external storage of oil could be eliminated.

Comparison with S.L. Ross Burner

A comparative burner has been built and tested by S.L. Ross Environmental Research, Ltd., as reported by Refs. [62,68,69]. The design and operation of the burner can best be understood from Refs. [62,68]. It is sufficient to relate that the burner is composed of a chimney-like structure, placed on a pool of oil. Air jets are placed at the base of the chimney that entrain and atomize the oil into a helical flow pattern. From the papers, we can infer that the oil is coarsely atomized, with the finer droplets evaporating and burning the duct flow, and the coarser droplets splattering against the inside wall of the chimney where they evaporate and burn. Very little information is given on the detailed combustion process nor on the droplets and exhaust emissions. They reported a maximum burn rate for a 40 cm pool of 0.151 m^3/hr (0.95 bbl/hr) and predict, without full testing, a burn rate of 3.16 m^3/hr (19.9 bbl/hr) for a 1.83 m pool.

In comparison, the engineering-scale FBA combustor, with a 25.7 mm nozzle, was tested at 5.2 L/min (1.9 bbl/hr) with a limited air supply at an ALR of 0.82 for Oriente crude oil. The projected full operation for the same burner is 11.8 L/min (4.4 bbl/hr). If we assume that we use a 2 in (51 mm) spray nozzle, then the flow rate is 4x that of the engineering scale nozzle, or 46.1 L/min (17.4 bbl/hr).

Table 14-Predicted performance for the full-scale burner, with a 2 in (51 mm) nozzle.

	$\dot{m}_{Air}$ (kg/s)	$\dot{V}_{Oil}$ (L/min)	$\dot{m}_{ANS}$ (kg/s)	ALR_{ANS}	$\dot{m}_{ORN}$ (kg/s)	ALR_{ORN}	$\dot{V}_{Oil}$ (bbl/hr)
Ignition	1.5E-1	15.4	2.2E-1	0.68	2.3E-1	0.66	5.8
78% Full	3.8E-1	15.4	2.2E-1	1.71	2.3E-1	1.64	5.8
78% Full	3.8E-1	30.8	4.5E-1	0.85	4.7E-1	0.82	11.6
Full	4.9E-1	46.1	6.7E-1	0.73	7.0E-1	0.70	17.4

CONCLUSIONS

We successfully designed, built, and tested sub-scale and engineering-scale burners to develop a single nozzle burner capable of burning neat, emulsified, and weathered crude oil for spill response remediation. We designed the sub-scale burner at 25% full scale and the engineering-scale burner at 50% full scale. We developed and adapted scaling rules from the concept demonstration phase of this investigation [1]. We anticipate that the full-scale burner will be capable of burning 366 bbl/day of combustible crude oil

mixtures. This capacity meets the projected skimming capacity of the SupSalv Vessel of Opportunity Skimming System (VOSS).

The successful development of these two burners has a number of significant implications for flow-blurring atomizer technology, practical crude oil spray combustion, and the combustor design that we developed in this effort. There was significant concern that the flow-blurring atomizer would not efficiently atomize crude oil as the dimensions were increased from the 3.18 mm-diameter used during the concept demonstration [1] to the 12.7 mm and 25.7 mm-diameter atomizers used during this investigation. We found that the increase in size did not inhibit the atomizer performance in any way. This conclusion is especially important as we develop the final burner concept with an atomizer diameter of 50 mm. For the intended capacity of 366 bbl/day to meet the skimming rates of the VOSS, one large burner is sufficient.

We also observed during the development and testing of the larger engineering-scale burner that practical crude oil spray combustion improves with increasing size. The larger plume produced a much greater radiant heat transfer than the smaller plume, as measured by the thermocouples in the flow and the higher temperatures of the components. Though this effect resulted in the thermal failure of the plasma torches, the higher temperature ensures that the spray will evaporate and burn rapidly; the radiant heat transfer to the surrounding combustor shroud increases, which transfers more heat to the entrained air that passes through the shroud dilution holes, and the resulting combustion more stable.

The combustor design, composed of axially-staged, annular recirculation zones and a single air-assisted, flow-blurring atomizer, successfully nebulized and burned crude oil at two different scales. From the sub-scale burner, we were able to determine the optimum ignition-zone dimensions and dilution hole pattern that produced stable combustion. We then applied the same scaling rules to the engineering-scale burner, which resulted in even hotter plume combustion temperatures. One of the design concerns of the geometry was that the shroud would not allow sufficient dilution air to entrain into the plume while still reflecting radiant heat back to the plume and heating the dilution air. First stage dilution air studies showed that an acceptable balance between allowing sufficient dilution air to enter, constraining the recirculation zone, and anchoring the spray plume combustion was possible.

We also explored a number of fundamental scientific aspects of crude oil combustion that provided insight into basic oil combustion behavior and assisted in the design and testing of the burners. More prominent among these insights is the development of methods to emulsify crude oil for both laboratory and practical burn testing. As we discussed earlier, there is a great deal of literature on the dispersion of crude oil, but little work has been devoted to reliably emulsifying crude oils for research purposes. We also developed a reliable method to weather the crude oil, in isolation of the photochemical and biological interactions that occur in nature, to provide laboratory test fuel.

By using a flat flame-stabilized, laboratory spray burner, we were also able to explore both non-ideal and ideal spray burning behavior to examine the associated spray combustion behavior. In the practical-scale burners, routinely ejecting unburned spray, at rates ~2 L/min or greater, into the open air is an environmental and health hazard. In the laboratory, the amount of unburned spray was ~ 5 mL/min and we used exhaust hoods to remove the unburned spray from the experiment. This allowed us to explore unstable, marginal, or inefficient spray combustion behavior and determine how spray flow rates, air-liquid ratio, oil type, emulsification, and weathering influenced the fundamental spray behavior.

We discovered that flame radiation has a significant influence on the upstream flame anchoring of both the neat and emulsified crude oil. With sufficient upstream heat transfer, either through convection from the piloting flat flame burner or radiation from the downstream plume, the spray plume will anchor low to the nozzle and produce stable, steady combustion. This is especially significant for crude oil, in comparison to conventional hydrocarbon fuels, which have a much greater range of molecular weights

among the constituents, especially at the higher weights. Furthermore, there is significantly more radiative absorption from the suspended asphaltenes in the crude oil.

One of the tangential discoveries that we made from our analytical measurements was the presence of a wide range of oxygenated hydrocarbons in the exhaust from the poorly burned emulsified crude oil. This discovery should be examined more closely to determine if it provides a potential method to develop a chemical or spectroscopic sensor for detecting lean blow off.

FUTURE WORK

The next phase of this research will continue to resolve some of the engineering issues of the burner system. First, the ignition source needs to be refined so that a steady, high temperature ignition source is available to ignite and anchor emulsified and weathered mixtures. We will continue work with emulsified and weathered mixtures, ensuring their stability and defining their chemical properties to assist in ignition studies. The thermal strain on the structure of the burner also needs to be addressed by refining the burner design. In order to design a burner structure that can be assembled, repeatedly thermally cycled, disassembled, stored, and shipped, a more robust design needs to be developed and tested. The broken welds and warped bulkheads and flanges indicate that the structural design needs to be adapted to the thermal strain associated with enclosing the burning plume.

Once these engineering issues are addressed, a complete burner system, including the burner structure, ignition system, fuel pump, air compressor, and power generation system needs to be design and tested. But, these final development steps need to be carried out in collaboration with NAVSEA SupSalv, who would be one of the final users of the system.

The laboratory methods and instrumentation we have developed will continue to allow us to support further research in this area. The two-dimensional laser and phase Doppler anemometry (LDA/PDA) and the CARS instrumentation will allow us to support continued measurements of gas and multi-phase combusting flow. We have also developed key analytical techniques for the analysis of soot and combustion products generated from the burner system. These technique will be incredibly insightful into the chemistry of the flame and possibly provide us with additional diagnostic measurements into the performance of the burner. These analytical protocols can be further developed to improve the characterization of the material going into and coming out of the burner. These techniques developed in this study gave us a solid foundation to explore the dynamics of the combustion products in future projects.

ACKNOWLEDGEMENTS

PERSONNEL

The Navy Technology Center for Safety and Survivability of the Naval Research Laboratory has an established history of successfully supporting the combustion and fire testing of the Navy's facilities and operations.

Dr. Steven Tuttle is a Mechanical Engineer and Section Head in the Combustion Dynamics and Modeling Section of the Navy Technology Center for Safety and Survivability (NTCSS) at the U.S. Naval Research Laboratory (NRL). Dr. Tuttle worked in the gas turbine industry for seven years while managing and conducting his doctoral research at the University of Connecticut. As an engineer, he developed and validated heat transfer, thermoacoustic, and spray combustion stability models for main burners,

afterburners, and nozzles in the engine technology development and demonstration organizations. At the same time, he directed and managed funding to the University of Connecticut that supported his research and that of others. As a student, he designed and built an afterburner combustion experiment and the associated electronic fuel control and safety systems. Dr. Tuttle mentored undergraduates and led the team of MS and PhD students as they conducted experiments and measured the fuel distribution, flowfield, and combustion behavior. For his postdoctoral studies, he was the principle investigator for velocity measurements of a reacting scramjet cavity and shear layer at the U.S. Air Force Research Laboratory. He joined the staff at NRL in 2011, where he is the principle investigator on a Department of Interior-sponsored program examining the spray combustion behavior of emulsified crude oil and a contributor on the design of a small gas turbine in Code 5712. He also collaborates with other NRL investigators in projects ranging from fuel sensing to fire characterization and instrumentation.

Dr. Alfredo Tuesta is a mechanical engineer conducting post-doctoral research in the Combustion Dynamics and Modeling Section of NTCSS at the U.S. Naval Research Laboratory in Washington D. C. His current work focuses on laser diagnostics of plumes from a crude oil, spray burner and a resisto-jet engine. He completed a MS in Mechanical Engineering at the Birck Nanotechnology Center in Purdue University. His thesis explored the plasma environment responsible for the synthesis of carbon nanostructures via absorption spectroscopy of acetylene. Dr. Tuesta expanded on this work by measuring the temperature and concentration of molecular hydrogen in the plasma via coherent anti-Stokes Raman scattering spectroscopy and by utilizing a Langmuir probe to determine the plasma's electron energy density function. He completed a PhD in mechanical engineering in 2014 based on his findings.

Ms. Katherine M. Hinnant is a Chemical Engineer in the Combustion Dynamics and Modeling Section of the Navy Technology Center for Safety and Survivability (NTCSS) at the U.S. Naval Research Laboratory (NRL). Ms. Hinnant graduated with her bachelors in chemical engineering from the University of Virginia in 2014. As an intern through the Naval Research Enterprise Internship Program, she was involved in the design of a novel experiment to measure the mass transport of fuels through firefighting foams. Her work as an intern led to a contract position at NRL through NOVA Research, Inc. until 2016 when she hired as a federal employee. Her work at the lab has focused on experiment design and physical property assessment through work with firefighting foam and her role as the wet chemist for MilSpec foam testing. She is pursuing her doctorate in Physical Chemistry through the Edison Memorial Graduate Training Program at George Washington University, in which she is examining foam degradation during flame extinction using optical diagnostics. Ms. Hinnant contributes to a range of programs, including firefighting foam development, low-concentration sulfur dioxide detection, novel gas fires suppression agent validation, and small gas turbine combustor development. For this work, Ms. Hinnant assists in large-scale data collection, physical property assessments of crude oil samples, and designed the weathering of crude oil experiment.

Dr. Brian T. Fisher is a Mechanical Engineer in the Combustion Dynamics and Modeling Section of the Navy Technology Center for Safety and Survivability (NTCSS) at the U.S. Naval Research Laboratory (NRL). Dr. Fisher has a background in combustion diagnostics, diesel engine combustion, and multi-phase fire suppression. He has experience with chemical kinetics, combustion, flame stability, and fuel sprays. His research has included fire suppression and optical diagnostics of basic diesel/gas turbine combustion behavior. He was a postdoc both at NRL and at Sandia National Laboratory's Combustion Research Facility. He arrived in 2015 after working as a professor and research supervisor at the University of Alabama for over three years.

Dr. Michael Weismiller worked as a postdoctoral researcher at the Naval Research Laboratory before going to the Department of Energy. While here, he conducted fundamental and applied research to examine the combustion behavior of metal fuel additives in the laboratory spray burner and other platforms. In the

process, he also made fundamental droplet measurements of various benchmark fluids with the flow-blurring atomizer to characterize the behavior.

Dr. Thomas N. Loegel is a research chemist within the Chemical Sensing and Fuel Technology Section of the Chemistry Division at the Naval Research Laboratory. He is a recipient of the Jerome and Isabella Karle Fellowship and tasked to develop response factors among different gas chromatography and mass spectroscopy detectors to enhance modeling of fuel properties and to develop new multidimensional separation strategies for the analysis of complex mixtures. His areas of research include characterization of petroleum and alternative fuels using a combination of gas chromatography and mass spectrometry. He has extensive experience with a wide variety of chromatography techniques and has worked with a variety of sample types ranging from heavy crude products to pharmaceuticals. Using gas chromatography–mass spectrometry (GC-MS), liquid chromatography–mass spectrometry (LC-MS), and the powerful two dimensional GC time-of-flight (GCxGC TOF), Dr. Loegel has been able to improve and develop methods that probe the complex constituents of petroleum fuels. Dr. Loegel's Ph.D. dissertation research focused on separations of glycoaminoglycans (heparin) by capillary electrophoresis (CE) and asphaltenes, a heavy fraction of crude oil, by high performance liquid chromatography (HPLC). While at Miami University, he initiated an asphaltene-based, Ph.D.-level research project and forged collaboration with the H. Kenttämaa group at Purdue University using high resolution MS.

REFERENCES

[1]   Tuttle, S. G., Farley, J. P., and Fleming, J. W., "Efficient Atomization and Combustion of Emulsified Crude Oil," Naval Research Laboratory, NRL/MR/6185-14-9566. Washington, DC, September 2014.

[2]   Smith, G. F. and McCracken, W. E., "Ohmsett High Seas Performance Testing: MARCO Class V Oil Skimmer," *English,* U.S. Environmental Protection Agency, EPA-600/2-78-093. Cincinnati, Ohio, May 1978.

[3]   Buist, I. A., McCourt, J., Potter, S., Ross, S., and Trudel, K., "In Situ Burning," *Pure and Applied Chemistry* Vol. 71, No. 1, 1999, pp. 43–65.
       doi: 10.1351/pac199971010043

[4]   Schaum, J., Cohen, M., Perry, S., Artz, R., Draxler, R., Frithsen, J. B., Heist, D., Lorber, M., and Phillips, L., "Screening Level Assessment of Risks Due to Dioxin Emissions from Burning Oil from the BP Deepwater Horizon Gulf of Mexico Spill," *Environmental Science & Technology* Vol. 44, No. 24, 2010, pp. 9383–9389.
       doi: 10.1021/es103559w

[5]   Kearney, S. P. and Pierce, F., "Evidence of soot superaggregates in a turbulent pool fire," *Combustion and Flame* Vol. 159, No. 10, 2012, pp. 3191–3198.
       doi: 10.1016/j.combustflame.2012.04.011

[6]   Markatos, N. C., Christolis, C., and Argyropoulos, C., "Mathematical modeling of toxic pollutants dispersion from large tank fires and assessment of acute effects for fire fighters," *International Journal of Heat and Mass Transfer* Vol. 52, No. 17–18, 2009, pp. 4021–4030.
       doi: 10.1016/j.ijheatmasstransfer.2009.03.039

[7]   Argyropoulos, C. D., Sideris, G. M., Christolis, M. N., Nivolianitou, Z., and Markatos, N. C., "Modelling pollutants dispersion and plume rise from large hydrocarbon tank fires in neutrally stratified atmosphere," *Atmospheric Environment* Vol. 44, No. 6, 2010, pp. 803–813.
       doi: 10.1016/j.atmosenv.2009.11.034

[8]   Michel, J., Scholz, D., Warren, S. R., and Walker, A. H., "*In-Situ* Burning: A Decision-Maker's Guide to In-Situ Burning," American Petroleum Institute, 4740. 2005.

[9]   Buist, I. A., "Disposal of Spilled Hibernia Crude Oils and Emulsions: In-Situ Burning and the "Swirlfire" Burner," *12th Arctic and Marine Oil Spill Program Technical Seminar*, Environment Canada, 1989.

[10]   Tebeau, P., Murphy, M., Vicedomine, J., and Sprague, M., "Technology Assessment and Concept Evaluation for Alternative Approaches to In-Situ Burning of Oil Spills in the Marine Environment," U.S. Minerals Management Service, Herndon, Virginia, Contract No. 1435-01-97-PO14176. Marine Research Associates, LLC 158 Wyassup Road North Stonington, CT 06359, 1998.

[11]   Bedford, F., Rutland, C., Dittrich, P., and Raab, A., "Effects of Direct Water Injection on DI Diesel Engine Combustion," SAE 2001-01-2938.

[12]   Barnaud, F., Schmelzle, P., and Schulz, P., "AQUAZOLE™: An Original Emulsified Water-Diesel Fuel for Heavy-Duty Applications " SAE 2000-01-1861.

[13]   Hines, W. R., "Gas turbine engine with water injection." Google Patents, 2000.

[14]   Nishida, K., Takagi, T., and Kinoshita, S., "Regenerative steam-injection gas-turbine systems," *Applied Energy* Vol. 81, No. 3, 2005, pp. 231-246.
        doi: 10.1016/j.apenergy.2004.08.002

[15]   Bartle, K. D., Jones, J. M., Lea-Langton, A. R., Pourkashanian, M., Ross, A. B., Thillaimuthu, J. S., Waller, P. R., and Williams, A., "The combustion of droplets of high-asphaltene heavy oils," *Fuel* Vol. 103, No. 0, 2013, pp. 835-842.
        doi: 10.1016/j.fuel.2012.07.004

[16]   Ombrello, T., Won, S. H., Ju, Y., and Williams, S., "Flame propagation enhancement by plasma excitation of oxygen. Part I: Effects of O3," *Combustion and Flame* Vol. 157, No. 10, 2010, pp. 1906-1915.
        doi: 10.1016/j.combustflame.2010.02.005

[17]   Ombrello, T., Won, S. H., Ju, Y., and Williams, S., "Flame propagation enhancement by plasma excitation of oxygen. Part II: Effects of O2(a1Δg)," *Combustion and Flame* Vol. 157, No. 10, 2010, pp. 1916-1928.
        doi: 10.1016/j.combustflame.2010.02.004

[18]   Incropera, F. P. and DeWitt, D. P., *Fundamentals of heat and mass transfer*, Wiley, 1996.

[19]   Blevins, L. G. and Pitts, W. M., "Modeling of bare and aspirated thermocouples in compartment fires," *Fire Safety Journal* Vol. 33, No. 4, 1999, pp. 239-259.
        doi: 10.1016/S0379-7112(99)00034-X

[20]   LeFebvre, A. H., *Atomization and Sprays*, 1 ed., Hemisphere Publishing Corporation, 1989.

[21]   Turns, S. R., *An Introduction to Combustion: Concepts and Applications*, 2 ed., McGraw-Hill, Boston, USA, 2000, pp. 522.

[22]   Kee, R. J., Rupley, F. M., Miller, J. A., Coltrin, M. E., Grcar, J. F., Meeks, E., Moffat, H. K., Lutz, A. E., Dixon-Lewis, G., Smooke, M. D., Warnatz, J., Evans, G. H., Larson, R. S., Mitchell, R. E., Petzold, L. R., Reynolds, W. C., Caracotsios, M., Stewart, W. E., Glarborg, P., Wang, C., and Adigun, O., "Chemkin Collection." 3.6 ed., Reaction Design, Inc., 2000.

[23]   O'Loughlin, W. and Masri, A. R., "A new burner for studying auto-ignition in turbulent dilute sprays," *Combustion and Flame* Vol. 158, No. 8, 2011, pp. 1577-1590.
        doi: 10.1016/j.combustflame.2010.12.021

[24]   Morley, C., "Gaseq, A Chemical Equilibrium Program for Windows." 2005.

http://www.gaseq.co.uk/

[25]   Tuesta, A. D., Bhuiyan, A., Lucht, R. P., and Fisher, T. S., "Laser Diagnostics of Plasma in Synthesis of Graphene-Based Materials," *Journal of Micro and Nano-Manufacturing* Vol. 2, No. 3, 2014, pp. 031002-031002.
       doi: 10.1115/1.4027547

[26]   Thariyan, M. P., Bhuiyan, A. H., Meyer, S. E., Naik, S. V., Gore, J. P., and Lucht, R. P., "Dual-pump coherent anti-Stokes Raman scattering system for temperature and species measurements in an optically accessible high-pressure gas turbine combustor facility," *Measurement Science and Technology* Vol. 22, No. 1, 2011, p. 015301.
       doi: 10.1088/0957-0233/22/1/015301

[27]   Kearney, S. P. and Jackson, M. N., "Dual-Pump Coherent Anti-Stokes Raman Scattering Thermometry in Heavily Sooting Flames," *AIAA Journal* Vol. 45, No. 12, 2007, pp. 2947-2956.
       doi: 10.2514/1.31054

[28]   Lucht, R. P., "Three-laser coherent anti-Stokes Raman scattering measurements of two species," *Optics Letters* Vol. 12, No. 2, 1987, pp. 78-80.
       doi: 10.1364/OL.12.000078

[29]   Law, C. K., *Combustion Physics*, Cambridge University Press, 2006.

[30]   Ocampo-Barrera, R., Villasenor, R., and Diego-Marin, A., "An experimental study of the effect of water content on combustion of heavy fuel oil/water emulsion droplets," *Combustion and Flame* Vol. 126, No. 4, 2001, pp. 1845-1855.
       doi: 10.1016/s0010-2180(01)00295-4

[31]   Nielsen, H. P., Frandsen, F. J., Dam-Johansen, K., and Baxter, L. L., "The implications of chlorine-associated corrosion on the operation of biomass-fired boilers," *Progress in Energy and Combustion Science* Vol. 26, No. 3, 2000, pp. 283-298.
       doi: http://dx.doi.org/10.1016/S0360-1285(00)00003-4

[32]   Tuttle, S. G., Lokare, S., Dunaway, M. D., Anderson, J. D., Moulton, D., Tree, D. R., Baxter, L. L., Mehta, A., Bakker, W., and Facciano, T., "Stoichiometric Effects on Boiler Corrosion from High-Chlorine and High-Alkaline Coals," *Western States Combustion Institute Conference*, Combustion Institute, 2002.

[33]   Baxter, L. L., Tree, D. R., Lokare, S., Dunaway, M. D., Moulton, D., Mehta, A., Bakker, W., and Facciano, T., "Mechanistic Investigation of Chlorine-based, High-temperature Boiler Corrosion," *UEF Conference, Power Production in the 21st Century: Impacts of Fuel Quality and Operations*, United Engineering Foundation, 2001.

[34]   Notarianni, K. A., Evans, D. D., and Walton, W. D., "Smoke Production From Large Oil Pool Fires," *6th International Fire Conference*, Society of Fire Protection Engineers, 1993.

[35]   Evans, D. D., Walton, W. D., Baum, H. R., Mulholland, G. W., Lawson, J. R., Koseki, H., and Ghoniem, A. F., "Smoke Emission From Burning Crude Oil," National Institute of Standards and Testing, NIST SP 995. Vol. 2, 12-14 June 1991.

[36]   Evans, D. D., Walton, W. D., Baum, H. R., Notarianni, K. A., Tennyson, E. J., and Tebeau, P. A., "Mesoscale Experiments Help to Evaluate In-Situ Burning of Oil Spills," *Oil Spill Conference*, American Petroleum Institute, Washington, DC, 1993.

[37]   Gañán-Calvo, A. M., "Enhanced liquid atomization: From flow-focusing to flow-blurring," *Applied Physics Letters* Vol. 86, No. 21, 2005, p. 214101.
       doi: 10.1063/1.1931057

[38]   Jiang, L. and Agrawal, A., "Investigation of Glycerol Atomization in the Near-Field of a Flow-Blurring Injector using Time-Resolved PIV and High-Speed Visualization," *Flow, Turbulence and Combustion* Vol. 94, No. 2, 2015, pp. 323-338.
       doi: 10.1007/s10494-014-9572-2

[39]   Simmons, B. M. and Agrawal, A. K., "Spray Characteristics of a Flow-Blurring Atomizer," *Atomization and Sprays* Vol. 20, No. 9, 2010, pp. 821-835.
       doi: 10.1615/AtomizSpr.v20.i9.60

[40]   LeFebvre, A. H., *Gas Turbine Combustion*, 2 ed., Taylor & Francis, Philadelphia, 1999.

[41]   ASTM D1141-98, "Standard Practice for the Preparation of Substitute Ocean Water", ASTM International, West Conshohocken, PA, 2013.

[42]   Belore, R. C., Trudel, K., Mullin, J. V., and Guarino, A., "Large-scale cold water dispersant effectiveness experiments with Alaskan crude oils and Corexit 9500 and 9527 dispersants," *Marine Pollution Bulletin* Vol. 58, No. 1, 2009, pp. 118-128.
       doi: 10.1016/j.marpolbul.2008.08.013

[43]   Fingas, M. F., "A Review of Literature Related to Oil Spill Dispersants: 1997-2008," Prince William Sound Regional Citizens' Advisory Council. Anchorage, AL.

[44]   *Oil Spill Dispersants: Efficacy and Effects*, The National Academies Press, 2005.

[45]   Zheng, R., Bray, K. N. C., and Rogg, B., "Effect of Sprays of Water and NaCl-Water Solution on the Extinction of Laminar Premixed Methane-Air Counterflow Flames," *Combustion Science and Technology* Vol. 126, No. 1-6, 1997, pp. 389-401.
       doi: http://dx.doi.org/10.1080/00102209708935683

[46]   Lazzarini, A. K., Krauss, R. H., Chelliah, H. K., and Linteris, G. T., "Extinction conditions of non-premixed flames with fine droplets of water and water/NaOH solutions," *Proceedings of the Combustion Institute* Vol. 28, No. 2, 2000, pp. 2939-2945.
       doi: http://dx.doi.org/10.1016/S0082-0784(00)80719-5

[47]   Mesli, B. and Gökalp, I., "Extinction Limits of Opposed Jet Turbulent Premixed Methane Air Flames with Sprays of Water and NaCl-Water Solution," *Combustion Science and Technology* Vol. 153, No. 1, 2000, pp. 193-211.
       doi: 10.1080/00102200008947260

[48]   Chelliah, H. K., Lazzarini, A. K., Wanigarathne, P. C., and Linteris, G. T., "Inhibition of premixed and non-premixed flames with fine droplets of water and solutions," *Proceedings of the Combustion Institute* Vol. 29, No. 1, 2002, pp. 369-376.
       doi: http://dx.doi.org/10.1016/S1540-7489(02)80049-9

[49]   Korobeinichev, O. P., Shmakov, A. G., Chernov, A. A., Bol'shova, T. A., Shvartsberg, V. M., Kutsenogii, K. P., and Makarov, V. I., "Fire suppression by aerosols of aqueous solutions of salts," *Combustion, Explosion, and Shock Waves* Vol. 46, No. 1, 2010, pp. 16-20.
       doi: http://dx.doi.org/10.1007/s10573-010-0003-y

[50]   Joseph, P., Nichols, E., and Novozhilov, V., "A comparative study of the effects of chemical additives on the suppression efficiency of water mist," *Fire Safety Journal* Vol. 58, 2013, pp. 221-225.
       doi: http://dx.doi.org/10.1016/j.firesaf.2013.03.003

[51]   Williams, B. A. and Fleming, J. W., "Suppression mechanisms of alkali metal compounds," *Proceeding of the Halon Options Technical Working Conference*, 1999.

[52] Jensen, D. E. and Jones, G. A., "Kinetics of flame inhibition by sodium," *Journal of the Chemical Society, Faraday Transactions 1: Physical Chemistry in Condensed Phases* Vol. 78, No. 9, 1982, pp. 2843-2850.
doi: 10.1039/F19827802843

[53] Hynes, A. J., Steinberg, M., and Schofield, K., "The chemical kinetics and thermodynamics of sodium species in oxygen-rich hydrogen flames," *The Journal of Chemical Physics* Vol. 80, No. 6, 1984, pp. 2585-2597.
doi: doi:http://dx.doi.org/10.1063/1.447052

[54] Slack, M., Cox, J. W., Grillo, A., Ryan, R., and Smith, O., "Potassium kinetics in heavily seeded atmospheric pressure laminar methane flames," *Combustion and Flame* Vol. 77, No. 3, 1989, pp. 311-320.
doi: http://dx.doi.org/10.1016/0010-2180(89)90137-5

[55] Zamansky, V. M., Lissianski, V. V., Maly, P. M., Ho, L., Rusli, D., and Gardiner Jr, W. C., "Reactions of sodium species in the promoted SNCR process," *Combustion and Flame* Vol. 117, No. 4, 1999, pp. 821-831.
doi: http://dx.doi.org/10.1016/S0010-2180(98)00127-8

[56] Husain, D., Plane, J. M. C., and Xiang, C. C., "Absolute third-order rate constant for the reaction between Rb + OH + He determined by time-resolved molecular resonance-fluorescence spectroscopy, OH (A2[capital Sigma]+-X2[capital Pi]), coupled with steady atomic resonance-fluorescence measurements, Rb(6 2P-5 2S1/2)," *Journal of the Chemical Society, Faraday Transactions 2: Molecular and Chemical Physics* Vol. 81, No. 4, 1985, pp. 561-573.
doi: 10.1039/F29858100561

[57] Patrick, R. and Golden, D. M., "Termolecular reactions of alkali metal atoms with O2 and OH," *International Journal of Chemical Kinetics* Vol. 16, No. 12, 1984, pp. 1567-1574.
doi: 10.1002/kin.550161210

[58] Fisher, B. T., Weismiller, M. R., Tuttle, S. G., and Hinnant, K. M., "Effects of fluid properties on flow-blurring atomizer sprays, Submitted," *ASME Turbo Expo 2017: Turbomachinery Technical Conference and Exposition*, ASME, 2017.

[59] Junk, G. A. and Richard, J. J., "Dioxins not detected in effluents from coal/refuse combustion," *Chemosphere* Vol. 10, No. 11, 1981, pp. 1237-1241.
doi: 10.1016/0045-6535(81)90040-0

[60] Wielgosiński, G., "The Reduction of Dioxin Emissions from the Processes of Heat and Power Generation," *Journal of the Air & Waste Management Association* Vol. 61, No. 5, 2011, pp. 511-526.
doi: 10.3155/1047-3289.61.5.511

[61] Ahling, B., Bjørseth, A., and Lunde, G., "Formation of chlorinated hydrocarbons during combustion of poly (vinyl chloride)," *Chemosphere* Vol. 7, No. 10, 1978, pp. 799-806.
doi: 10.1016/0045-6535(78)90063-2

[62] Cooper, D. W., Buist, I. A., Belore, R. C., Nedwed, T. J., and Tidwell, A. C., "One-step Offshore Collection and Removal: Combining an Oleopohilic Skimmer and Floating Burner," *35th Arctic and Marine Oil Spill Program (AMOP) Technical Seminar*, Environmental Canada, 2012.

[63] ASTM F2709-08, "Standard Test Method for Determining Nameplate Recovery Rate of Stationary Oil Skimmer Systems", ASTM International, West Conshohocken, PA, 2008.

[64]   "U.S. Navy Emergency Ship Salvage Material Catalog, Pollution Equipment," U.S. Navy, SEA 00C, Supervisor of Salvage, 0910-LP-722-6800, E ed. Vol. 2, 30 June 2006.

[65]   "VOSS, High Speed Current Buster," U.S. Navy, SEA 00C, S0300-BC-CAT-020 P16300. 4 February 2014.

[66]   "Inland Support Skimmer System," U.S. Navy, SEA 00C, S0300-BC-CAT-020 P16700. 4 February 2014.

[67]   "Vessel of Opportunity Skimmer System, Class XI," U.S. Navy, SEA 00C, S0300-BC-CAT-020 P16310. 4 February 2014.

[68]   Zhang, C., Nedwed, T., Tidwell, A., Urbanski, N., Cooper, D., Buist, I., and Belore, R., "One-Step Offshore Oil Skim and Burn System for use with Vessels of Opportunity," *International Oil Spill Conference Proceedings*, American Petroleum Institute, 2014.

[69]   Nedwed, T. J., Tidwell, A. C., Buist, I. A., Belore, R. C., and Cooper, D. W., *Method and system for oil release management*, USA Patent No. US 20150284925 A1, Oct 8, 2015.

Appendix A

EQUIVALENCE RATIO CALCULATION

$$\phi = \frac{(F/A)}{(F/A)_{stoic}} \tag{A.1}$$

The stoichiometric fuel air ratio is calculated from the following expressions for a given hydrocarbon fuel:

$$C_xH_y + \alpha(3.76N_2 + O_2) \rightarrow xCO_2 + \frac{y}{2}H_2O + 3.76\alpha N_2 \tag{A.2}$$
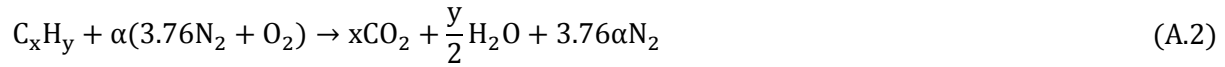
$$\alpha = (1 - \beta)x \tag{A.3}$$

$$(F/A)_{stoic} = \frac{MW_{fuel}}{4.76\alpha MW_{air}} \tag{A.4}$$

$$MW_{mix} = \sum_i \chi_i MW_i \tag{A.5}$$

where α is the number of moles of air, x is the number of moles of carbon in the fuel, and y is the number of mols of hydrogen in the fuel. The number of moles of air is solved by solving the expression of oxygen on either side of the chemical equation for α, using equation (A.3). The stoichiometric fuel-air ratio is the ideal fuel-air mixture that leaves no remaining molecules of fuel or oxygen in the exhaust, assuming idealized, complete combustion. In order to calculate the mass flow of the air and fuel mixture for a given equivalence ratio, we must first calculate the stoichiometric fuel-air ratio, using equation (A.4).

Appendix B

CRUDE OIL ASSAY

The following list contains the assay data for the Ecuadorian (Oriente) and Alaskan North Slope (ANS) crude oil that we will be examining in this study. A cursory examination reveals that the ANS contains a lighter cut of hydrocarbons and is much less viscous when compared to the Oriente. The ANS assay is from 1999, which is rather old, but the contact at Chevron related that ANS has shown remarkable consistency over the years. We may consider independent assay of both crude oils for verification.

COUNTRY	Ecuador	USA
STATE		Alaska
CRUDE	Oriente Heavy Exp Bld (CVX) '10	Alaska N. Slope (BP)
REFERENCE	ORINT234-L	ANS297BP
SAMPLE DATE	2010	1999
ANALYSIS QUALITY	A	BP
WHOLE CRUDE INSPECTIONS		
Gravity, °API	23.4	29.7
Specific Gravity	0.9135	0.8797
Sulfur, wt %	1.48	1.08
Mercaptan Sulfur, ppm	2	4
Dissolved H2S, ppm	0.000268	
Nitrogen, ppm	2980	2000
Pour Point °F	-21.2	-11
Pour Point °C	-29.6	-23.9
Acid Number, mg KOH/g	0.1	0.07
Back-Blended Acid, mg KOH/g	0.0402	
Viscosity @ 40 °C (104 °F), cSt	48.1	9.53
Viscosity @ 50 °C (122 °F), cSt	31.3	7.31
Asphaltenes, C7, %	8.91	
Nickel, ppm	70.8	
Vanadium, ppm	175	
Characterization Factor, K	11.77	
MCR, wt%	9.86	
TBP YIELDS, VOL %		
Butanes and Lighter	0.918	3.1
Light Gasoline (55-175 °F)	2.832	6.0
Light Naphtha (175-300 °F)	8.297	12.2
Heavy Naphtha (300-400 °F)	7.267	5.0
Kerosene (400-500 °F)	8.244	8.4
Atm. Gas Oil (500-650 °F)	14.304	13.3
Lt Vacuum Gas Oil (650-800 °F)	13.627	13.3
Hvy Vacuum Gas Oil (800-1050 °F)	19.186	17.8

Vacuum Residuum (1050 °F+)	25.326	17.9
LIGHT GASOLINE (55-175 °F)		
Gravity, °API	81.5	82.5
Specific Gravity	0.6643	0.6626
Mercaptan Sulfur, ppm	0.289	4
Octane Number, Research, Clear	74.4	67
LIGHT NAPHTHA (175-300 °F)		
Gravity, °API	56.4	53.1
Specific Gravity	0.7531	0.7681
Mercaptan Sulfur, ppm	1.13	4
Naphthenes, vol %	44.15	43
Aromatics, vol %	8.28	16
Octane Number, Research, Clear	61.5	60
HEAVY NAPHTHA (300-400 °F)		
Gravity, °API	46.3	44.8
Specific Gravity	0.7959	0.8043
Sulfur, wt %	0.0378	0.03
Mercaptan Sulfur, ppm	1.42	2
Naphthenes, vol %	49.46	42
Aromatics, vol %	11.58	23
Smoke Point, mm (ASTM)	24.7	23
KEROSENE (400-500 °F)		
Gravity, °API	38.3	36.6
Specific Gravity	0.8335	0.8435
Sulfur, wt %	0.321	0.14
Mercaptan Sulfur, ppm	2.26	2
Naphthenes, vol %	50.72	45
Aromatics, vol %	16.82	26
Freezing Point, °F	-49.7	
Freezing Point, °C	-45.4	
Smoke Point, mm (ASTM)	19.2	18
Acid Number, mg KOH/g	0.0188	0.04
Viscosity @ 50 °C (122 °F), cSt	1.54	1.58
ATM. GAS OIL (500-650 °F)		
Gravity, °API	32	30
Specific Gravity	0.8655	0.8780
Sulfur, wt %	0.915	0.66
Nitrogen, ppm	97	81
Acid Number, mg KOH/g	0.0304	0.06
Pour Point °F	4.8	0
Pour Point °C	-15.1	-17.8
Viscosity @ 50 °C (122 °F), cSt	3.59	3.59
Cetane Index	51.2	44
Characterization Factor, K	11.7	11.5

ATM. RESIDUUM (650 °F+)

Yield, vol%	58.139	49.0
Gravity, °API	11.8	14.6
Specific Gravity	0.9874	0.9706
Sulfur, wt %	2.1	1.78
Nitrogen, ppm	4700	3350
MCR, wt%	15.6	9.6
Asphaltenes, C7, %	14.1	3.8
Nickel, ppm	112	22
Vanadium, ppm	278	51
Pour Point °F	83.4	
Pour Point °C	28.6	
Viscosity @ 50 °C (122 °F), cSt	4140	734
Viscosity @ 100 °C (212 °F), cSt	215	47.5
Characterization Factor, K	11.64	11.7

LT VAC. GAS OIL (650-800 °F)

Gravity, °API	24.2	23.8
Specific Gravity	0.9087	0.9131
Sulfur, wt %	1.4	1.22
Nitrogen, ppm	822	750
Naphthenes, vol %	46.48	48
Paraffins, vol%	19.32	17
Pour Point °F	56.9	65
Pour Point °C	13.8	18.3
Acid Number, mg KOH/g	0.0469	0.10
Aniline Point, °F	166.9	161
Aniline Point, °C	75	71.7
Hydrogen, wt%	12.61	12.3
Viscosity @ 50 °C (122 °F), cSt	14.5	15.0
Viscosity @ 100 °C (212 °F), cSt	3.84	3.92
Characterization Factor, K	11.65	

HVY VAC. GAS OIL (800-1050 °F)

Gravity, °API	19.1	23.8
Specific Gravity	0.9399	0.9131
Sulfur, wt %	1.67	1.43
Nitrogen, ppm	2220	2070
Acid, mg KOH/g		0.12
MCR, wt%	1.26	
Nickel, ppm	1.62	
Vanadium, ppm	4.33	
Pour Point °F	106.1	108
Pour Point °C	41.1	42.2
Acid Number, mg KOH/g	0.064	
Aniline Point, °F	185.1	179
Aniline Point, °C	85.1	81.7

Hydrogen, wt%	12.09	11.5
Viscosity @ 50 °C (122 °F), cSt	174	734
Viscosity @ 100 °C (212 °F), cSt	18.6	47.5
Characterization Factor, K	11.84	11.7
VACUUM RESIDUUM (1050 °F+)		
Yield, vol%	25.326	17.9
Gravity, °API	1.3	5.1
Specific Gravity	1.0658	1.0381
Sulfur, wt %	2.71	2.47
Nitrogen, ppm	8140	6200
Hydrogen, wt%	10.02	9.5
MCR, wt%	32.4	24.6
Asphaltenes, C7, %	30	9.7
Nickel, ppm	238	57
Vanadium, ppm	588	130
Pour Point °F	277	180
Pour Point °C	136.1	82.2
Viscosity @ 50 °C (122 °F), cSt	4.84E+10	6.51E+07
Viscosity @ 100 °C (212 °F), cSt	5.30E+06	1.26E+04
Viscosity @ 135 °C (275 °F), cSt	1.09E+05	9.30E+02
Cutter, vol% in Fuel Oil	46.9	42
Fuel Oil Yield, vol%	47.7	30.8
Characterization Factor, K	11.6	11.8